KU LEUVEN

ARENBERG DOCTORAL SCHOOL
Faculty of Engineering Science

Data-driven local and global reconstruction of white matter fibres in diffusion-weighted imaging

Daan Christiaens

Supervisors:
Prof. dr. ir. F. Maes
Prof. dr. S. Sunaert

Dissertation presented in partial
fulfilment of the requirements for the
degree of Doctor of Engineering Science (PhD):
Electrical Engineering

July 2016

Data-driven local and global reconstruction of white matter fibres in diffusion-weighted imaging

Daan CHRISTIAENS

Examination committee:
Prof. dr. ir. P. Van Houtte, chair
Prof. dr. ir. F. Maes, supervisor
Prof. dr. S. Sunaert, supervisor
Prof. dr. P. Dupont
Prof. dr. ir. P. Suetens
Prof. dr. ir. S. Van Huffel
Dr. L. Emsell
Prof. dr. J.-D. Tournier
(King's College London)
Dr. Dipl. Inf. M. Reisert
(University of Freiburg Medical Center)

Dissertation presented in partial fulfilment of the requirements for the degree of Doctor of Engineering Science (PhD): Electrical Engineering

July 2016

Il semble que la perfection soit atteinte non quand il n'y a plus rien à ajouter, mais quand il n'y a plus rien à retrancher.

— Antoine de Saint-Exupéry, Terre des Hommes

Voorwoord

Een doctoraat maken is vaak eenzaam maar doe je nooit alleen. Bij aanvang van dit boek wil ik daarom enkele mensen bedanken die rechtstreeks of onrechtstreeks hebben bijgedragen tot dit werk.

In de eerste plaats wil ik mijn promotor, prof. Frederik Maes, bedanken voor zijn steun en vertrouwen. Frederik, je hebt me van bij het begin veel vrijheid gegeven om een project uit te schrijven op basis van mijn eigen interesses en zelf een onderzoekslijn uit te stippelen. Ik had iets gelezen over globale tractografie en zag daar wel een leuke uitdaging in, jij was meteen bereid om dat te steunen. Doorheen mijn doctoraat liet je me mijn eigen weg zoeken, met vallen en opstaan, en wanneer ik nood had aan kritische feedback stond je deur altijd open. Je wees op tekortkomingen, gaf suggesties voor aanvullingen en tilde het werk zo naar een hoger niveau. Als ik je advies in de wind sloeg mocht dat ook – achteraf bleek je doorgaans toch gelijk te hebben. Maar dankzij die vrijheid heb ik me kunnen ontwikkelen tot de zelfstandige, kritische onderzoeker die ik hoop te zijn. In elk geval hoop ik dat we ook in de komende jaren nog regelmatig kunnen samenwerken.

Ook prof. Stefan Sunaert, mijn co-promotor, wil ik graag bedanken voor zijn ondersteuning. Stefan, je hebt de voorbije jaren moeilijke tijden doorgemaakt en daardoor hebben we elkaar helaas weinig gezien. Maar wanneer je er was heb je me met je jarenlange ervaring als radioloog, je opmerkelijke technische kennis, en vooral je aanstekelijk enthousiasme vaak grote sprongen vooruit geholpen en nieuwe inzichten en ideeën bezorgd.

Professor Paul Suetens, het afdelingshoofd van onze groep, wil ik in het bijzonder bedanken om mij de kans te geven aan een doctoraat te starten. Paul, je hebt in het Medical Imaging Research Center (MIRC) een aangename en stimulerende onderzoeksomgeving gecreëerd, waarin brede expertise aanwezig is en verschillende disciplines elkaar vinden.

I also wish to thank invited jury members prof. J-Donald Tournier and dr. Marco Reisert. Marco, es ist eine Ehre und Freude dass Sie Teil der Jury sein wollen. My visit to Freiburg has been a pivotal week in my Ph.D., which greatly impacted this work. Your outstanding scientific record and your willingness to share ideas are a true example to many. Thank you for your trust and support.

Donald, many thanks for your comments on this thesis. It is a privilege to have you in my jury. You have been very generous to lend me early access to the MRtrix3 codebase, which came in at exactly the right time to develop the global tractography framework. I am very lucky to now consider myself part of its skilled team of developers. I am also very grateful for the postdoc position you offered me in your lab and eager to get started soon. I am sure we have interesting and fruitful times ahead of us.

Ik wil ook de overige juryleden, prof. Patrick Dupont, prof. Sabine Van Huffel en dr. Louise Emsell bedanken om het manuscript te beoordelen. Hun kritische vragen en opmerkingen hebben deze uiteindelijke tekst ontegensprekelijk verbeterd. Louise, a special thanks for reading and commenting on my thesis even during your pregnancy leave. I am delighted to hear that a healthy girl has now arrived and wish you and Wim all the best. Tot slot bedank ik ook juryvoorzitter prof. Paul Van Houtte om de verdediging in goede banen te leiden.

Vervolgens wil ik alle leden van de medical image computing (MIC) groep bedanken voor de voorbije jaren. In de eerste plaats prof. Dirk Vandermeulen om tijdens seminaries en groepsdiscussies steeds de puntjes op de i te zetten. Dirk, je bent een uomo universale met een scherp verstand en een brede interesse. Bedank ook Martine voor jullie gastvrijheid bij de barbecue en jullie aangename gezelschap op het jaarlijkse kerstfeest. Voorts dank ik Patricia Waege, Annitta De Messemaeker, Dominique Delaere en Bart De Dobbelaer voor hun administratieve en technische ondersteuning.

En dan zijn er alle collega's van MIC en MIRC waarmee ik doorheen de jaren heb mogen samenwerken. Dankzij hen is het Louvre de leuke werkplek die het is en konden we bij een tas koffie de nodige stoom aflaten. David, onze reizen in Japan en Amerika hebben veel leuke herinneringen nagelaten. Tussen de Sake en de IPA door was je het klankbord waarmee ik zelfs op mijn meest chaotische momenten mijn gedachten terug kon ordenen. Ik wens je veel succes met de eindsprint en twijfel er niet aan dat je je thesis binnenkort met verve gaat verdedigen. Tom, jou moet ik bedanken om mij op het pad naar neuroimaging te zetten, om me te leren klimmen, en om een goede vriend te zijn. Ik wens je eveneens veel succes met de eindfase van je doctoraat en de nog onbekende plannen daarna. Thijs, bedankt om mijn masterthesis nauwgezet te begeleiden en me zo tot de onderzoekswereld en DWI te introduceren. Catarina, your contagious good mood is more uplifting than even the largest pile of pastéis

de nata. Thanks for bringing the Portuguese sun to work on even the most rainy Belgian days. Janaki, thanks for all the moral support at times when it was much needed. Pieter, de onbetwiste karaoke-kampioen, bedankt om schwung in de conferenties te brengen en ons op Alaskan king crab te trakteren. Stijn, bedankt voor de zeiltochten. An, bedankt voor al je goede raad. Anke, Annemie, Babs, Brecht, Charlotte, Dirk, Dorothée, Dorothy, Dzemilla, Elke, Frederik, Gilles, Hans, Ine D., Ine S., Jaap, Jasmien, Jeroen, Jiarui, Johannes, Jonatan, Jose, Katleen, Laura, Leonardo, Maarten, Marjolein, Markus, Martijn, Martino, Mauro, Pedro, Peter, Philip, Ron, Sabine, Simon, Sofie, Thibo, Tom en Wouter, dankzij jullie vond ik steeds de nodige energie om door te zetten.

Daarnaast heb ik ook buiten Leuven heel wat nieuwe vrienden gemaakt via samenwerkingen en conferenties. Ik wil in het bijzonder Jelle, Steven, Ben, Dave, Rob, Max, Jimmy, Rami, Quinten, Gwendolyn, Gabriel, Timo, Chantal, Sjoerd, Maxime, Lisa, Andreas, Zehan, Elias, Bibek, Vladimir en Thomas bedanken voor de memorabele tijden op MICCAI, ISMRM of de EIBIR Summer School.

Om dit deel af te sluiten hou ik eraan om ook het Instituut voor Innovatie door Wetenschap en Technologie (IWT, doctoraatsbeurs SB121013) te bedanken voor de financiële steun waarmee dit doctoraat mogelijk gemaakt werd.

Vervolgens wil ik mijn vrienden en familie bedanken voor hun onvoorwaardelijke steun. Mama en papa, jullie hebben ons altijd alle kansen gegeven en ons geleerd om op eigen benen te staan. Bedankt om er altijd te zijn. Ellis en Eva, bedankt om thuis te laten opleven en mij met beide voeten op de grond te houden. Opa, zoals je ziet neem ik je advies om mijn leven lang naar school te gaan nogal letterlijk – deze thesis is voor jou. Oma, bedankt om mij te tonen wat sterkte is, nog meer sinds je er alleen voor staat. Oma en opa, bedankt voor jullie zorg en vrolijkheid, om altijd een warme tweede thuis te zijn.

Eindigen doe ik met de allerbelangrijkste: Liese, mijn rots in de branding. Lieve schat, zonder jouw steun, zorgzaamheid en toewijding zou dit niet gelukt zijn. We hebben binnenkort een beetje vakantie verdiend, en daarna starten we aan een nieuw avontuur.

Daan Christiaens
4 juli 2016

Abstract

Mapping the structural network topology of the human brain is a fundamental challenge in science, and one that may advance our understanding and treatment of neurological and neuropsychiatric disorders. Diffusion-weighted magnetic resonance imaging (DWI) is currently the only non-invasive technique for probing the structural connectivity in the brain in vivo. Its principle is based on indirect measurement of the diffusion anisotropy of water, which is correlated with tissue microstructure. Estimating the local geometry of axonal fibres then hinges on biophysical models of diffusion in white matter. Such local estimates can subsequently be integrated along the image to reconstruct global structural connections in the brain, a process known as tractography.

Many state-of-the-art DWI analysis methods build on strong model assumptions about the signal in white matter, which are hard to validate and may not generalize to other tissues and pathology. In this thesis, we therefore aim to reconstruct the local and global fibre configuration in brain white matter with as few prior assumptions about the microstructure as possible. Instead, we develop data-driven methodology, informed by spatial priors, population priors, and the signal itself.

From this perspective, we develop a global tractography framework that integrates a spatial prior on the continuity of white matter fibres into a minimal convolutive multi-tissue model for DWI in the brain, based on a fibre response function that is estimated from and thus adapted to the data at hand. In this method, local fibre orientation estimates inform the global track configuration and vice versa, hence integrating local and global scales into one Markov chain Monte Carlo optimization framework. Results show improved specificity of valid connections and maintain a quantitative correspondence between track density and the apparent fibre density in the data.

Secondly, we introduce population priors in the form of atlases of the local fibre orientation or of the global white matter bundle label to which individual fibres belong. As such, tractography in individual subjects is informed by common structure found across a cohort. Results indicate that such priors can reduce false positive tracks, thus improving specificity.

Finally, we develop a blind source separation technique for multi-shell DWI, decomposing the data as a convolutive mixture of nonnegative tissue orientation distribution functions and corresponding response functions, without assuming the latter as known thus fully unsupervised. In healthy human brain data, the resulting components are associated with white matter fibres, grey matter, and cerebrospinal fluid. This factorization is on par with state-of-the-art supervised methods, as demonstrated also in Monte-Carlo simulations evaluating accuracy and precision. In animal data and in the presence of edema, our method is able to recover unseen tissue structure, fully data-driven.

In summary, we developed local and global fibre reconstruction methods for DWI that improve over the state-of-the-art and extend to applications in preclinical data and pathology.

Beknopte samenvatting

Het structurele netwerk van het menselijk brein in kaart brengen is een fundamentele uitdaging in de wetenschap, en een die ons begrip en de behandeling van neurologische en neuropsychiatrische aandoeningen kan verbeteren. Diffusie-gewogen magnetische resonantie beeldvorming (diffusion-weighted imaging, DWI) is momenteel de enige niet-invasieve techniek om de structurele connectiviteit in de hersenen te onderzoeken in vivo. Het principe ervan is gebaseerd op een indirecte meting van de anisotrope diffusie van water in het weefsel, die gerelateerd is aan de onderliggende microstructuur. Op basis van een biofysisch model van diffusie in witte stof, kan hieruit een schatting worden bekomen voor de lokale configuratie van de axonale vezels. Dergelijke lokale schattingen kunnen vervolgens geïntegreerd worden doorheen het beeld om de globale, structurele connecties te reconstrueren, een proces gekend als tractografie.

Vele geavanceerde DWI analyse methoden bouwen op sterke modelaannames over het signaal in witte stof, welke moeilijk te valideren zijn en soms niet veralgemenen naar andere weefsels of pathologie. In deze thesis beogen we daarom om de lokale en globale wittestofbanen in het brein te reconstrueren met zo weinig mogelijk a priori veronderstellingen over de microstructuur. Daartoe hebben we data-gedreven methoden ontwikkeld die enkel gebruik maken van ruimtelijke voorkennis, voorkennis geleerd uit een populatie, en het signaal zelf.

Vanuit dat perspectief ontwikkelen we een globale tractografie methode waarin ruimtelijke voorkennis over de continuiteit van wittestofbanen geïntegreerd wordt met een minimaal, convolutief multi-weefsel model voor DWI in de hersenen, op basis van een vezel-responsfunctie die geschat wordt uit en dus aangepast is aan de data. In deze methode informeren lokale schattingen van de vezelrichting de globale track configuratie en vice versa, zodoende de lokale en globale schaal verenigend in één Markov-keten Monte-Carlo optimalisatiekader.

De resultaten tonen verbeterde specificiteit van het aantal geldige verbindingen en behouden een kwantitatief verband tussen de track-dichtheid en de schijnbare wittestofvezel-dichtheid in de data.

Vervolgens introduceren we populatie-gebaseerde voorkennis in de vorm van atlassen van de lokale vezelrichting of van globale labels van de wittestofbundels waartoe de individuele tracks behoren. Zodoende is de tractografie in individuen geïnformeerd door gemeenschappelijke structuur in een groep subjecten. De resultaten wijzen uit dat dergelijke voorkennis de specificiteit van tractografie kunnen verbeteren.

Tenslotte ontwikkelen we een blinde signaalscheidingstechniek voor multi-shell DWI, waarin we de data ontbinden als een convolutieve combinatie van niet-negatieve distributiefuncties van de lokale weefseloriëntatie en overeenkomstige responsfuncties, zonder die laatste als gekend te beschouwen en dus volledig ongesuperviseerd. In data van het gezonde menselijke brein zijn de resulterende componenten geassocieerd met wittestofbanen, grijze stof en cerebrospinaal vocht. Deze factorisatie is gelijkwaardig aan gesuperviseerde methoden, zoals aangetoond in Monte-Carlo simulaties om accuraatheid en precisie te evalueren. Omdat onze methode volledig data-gedreven is, is ze in staat om ongeziene weefselstructuur te ontdekken zoals in aanwezigheid van oedeem, en is ze ook toepasbaar op niet-humane data.

Samengevat hebben we methoden ontwikkeld voor lokale en globale reconstructie van de wittestofbanen uit DWI die de stand der techniek verbeteren en uitbreiden naar toepassingen in preklinische data en pathologie.

Abbreviations

AD	axial diffusivity
ADC	apparent diffusion coefficient
AF	arcuate fasciculus
AFD	apparent fibre density
AIC	Akaike information criterion
aPSF	apodized point spread function
ASD	autism spectrum disorder
BIC	Bayesian information criterion
CC	corpus callosum
CHARMED	composite hindered and restricted model of diffusion
CNMF	convex nonnegative matrix factorization
CNSF	convex nonnegative spherical factorization
CSD	constrained spherical deconvolution
CSF	cerebrospinal fluid
CST	corticospinal tract
CT	computed tomography
DKI	diffusion kurtosis imaging
dODF	diffusion orientation distribution function
DSI	diffusion spectrum imaging
DTI	diffusion tensor imaging
DWI	diffusion-weighted imaging
EPI	echo planar imaging
FA	fractional anisotropy
FLAIR	fluid-attenuated inversion recovery MRI

fMRI	functional magnetic resonance imaging
FOD	fibre orientation distribution
fODF	fibre orientation distribution function
FRT	Funk-Radon transform
GM	grey matter
GT	global tractography
HARDI	high angular resolution diffusion imaging
HCP	human connectome project
HMOA	hindrance-modulated orientational anisotropy
IB	invalid bundle
IC	invalid connection
IOFF	inferior occipitofrontal fasciculus
MCP	mean closest point
MD	mean diffusivity
MND	motor neurone disease
MRI	magnetic resonance imaging
MRS	magnetic resonance spectroscopy
MS	multiple sclerosis
NC	no connection
NMF	nonnegative matrix factorization
NMR	nuclear magnetic resonance
ODF	orientation distribution function
PD	proton density
PDF	probability distribution function
PET	positron emission tomography
PGSE	pulse gradient spin echo
PVE	partial volume effect
QBI	q-ball imaging
QP	quadratic programming
QSI	q-space imaging
RBF	radial basis function
RD	radial diffusivity
RF	response function

RJMCMC	reversible jump Markov chain Monte Carlo
RMS	root-mean-square
ROI	region-of-interest
SD	spherical deconvolution
SH	spherical harmonics
SLF	superior longitudinal fasciculus
SNR	signal-to-noise ratio
SSD	sum of squared differences
SVM	support vector machine
T1	T_1-weighted imaging
T2	T_2-weighted imaging
TDI	track density imaging
TOD	track orientation distribution
UF	uncinate fasciculus
VB	valid bundle
VC	valid connection
WM	white matter
WMQL	white-matter query language
ZH	zonal harmonics

Contents

List of Figures

List of Tables

Chapter 1

Introduction

1.1 The brain at micro- and macroscopic scale

The central nervous system consists of the brain and the spinal cord, and is responsible for processing sensory stimuli and controlling the actions taken in response. This thesis focuses exclusively on brain imaging, although the general principles apply to the spinal cord as well.

1.1.1 Brain histology

At the microscopic level, the brain comprises two closely interacting cellular networks, neuronal and neuroglial. The human brain contains approximately 10^{11} neurons and 10^{12} glial cells that each occupy about half of its volume [1].

Neurons

Neurons are the functional units of the brain, specialized in rapid signal integration and transmission. As illustrated in Fig. 1.1, a neuron consists of a cell body or soma that contains the nucleus, dendritic processes that receive information from other neurons, and an axon that conducts signals to other neurons. Axons extend from the cell body on a length scale of less than a millimeter to over 1 meter, and end in one or more synaptic terminals that transmit signals to other cells. Signal transmission relies on axonal conduction of action potentials, an electrochemical mechanism of fluctuations in Na^+ and

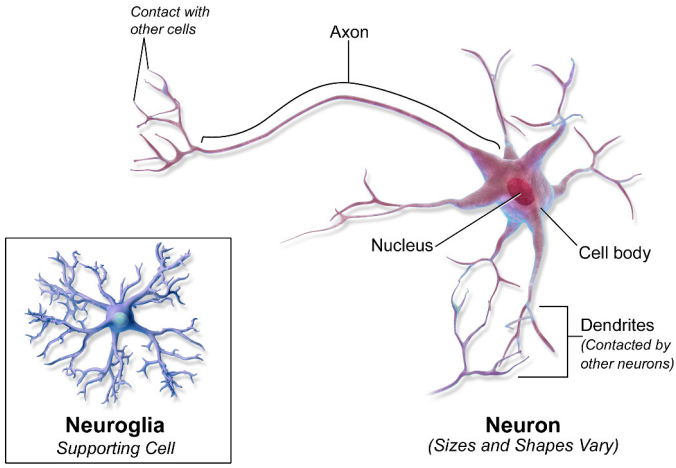

Figure 1.1: Neural tissue at the cellular level consists primarily of neurons and supporting neuroglial cells. Neurons have a cell body, a long extending axon that ends in synaptic connections to other cells, and dendrites that receive signals from the synapses of adjacent neurons. (Adapted from [2]; CC BY 3.0)

K^+ ion concentration across the cell membrane, which causes neurotransmitter release at the synapse to signal other cells. Rapid conduction of action potentials is strongly improved in the presence of myelin (see below).

Neuronal cell bodies aggregate in *grey matter* (GM), either in lamellar sheets or in localized groups, so-called nuclei and ganglia. Axonal fibres running in a common direction usually form compact bundles throughout *white matter* (WM) [1]. These neural fibres or fasciculi are in turn organized in larger white matter tracts, peduncles, or pathways.

Neuroglia

The brain contains three types of glial cells: astrocytes, oligodendrocytes, and microglia. Astrocytes are star-shaped cells that provide structural support to neurons and axons by forming a cellular scaffold. They also cater nutrients to the neurons, and control the ion composition of the extracellular space. In addition, astrocytes propagate Ca^{2+} waves in response to neurotransmitter activation, making them an integral, yet not fully understood, part of signal transduction in the nervous system [1]. Oligodendrocytes are neuroglia that form myelin sheets as concentric layers of lipid material surrounding the axons.

Myelin provides electrochemical insulation between successive nodes of Ranvier, sections of exposed cell membrane, which is critical for rapid propagation of action potentials. Finally, microglia are smaller glial cells that play an active role upon brain injury and restoration [1].

1.1.2 Brain anatomy

At a macroscopic level, the brain is subdivided into the brain stem, the cerebellum, the diencephalon and the cerebrum (cf. Fig. 1.2). The brain and spinal cord are suspended in *cerebrospinal fluid* (CSF) and surrounded by three membranes: the outer dura mater, the arachnoid lined with blood vessels, and the inner pia mater. CSF also extends into interconnected cavities between the main parts of the brain, the so called ventricles. The brain stem links the spinal cord to the cerebrum and comprises the medulla oblongata, the pons, and the midbrain including the cerebral peduncles. The cerebellum is a dorsal part of the brain mostly associated with motor control. It consists of a thin outer grey matter layer that contains over 50% of all neurons in the brain, which covers a tree-like white matter structure (arbor vitae) formed by axonal connections to the cortex [1]. The diencephalon comprises the thalamus and the hypothalamus, which contain GM nuclei associated with sensory and motor signals, sleep, and autonomic functions. The cerebrum consists of left and right hemispheres, interconnected with a thick white matter structure known as the corpus callosum. The cerebral cortex, an outer GM layer, is organized in a folding pattern of gyri and sulci to increase the surface area. The primary sulci subdivide each cerebral hemisphere into frontal, temporal, parietal, and occipital lobes.

The WM within the cerebrum contains neural fibres connecting GM regions to other gyri and to the spinal cord and the rest of the body via the brain stem. These pathways are subdivided in commissural, association, and projection tracts. Commissural fibres connect contralateral regions across both hemispheres. The main commisural tracts are the corpus callosum and the anterior and posterior commissure. Association pathways affiliate separate cortical regions within the same hemisphere, with primarily anterior-posterior connections [4]. Examples include the cingulum bundles, the fornix, the arcuate fasciculus, and the superior and inferior longitudinal fasciculus. Finally, projection fibres such as the corticospinal tract and the cerebellar peduncles connect cortical areas to subcortical structures and the brain stem.

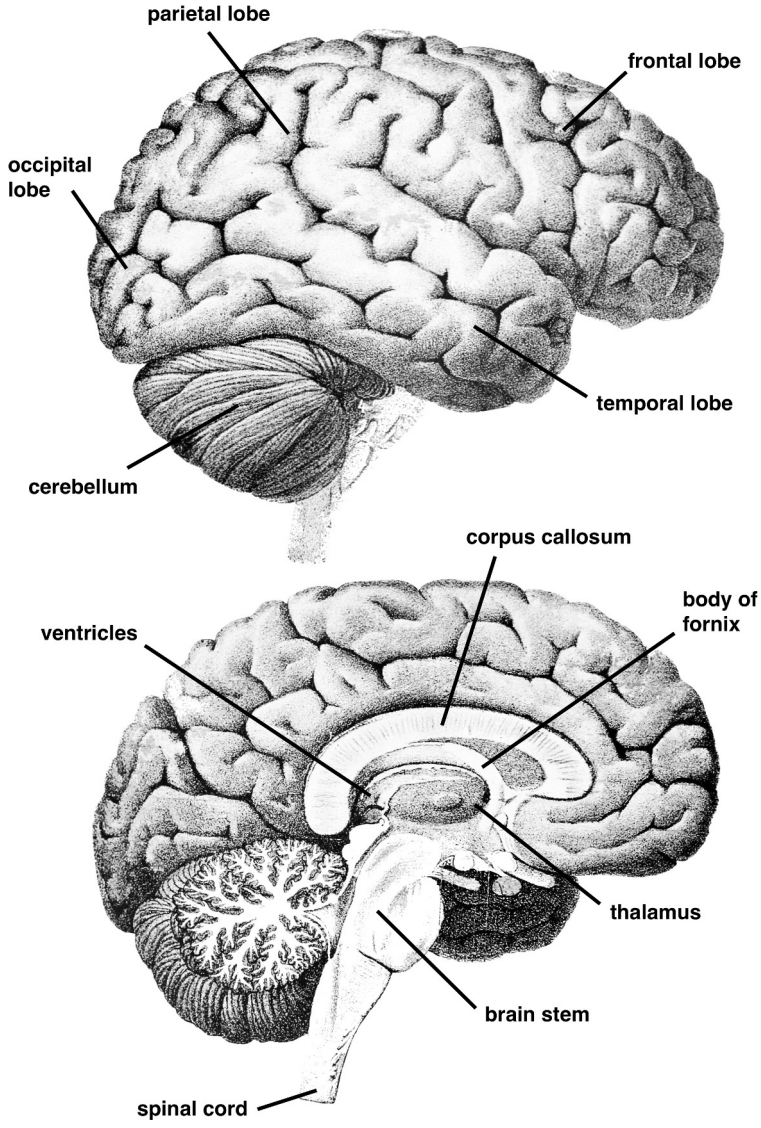

Figure 1.2: Lateral and mesial view of the human brain. (Adapted from [3]; public domain)

1.2 Neuroimaging in research and clinical practice

Neurological and neuropsychiatric disorders may affect the brain at both local and global scale. Some disorders, such as multiple sclerosis (MS), dementia, and motor neurone disease (MND), induce microstructural tissue changes, often targeted to certain cell types or brain regions. Others, such as autism spectrum disorder (ASD) and schizophrenia, presumably affect the network of brain connections, the so-called *connectome* [5], associated with language, emotion, consciousness, etc. Diagnosis and treatment follow-up of neurological disorders is often hindered by the inaccessibility and sheer complexity of the brain.

Imaging therefore plays a vital role in research and clinical practice alike, for diagnosing disease processes, understanding their underlying mechanisms, and evaluating treatment plans. In addition to computed tomography (CT) and positron emission tomography (PET), magnetic resonance imaging (MRI) is of particular relevance for it offers a wide range of image contrasts without subjecting the patient to harmful radiation. Common MRI modalities such as T_1-weighted, T_2-weighted, and proton density (PD) imaging facilitate assessing brain anatomy and discriminating healthy tissues and pathology. Beyond these structural MRI measures, several advanced MRI techniques have been developed that are sensitive to blood flow [6], perfusion [7], or oxygenation [8]. The latter is especially used in functional MRI (fMRI), either for imaging activated brain regions in response to certain tasks or for disentangling the functional networks of the brain from time-correlated activation under resting-state conditions [9–11].

In addition, several MRI modalities capture information on a sub-voxel scale, including diffusion-weighted imaging (DWI) [12] and myelin water imaging [13]. In DWI, the MR signal is sensitized to the continuous random motion of water molecules due to diffusion. Because this molecular motion is hindered or restricted by cell membranes and intracellular organelles, the acquired signal is indicative of tissue microstructure. For example, a nearly two-fold drop of the apparent diffusion coefficient was observed in acute stroke [14]. Moreover, the directional dependence of diffusion and the DWI signal can be exploited to characterize tissue geometry, which is particularly relevant in white matter due to the large anisotropy of neural fibres [15]. As such, DWI is for instance sensitive to demyelination in MS lesions [16–19]. Additionally, these local measures can be integrated over a longer spatial scale, tracing neuronal pathways and structural connections in the brain in a process known as tractography [20, 21].

DWI and neuroimaging in general thus facilitate detecting and studying neural disorders in vivo, non-invasively. In research, MRI provides invaluable information on disease mechanisms and progression, analyzed either cross-sectionally between patient and control groups, or longitudinally across

subsequent time points [22]. The effectiveness of drugs and treatment options can be similarly assessed. In clinical practice, defining imaging *biomarkers* that can detect disease development at an early stage is of particular importance.

1.3 Aims and objectives

This thesis focuses primarily on diffusion-weighted imaging and the unique means it provides to probe white matter fibre structure in the brain. As we will introduce in more detail in Chapter 2, analysis of DWI data entails particular challenges stemming from limited resolution, low signal-to-noise ratio, and the complex fibre geometry of the brain itself, which complicate robust estimation of the local fibre geometry. This estimation generally depends on biophysical models that relate white matter microstructure to the measured diffusion-weighted MR signal, based on strong model assumptions of the signal contributions of independent cellular compartments. Not only are these assumptions hard to validate, they may not generalize to other tissue types and pathology. Our overarching aim is therefore to make as few prior assumptions about the tissue microstructure as possible, adopting a data-driven approach instead. The envisaged methodology is then informed by spatial priors, population priors, and the DWI signal itself.

While tractography methods for reconstructing WM pathways and connectivity at the global scale are guided by local estimates in each voxel, vice versa the local reconstruction may also be informed by more global spatial priors on the continuity of white matter fibres. The first objective of this thesis is therefore to develop analysis methods and computational strategies for reconstructing WM fibre structure at the image scale, unifying local model fitting and global tractography.

In addition, the expected fibre configuration and its variability can be learned from a cohort of subjects with normal anatomy, represented as a population atlas. Such an atlas may subsequently be used to guide tractography to the global optimum and exclude implausible fibres. Our second objective is hence to incorporate population-based atlas priors in global tractography and explore their benefits and weaknesses.

Finally, a local tissue model may be learned from the signal across all voxels in the image, avoiding the need for parametric models or preprocessing pipelines. Our third objective is therefore to develop unsupervised tissue decomposition techniques based on minimal assumptions about the signal and the imaging process.

1.4 Main contributions

The main contributions of this thesis are the development and enhancement of global tractography algorithms for white matter fibre reconstruction, the investigation of population priors in this framework, and the development of a fully unsupervised local tissue decomposition strategy in DWI. Specifically:

- We incorporate a multi-tissue spherical convolution model in global tractography, based on a fibre response function estimated from and thus adapted to the data at hand [23].
- We investigate the use of a local track orientation prior, learned from a database of representative subjects, in global tractography [24].
- We incorporate a label prior in global tractography, which categorizes individual tracks as part of macroscopic white matter bundles. Aside from providing a segmentation, such prior may also improve the track reconstruction itself by excluding false positive tracks [25].
- We introduce a novel method for group-wise spatial normalization of full brain tractography [26].
- We develop a blind source separation technique for multi-shell DWI data, decomposing the data as a convolutive mixture of nonnegative tissue components [27].

As we will highlight in subsequent chapters, these contributions have applications for both local image biomarkers and global connectivity mapping.

1.5 Outline

In Chapter 2, we introduce the concepts and physical principles behind diffusion-weighted imaging. We give an overview of the various signal models that have been explored in literature, and how they are related to tissue and microstructure properties. Particular attention goes to spherical deconvolution techniques that are a cornerstone of this thesis. Furthermore, we introduce streamline and global tractography methods, and highlight the main challenges and limitations these entail.

Chapter 3 describes a novel global tractography framework that explicitly accounts for partial volume effects between adjacent tissue types. This tractography method is evaluated in simulated phantom data with known ground truth and in vivo in human brain data.

Chapter 4 explores the use of population priors, learned from a population of normal subjects, in global tractography. We investigate both local priors on the track orientation, and global label priors segmenting white matter fibre bundles at larger scale, and evaluate their strengths and weaknesses in simulations and human brain data.

Chapter 5 develops population-based atlases of tractography. We introduce a novel method for track set registration that, in contrast to the state of the art, enables deformable, group-wise registration of full brain track sets. In addition, we describe an approach for automated labelling of fibre bundles in population data.

In Chapter 6, we return to the local scale and introduce a nonnegative factorization method that decomposes DWI data in every voxel in tissue-related response functions and local orientation distribution functions, fully unsupervised. The presented method is validated in silico and demonstrated in brain data with and without pathology, in vivo and ex vivo.

Finally, in Chapter 7 we summarize the main conclusions of our work, outline the remaining challenges, and provide perspectives on future work.

Chapter 2

Diffusion-weighted imaging: concepts, challenges, and limitations

2.1 Brownian motion and diffusion

Each molecule in a fluid is in constant motion due to its thermal energy, and changes direction upon each collision with other molecules. In a homogeneous medium without restrictions, the resulting particle trajectory describes a random walk: a process of statistically independent steps as illustrated in Fig. 2.1. This process is known as Brownian motion, named after Robert Brown [28], a botanist who first observed the random motion of pollen grains suspended in water under a microscope. A rigorous explanation of this phenomenon was developed independently by Albert Einstein [29] and Marian Smoluchowski [30]. Their theory was experimentally verified by Jean-Baptiste Perrin in 1909, confirming the kinetic theory of gases and the existence of atoms, for which he was awarded the Nobel prize in Physics in 1926.

Einstein introduced the probability distribution function (PDF) that a particle at position $\mathbf{r}_0$ at time $t = 0$ displaces to position $\mathbf{r}$ in time $t = \tau$: $P(\mathbf{r}|\mathbf{r}_0, \tau)$. He then showed that

$$\frac{\partial P(\mathbf{r}|\mathbf{r}_0, \tau)}{\partial t} = D \, \nabla^2 P(\mathbf{r}|\mathbf{r}_0, \tau), \tag{2.1}$$

where the diffusion coefficient $D = k_B T/\gamma$ with temperature T, Bolzmann's constant k_B, and viscous drag coefficient γ. It should come as no surprise that Einstein's diffusion equation has the same form as Fick's second law of diffusion, which was derived from the phenomenological observation that the flux in a solution is proportional and opposite to the concentration gradient (his first law), and the mass conservation principle [31].

For a single particle in a homogeneous medium, the solution to the diffusion equation is a 3-dimensional Gaussian distribution of the net displacement $\hat{\mathbf{r}} = \mathbf{r} - \mathbf{r}_0$ with standard deviation $\sigma = \sqrt{6D\tau}$. As such, the diffusion coefficient D is related to the root-mean-square (RMS) displacement of a particle in a time interval τ:

$$D = \frac{1}{6\tau} \left\langle \hat{\mathbf{r}}^T \, \hat{\mathbf{r}} \right\rangle, \tag{2.2}$$

where the brackets $\langle . \rangle$ denote the ensemble average, i.e., the average for an infinite number of particles. D is directionally independent and is therefore called the isotropic diffusion coefficient.

For water at 37.5 °C, D is approximately $2.5\,\mu\mathrm{m}^2/\mathrm{ms}$. We should appreciate how fortuitous this is, for with a different value the field of diffusion MRI – and this thesis – would not have been possible. Indeed, the diffusion coefficient effectively provides a length scale on the order of 10–50 μm for diffusion times $\tau \sim$ 10–200 ms measurable with modern MR scanners – far below the imaging resolution. Moreover, this length scale is generally commensurate with cell dimensions [32], and thus enables to probe biological tissue structure on the micrometer scale.

Biological tissue is often highly heterogeneous in the presence of cell membranes and intracellular organelles that reduce the diffusion of water molecules. White matter, for instance, consists of several compartments, e.g., intra- and extracellular space, and barriers, particularly myelin, that hinder or restrict diffusion [15]. Hindrance refers to reduced molecular mobility in general, whereas restricted diffusion specifically denotes that molecules are confined to a bounding structure on the time scale of the measurement. In addition, boundaries between these compartments may have coherent directional structure, hindering diffusion in one direction but less in the other. Therefore, the diffusion PDF in white matter will not be Gaussian, nor isotropic.

Except for CSF in the ventricular chambers, the measured root-mean-square displacement of water in biological tissue will hence be lower than its expected diffusion coefficient. To underscore that this effect relates to the underlying tissue rather than the diffusion process itself, Le Bihan *et al.* [12] coined the term *apparent* diffusion coefficient (ADC).

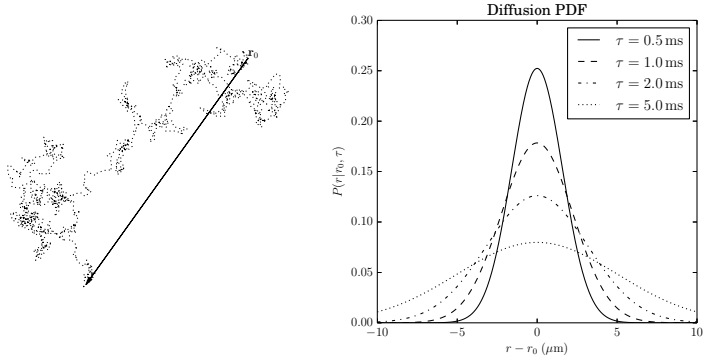

Figure 2.1: Left: 2-Dimensional random walk of a particle due to Brownian motion from position $\mathbf{r}_0$ at time 0 to position $\mathbf{r}$ at time τ. Right: Probability distribution function of the total displacement in an isotropic, homogeneous medium. In this case, the diffusion PDF is a Gaussian who's variance scales linearly with time.

To account for anisotropy, Basser *et al.* [33] subsequently proposed the apparent diffusion tensor, which generalizes (2.2) by taking the covariance matrix instead of the root-mean-square displacement:

$$\mathbf{D} = \frac{1}{6\tau} \left\langle \hat{\mathbf{r}}\, \hat{\mathbf{r}}^T \right\rangle = \begin{pmatrix} D_{xx} & D_{xy} & D_{xz} \\ D_{xy} & D_{yy} & D_{yz} \\ D_{xz} & D_{yz} & D_{zz} \end{pmatrix}. \tag{2.3}$$

The diffusion tensor $\mathbf{D}$ is a symmetric, positive-definite matrix [33, 34]. The ADC in an arbitrary direction $\mathbf{u}$ is then evaluated as $\mathbf{u}^T\, \mathbf{D}\, \mathbf{u}$.

2.2 Diffusion-weighted imaging

Diffusion-weighted imaging (DWI) is currently the sole non-invasive technique to measure water diffusion in vivo. DWI is based on the physical principle of nuclear magnetic resonance (NMR), simultaneously described by Bloch [35] and Purcell *et al.* [36] in 1946. The basic principle behind NMR is to align proton (^{1}H) spins in a strong magnetic field and measure the response to a perturbation of their alignment with an electromagnetic field. This response characterizes the proton density, as well as surrounding spin-spin and spin-lattice interactions [37]. Lauterbur [38] later studied the use of magnetic field gradients to encode spatial information in 2D-images. Mansfield [39]

subsequently introduced the echo-planar imaging (EPI) acquisition sequence. Their discoveries led to the development of magnetic resonance imaging (MRI), for which they received the Nobel prize in Physiology and Medicine in 2003.

A detailed discussion of NMR and MRI goes beyond the scope of this text. The interested reader is referred to McRobbie *et al.* [37].

2.2.1 The Stejskal-Tanner sequence

Even before the invention of MRI, Stejskal and Tanner [40] developed the pulse gradient spin echo (PGSE) sequence, which measures the diffusion of water molecules along the direction of a *diffusion gradient* $\mathbf{G}$. The Stejskal-Tanner sequence is shown in Fig. 2.2. It adds two rectangularly shaped gradient pulses to the EPI sequence, symmetrically positioned around the 180° RF pulse. The diffusion gradients are directed along $\mathbf{G}$, switched on during a time δ, and spaced at a time distance Δ.

The first gradient pulse induces a phase shift φ_1 of the spin transverse magnetization, and is therefore called the *dephasing gradient*. The spin position $\mathbf{r}(t=0) = \mathbf{r}_0$ is assumed to be constant during the pulse duration $\delta \ll \Delta$.

$$\varphi_1 = \gamma \int_0^{\delta} \mathbf{G} \cdot \mathbf{r}(t)\, \mathrm{d}t = \gamma\, \delta\, \mathbf{G} \cdot \mathbf{r}_0, \tag{2.4}$$

where $\gamma = 2\pi \cdot 42.576\,{}^{\mathrm{MHz}}\!/_{\mathrm{T}}$ is the gyromagnetic ratio of ^{1}H [37]. The phase φ_1 of each spin now depends on its original position along the gradient direction. The 180° RF pulse subsequently inverts the spins and a second, identical gradient pulse refocuses the spins. As such, this *rephasing gradient* induces a new phase shift φ_2 of opposite sign:

$$\varphi_2 = -\gamma \int_{\Delta}^{\Delta+\delta} \mathbf{G} \cdot \mathbf{r}(t)\, \mathrm{d}t = -\gamma\, \delta\, \mathbf{G} \cdot \mathbf{r}, \tag{2.5}$$

where $\mathbf{r}(t=\Delta) = \mathbf{r}$ is again assumed constant. The net induced phase shift after the full sequence is given by

$$\varphi = \varphi_1 + \varphi_2 = -\gamma\, \delta\, \mathbf{G} \cdot (\mathbf{r} - \mathbf{r}_0). \tag{2.6}$$

The spins that did not experience diffusion ($\mathbf{r} = \mathbf{r}_0$) in the time Δ have a net phase shift $\varphi = 0$. For spins that did change location due to Brownian motion, on the other hand, the net phase shift $\varphi \neq 0$. Note that, due to the inner product, only position changes along the direction of $\mathbf{G}$ are detected.

The loss of phase coherence due to diffusion leads to attenuation of the spin-echo signal S [41, 42]. Define S_0 as the signal intensity in the absence of a diffusion gradient, i.e., $\|\mathbf{G}\| = 0$. As in the standard EPI sequence, S_0 depends primarily

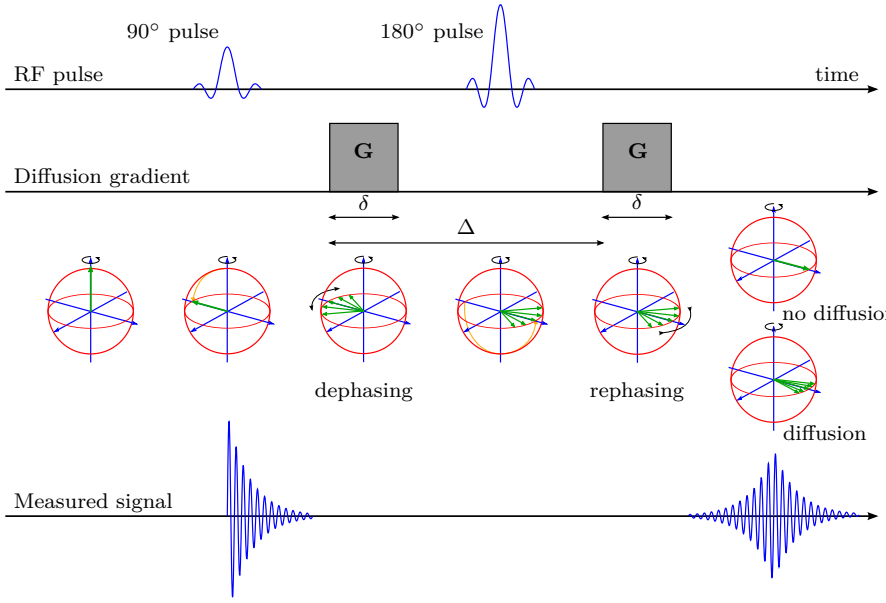

Figure 2.2: Scheme of the Stejskal-Tanner acquisition sequence for diffusion-weighted imaging. From left to right: (1) all spins are aligned in a strong magnetic field along the vertical axis of a rotating frame; (2) a 90° RF pulse maps the spins onto the transverse plane; (3) a magnetic field gradient in direction $\mathbf{G}$ causes *dephasing* of the proton spins; (4) a 180° RF pulse flips the proton spins to the opposite side of the transverse plane; (5) a second diffusion gradient causes *rephasing* of the proton spins; (6) signal readout at maximal rephasing, in case of diffusion, the proton spins are not completely refocused, resulting in signal loss.

on the T_2 relaxation time. The signal attenuation due to diffusion then equals the ensemble average phase shift across all spins in the voxel:

$$\frac{S}{S_0} = \left\langle e^{i\varphi} \right\rangle \leq 1. \tag{2.7}$$

Under the narrow pulse approximation $\delta \ll \Delta$, the ensemble average is explicitly computed by means of the diffusion PDF

$$\frac{S(\mathbf{q},\tau)}{S_0} = \int_{\mathbb{R}^3} P(\mathbf{r} \,|\, \mathbf{r}_0, \tau) e^{-2\pi i \mathbf{q}\cdot(\mathbf{r}-\mathbf{r}_0)} \mathrm{d}\mathbf{r} = \mathcal{F}\{P(\mathbf{r} \,|\, \mathbf{r}_0, \tau)\}\,, \tag{2.8}$$

where $\mathbf{q} = \gamma\delta\mathbf{G}/2\pi$. Introducing the vector $\mathbf{q}$ results in a rather elegant relation commonly referred to as the Stejskal-Tanner equation: the signal attenuation as a function of $\mathbf{q}$ equals the Fourier transform of the diffusion PDF.

2.2.2 Q-space imaging

The Fourier relation derived in the previous section is valid for any diffusion gradient $\mathbf{G}(t)$ if the vector $\mathbf{q}$ is generalized to

$$\mathbf{q} = \frac{\gamma}{2\pi} \int_0^\delta \mathbf{G}(t) \mathrm{d}t. \tag{2.9}$$

By acquiring a large collection of images for different diffusion-sensitizing gradient strengths and directions, a full sample of the q-space, the frequency spectrum of the diffusion propagator in every voxel, is obtained. The diffusion PDF can subsequently be computed as the inverse Fourier transform of the acquired data in each voxel. This is the principle of q-space imaging (QSI) [43, 44], also known as diffusion spectrum imaging (DSI) [45]. The concept of q-space bears an elegant analogy with k-space, the spatial frequency spectrum of images in structural MRI. Hence, a full QSI dataset effectively contains 6-dimensional data: 3 dimensions in k-space, related to the image space, and another 3 dimensions in q-space, related to the diffusion PDF.

In practice, the applicability of QSI is impeded by the required gradient strength and by the time constraints of the acquisition. Various suboptimal sampling schemes have therefore been proposed, which are discussed in Section 2.3.

2.2.3 Gradient strength and b-value

In their pioneering work on diffusion-weighted imaging, Le Bihan *et al.* [12] introduced an alternative parametrization of q-space that remains popular to this day. They define a unit vector $\mathbf{g}$ along the direction of the diffusion sensitizing gradient, and propose a diffusion weighting factor b that characterizes the strength and duration of that gradient. Given a fixed diffusion time τ,

$$\mathbf{g} = \frac{\mathbf{q}}{\|\mathbf{q}\|} = \frac{\mathbf{G}}{\|\mathbf{G}\|} \tag{2.10}$$

$$b = \tau \|\mathbf{q}\|^2 \tag{2.11}$$

and

$$\mathbf{q} = \|\mathbf{q}\| \cdot \mathbf{g} = \sqrt{\frac{b}{\tau}}\, \mathbf{g} \quad . \tag{2.12}$$

For the Stejskal-Tanner PGSE sequence, the b-value becomes

$$b = \gamma^2 \delta^2 \left(\Delta - \frac{\delta}{3} \right) \|\mathbf{G}\|^2 \quad , \tag{2.13}$$

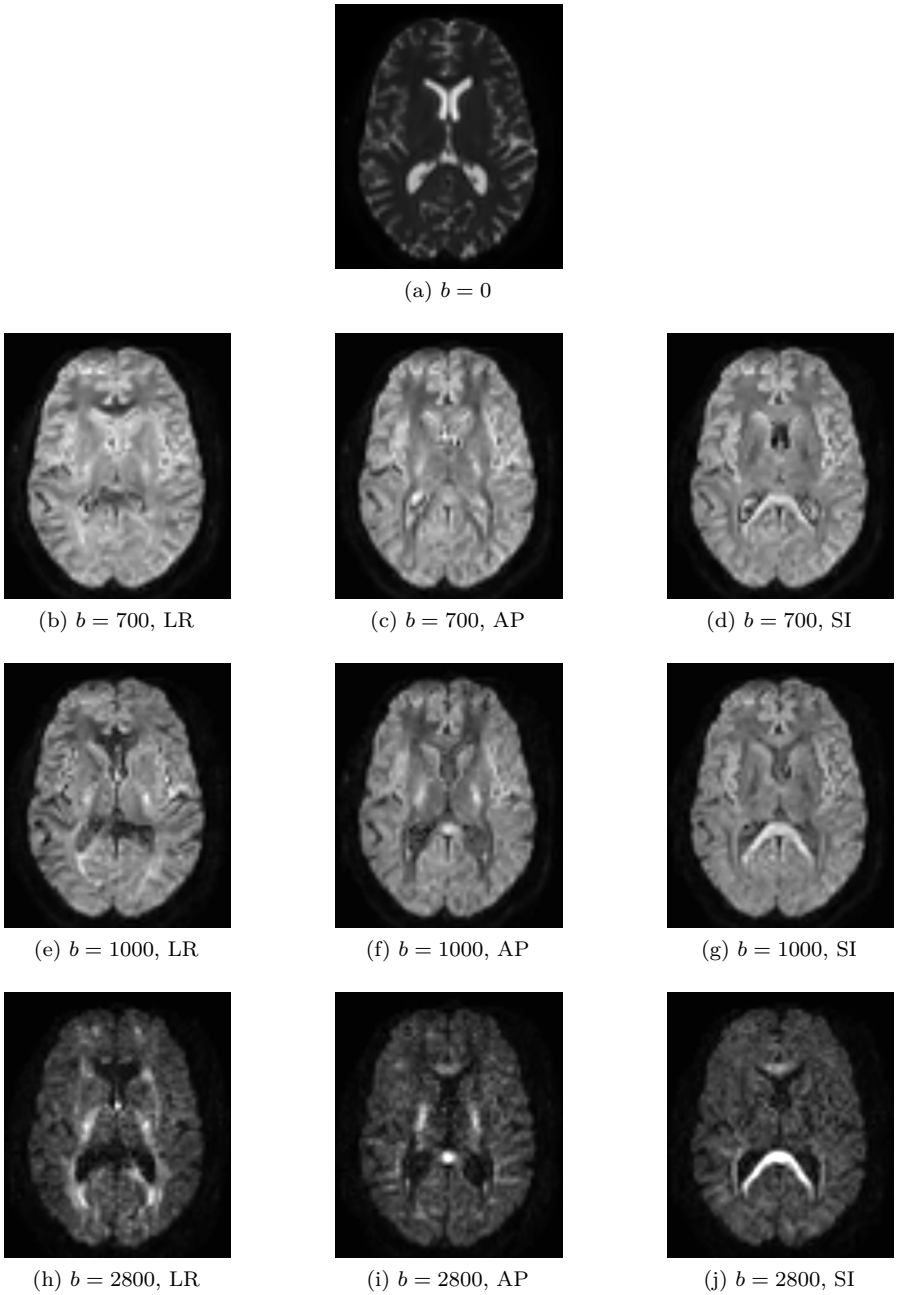

(a) $b = 0$

(b) $b = 700$, LR (c) $b = 700$, AP (d) $b = 700$, SI

(e) $b = 1000$, LR (f) $b = 1000$, AP (g) $b = 1000$, SI

(h) $b = 2800$, LR (i) $b = 2800$, AP (j) $b = 2800$, SI

Figure 2.3: DWI contrast obtained for varying diffusion sensitizing gradient encoding $\mathbf{G}$. Rows: gradient strength (b-value). Columns: gradient direction along left-right (LR), anterior-posterior (AP), and superior-inferior (SI) axes.

and comprises all characteristics of the diffusion sensitizing gradient [12]. The b-value is expressed in $^{s}/_{mm^2}$. Typical values range from $0\,^{s}/_{mm^2}$ to $4000\,^{s}/_{mm^2}$. At high b-values, the signal is lower but the angular contrast between different gradient directions increases, as shown in Fig. 2.3.

2.3 Signal modelling

2.3.1 Diffusion tensor imaging

If the diffusion PDF is assumed to be Gaussian, the Stejskal-Tanner equation (2.8) can be solved analytically, and we obtain

$$S(\mathbf{q},\tau) = S_0\, e^{-\tau \mathbf{q}^T \mathbf{D} \mathbf{q}} \quad , \tag{2.14}$$

or equivalently

$$S(b,\mathbf{g}) = S_0\, e^{-b \mathbf{g}^T \mathbf{D} \mathbf{g}} \quad . \tag{2.15}$$

The scalar $\mathbf{g}^T\mathbf{D}\mathbf{g}$ measures the apparent diffusion coefficient (ADC) along gradient direction $\mathbf{g}$. From (2.15), it follows that the ADC is linearly proportional to the logarithm of the signal attenuation:

$$\ln\left(\frac{S(b,\mathbf{g})}{S_0}\right) = -b\,\mathbf{g}^T\,\mathbf{D}\,\mathbf{g} = -b\,\mathrm{ADC} \quad . \tag{2.16}$$

In diffusion tensor imaging (DTI) [33], the elements of the diffusion tensor D are estimated from ADC measurements in a large number of gradient directions $\mathbf{g}_i = (g_{ix}, g_{iy}, g_{iz})$. This is most commonly achieved as the least-squares solution to a set of linear equations

$$\mathbf{B}\boldsymbol{\beta} = \boldsymbol{\sigma} \quad , \tag{2.17}$$

where vectors

$$\boldsymbol{\beta} = (\ln S_0, D_{xx}, D_{xy}, D_{xz}, D_{yy}, D_{yz}, D_{zz}) \quad ,$$

$$\boldsymbol{\sigma} = (\ln S(b,\mathbf{g}_1), \ln S(b,\mathbf{g}_2), \ldots, \ln S(b,\mathbf{g}_N)) \quad ,$$

and the so-called b-matrix [46]

$$\mathbf{B} = \begin{bmatrix} 1 & -bg_{1x}^2 & -2bg_{1x}g_{1y} & -2bg_{1x}g_{1z} & -bg_{1y}^2 & -2bg_{1y}g_{1z} & -bg_{1z}^2 \\ 1 & -bg_{2x}^2 & -2bg_{2x}g_{2y} & -2bg_{2x}g_{2z} & -bg_{2y}^2 & -2bg_{2y}g_{2z} & -bg_{2z}^2 \\ \vdots & \vdots & \vdots & \vdots & \vdots & \vdots & \vdots \\ 1 & -bg_{Nx}^2 & -2bg_{Nx}g_{Ny} & -2bg_{Nx}g_{Nz} & -bg_{Ny}^2 & -2bg_{Ny}g_{Nz} & -bg_{Nz}^2 \end{bmatrix} .$$

The b-matrix is of full rank and a unique solution can be computed if at least 6 diffusion-weighted images are acquired at non-collinear gradient directions, in addition to at least one image of different b-value, typically at $b = 0\,\mathrm{s/mm^2}$. For a larger number of gradients, the tensor estimation will be more robust to noise. Studies have shown that at least 30 unique gradient directions are needed to obtain a robust estimation of the tensor orientation [47, 48].

Geometric interpretation

The diffusion tensor $\mathbf{D}$ is the covariance matrix of a 3-dimensional Gaussian diffusion PDF. The iso-surface of this PDF is an ellipsoid described by $\mathbf{u}^T\mathbf{D}\mathbf{u}\ \forall \mathbf{u} \in \mathbb{S}_2$. Its principal axes and the diffusivity along those axes are defined with the eigenvalue decomposition of the diffusion tensor:

$$\mathbf{D} = \mathbf{E}\,\mathbf{\Lambda}\,\mathbf{E}^T = \begin{pmatrix}\mathbf{e}_1 & \mathbf{e}_2 & \mathbf{e}_3\end{pmatrix} \begin{pmatrix}\lambda_1 & 0 & 0\\ 0 & \lambda_2 & 0\\ 0 & 0 & \lambda_3\end{pmatrix} \begin{pmatrix}\mathbf{e}_1 & \mathbf{e}_2 & \mathbf{e}_3\end{pmatrix}^T, \tag{2.18}$$

with $\lambda_1 \geq \lambda_2 \geq \lambda_3$ the eigenvalues of $\mathbf{D}$ and $\mathbf{e}_i$ the corresponding eigenvectors. As $\mathbf{D}$ is a real, symmetric matrix, its eigenvalues are real and its eigenvectors are orthonormal. The principal eigenvector $\mathbf{e}_1$ is directed along the axis of largest diffusion. The corresponding eigenvalue λ_1 is the apparent diffusion coefficient along this direction.

DTI parameters

Additionally, a number of scalar measures have been defined from the eigenvalue decomposition. As these measures only depend on the eigenvalues, not the eigenvectors, they are invariant to rotation.

Mean diffusivity (MD) is the average ADC across all directions:

$$\mathrm{MD} = \frac{\lambda_1 + \lambda_2 + \lambda_3}{3} = \bar{\lambda} \quad , \tag{2.19}$$

which also equals the mean of the diagonal elements of the diffusion tensor, i.e., the trace divided by 3.

Axial diffusivity (AD) is the ADC along the principal axis $\mathbf{e}_1$:

$$\mathrm{AD} = \lambda_1 \quad . \tag{2.20}$$

Radial diffusivity (RD) is the mean ADC in the radial direction, i.e., the plane perpendicular to the principal direction, spanned by $\mathbf{e}_2$ and $\mathbf{e}_3$:

$$\mathrm{RD} = \frac{\lambda_2 + \lambda_3}{2} \quad . \tag{2.21}$$

Fractional anisotropy (FA) is defined as

$$\mathrm{FA} = \frac{\mathrm{std}(\lambda_i)}{\mathrm{rms}(\lambda_i)} = \sqrt{\frac{3}{2}} \frac{\sqrt{(\lambda_1 - \bar{\lambda})^2 + (\lambda_2 - \bar{\lambda})^2 + (\lambda_3 - \bar{\lambda})^2}}{\sqrt{\lambda_1^2 + \lambda_2^2 + \lambda_3^2}} \quad . \tag{2.22}$$

The FA is scaled within the unit range, and quantifies the amount of anisotropy. For isotropic diffusion, the FA equals 0. For cigar shaped or pancake shaped diffusion tensors, the FA approaches 1.

In addition, the principal eigenvector $\mathbf{e}_1$ is often visualized in a directionally encoded colour FA map (DEC-FA) [49]. By convention, red indicates the left-right axis, green indicates the anterior-posterior axis, and blue indicates the inferior-superior axis. The DEC-FA is the RGB image obtained by projecting $\mathrm{FA} \cdot \mathbf{e}_1$ onto this reference frame. These DTI metrics are depicted in Fig. 2.4.

2.3.2 Diffusion kurtosis imaging

Due to the presence of restricted compartments, the diffusion signal will generally not be Gaussian. Diffusion kurtosis imaging (DKI) [50, 51] is a method to estimate excess kurtosis as a metric of non-Gaussianity of the diffusion PDF. For any gradient direction, (2.16) is extended to

$$\ln\left(\frac{S(b, \mathbf{g})}{S_0}\right) = -b\,D + \tfrac{1}{6} b^2 D^2 K + \mathcal{O}(b^3) \quad , \tag{2.23}$$

where D is the apparent diffusion coefficient and K is the apparent diffusional kurtosis in that gradient direction [50]. Equation 2.23 is essentially a Maclaurin series expansion of the log-attenuation in powers of b. This description was subsequently related to the cumulant expansion of the diffusion propagator [52, 53]. The second-order cumulant is the variance of the diffusion PDF and thus related to the ADC via (2.2). The fourth-order cumulant relates to kurtosis. All odd-order cumulants are zero due to the symmetry of the diffusion PDF.

DKI is similarly extended to model the full directionality of the signal with the use of the kurtosis tensor, a fully symmetric $3 \times 3 \times 3 \times 3$ tensor that contains 15 unique elements, resulting in 21 parameters in total. Estimating these parameters requires at least 3 distinct b-values and 15 unique gradient directions [50, 54].

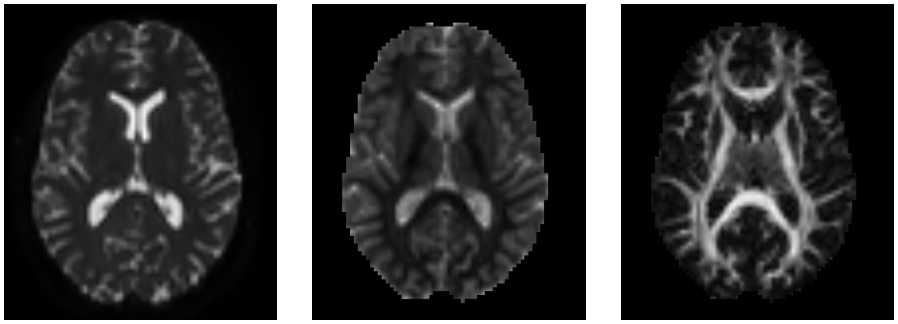

(a) $b = 0$ image (b) Mean diffusivity (MD) (c) Fractional anisotropy (FA)

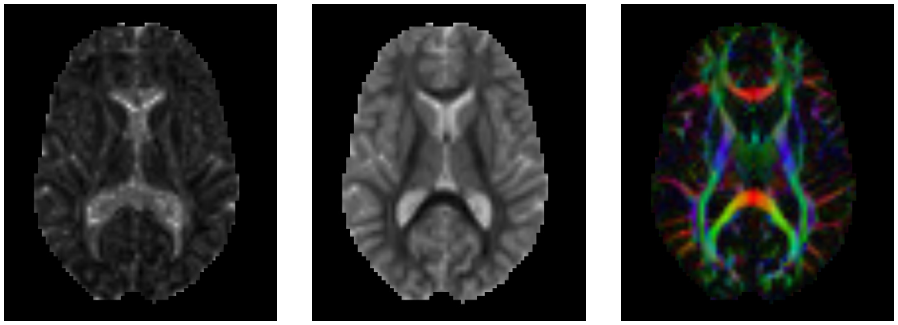

(d) Axial diffusivity (AD) (e) Radial diffusivity (RD) (f) Colour FA (DEC-FA)

Figure 2.4: Common metrics used in diffusion tensor imaging (DTI).

2.3.3 High angular resolution diffusion imaging

A serious drawback of the diffusion tensor model is its inability to represent complex intravoxel topologies, such as crossing fibres (cf. Fig. 2.7 below). The fraction of WM voxels containing crossing fibres has been estimated to be at least 30% [55, 56], and hence calls for more advanced models. QSI does not suffer from this drawback, but the required scan time is too long for clinical use. Therefore, a class of methods has been introduced that aim at maximizing angular resolution, sacrificing the radial component of the diffusion PDF. These methods are nowadays referred to as high angular resolution diffusion imaging (HARDI) techniques. They have in common that the q-space is sampled on a single *shell*, i.e., with gradients of a fixed b-value in equally-distributed directions [57]. The number of directions is as large as the scan time allows, typically around 60, and high b-values are used to maximize angular contrast. In recent years, the radial component of the diffusion PDF has been reintroduced with multi-shell

HARDI acquisition schemes. However, the conceptual switch from cartesian to spherical coordinates in q-space has introduced several important new signal representations, most notably a spherical harmonics decomposition and q-ball imaging.

Spherical harmonics decomposition

Spherical harmonics (SH) of order ℓ and degree m provide a convenient basis for representing complex functions on the unit sphere $\mathbb{S}_2$. They are defined as

$$Y_\ell^m(\theta,\phi) = \sqrt{\frac{2\ell+1}{4\pi}\frac{(\ell-m)!}{(\ell+m)!}}\, P_\ell^m(\cos\theta)\, e^{im\phi} \quad , \tag{2.24}$$

where $P_\ell^m(x)$ is the associated Legendre polynomial of order ℓ and degree $m \in [-\ell,\ell]$. The normalization is chosen such that the inner product

$$\left\langle Y_\ell^m(\theta,\phi), Y_{\ell'}^{m'}(\theta,\phi)\right\rangle = \delta_{\ell,\ell'}\,\delta_{m,m'} \quad , \tag{2.25}$$

with $\delta_{i,j}$ the Kronecker delta [58]. Any complex function of the unit sphere can be decomposed as a linear combination of these basis functions, akin to a Fourier series expansion of a periodic function in sines and cosines of increasing frequency. Here, spherical harmonics of higher orders ℓ correspond to higher "frequency" components of the spherical function.

By its very nature, the HARDI signal is assumed real and antipodally symmetric. Therefore, for applications in DWI, the SH basis is often restricted to real, symmetric functions too [58–61]. Antipodal symmetry is enforced by selecting SH basis functions of even order only. Real functions are selected using the modified basis

$$Y_j(\theta,\phi) = \begin{cases} \sqrt{2}\,\mathrm{Re}(Y_\ell^m) & \text{if } -\ell < m < 0 \\ Y_\ell^0 & \text{if } m = 0 \\ \sqrt{2}\,\mathrm{Im}(Y_\ell^m) & \text{if } 0 < m < \ell \end{cases} \quad , \tag{2.26}$$

where $j = (\ell+1)(\ell+2)/2 - \ell + m$ for $\ell = 0,2,4,\ldots$ and $m = -\ell,\ldots,\ell$ [58]. These basis functions $Y_j(\theta,\phi)$ are depicted in Fig. 2.5. The measured HARDI signal $S(\mathbf{q})$ is then represented as a linear combination of these basis functions

$$S(\theta,\phi) \approx \sum_{j=1}^{n} s_j\, Y_j(\theta,\phi), \tag{2.27}$$

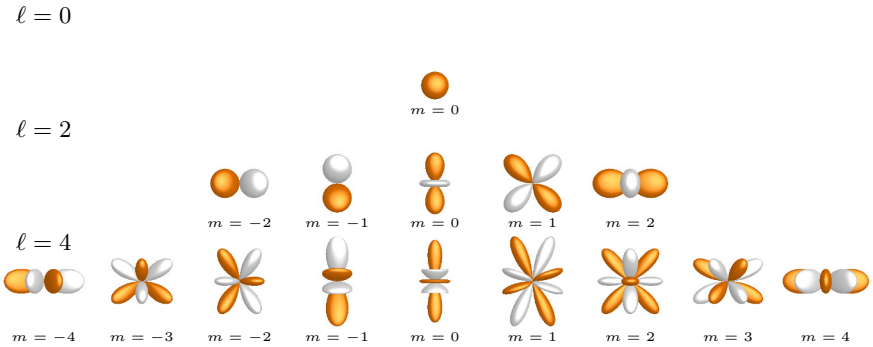

Figure 2.5: The modified spherical harmonics basis functions (2.26) for order ℓ (rows) and degree m (columns). White lobes denote negative amplitude.

where $n = (\ell_{\max}+1)(\ell_{\max}+2)/2$ and $\ell_{\max}$ is the maximal harmonic order. The coefficients s_j form a compact representation of the signal function as a vector of length n. They are estimated from a linear least squares fit of the measured signal. By limiting the SH basis order $\ell_{\max}$, typically around 8, high frequency noise is suppressed.

The SH basis thus provides a natural, model-free representation of the HARDI signal. Many advanced operations in spherical coordinates, including rotation and convolution, become direct, linear operations when cast into the SH basis. Therefore, spherical harmonics have become a mathematical framework of utmost importance for HARDI techniques, including the developments in this thesis.

Q-ball imaging

As explained in Sec. 2.2.2, reconstructing the full diffusion PDF requires many samples in q-space, resulting in long acquisition times. Q-ball imaging (QBI) was introduced as a fast alternative to reconstruct the directional information only, namely the diffusion orientation distribution function (dODF) [62]. The dODF is defined as the radial integral of the diffusion PDF:

$$\mathrm{dODF}(\mathbf{u}) = \int_0^\infty P(\mathbf{r}_0 + \hat{r}\,\mathbf{u} \,|\, \mathbf{r}_0, \tau)\, \hat{r}^2 \,\mathrm{d}\hat{r}, \tag{2.28}$$

where $\mathbf{u} \in \mathbb{S}_2$ is a unit vector that encodes for the position (θ, ϕ) on the sphere. The factor $\hat{r}^2$ is the Jacobian of the spherical coordinate transformation that accounts for the solid angle consideration [63, 64].

QBI estimates the dODF directly from single-shell HARDI data. Tuch [62] has shown that the dODF is closely approximated by the Funk-Radon transform (FRT) of $S(\mathbf{q})$, i.e.,

$$\mathrm{dODF}(\mathbf{u}) \approx \mathrm{FRT}\{S(\mathbf{q})\}(\mathbf{u}) = \int_{\mathbb{S}^2} \delta(\mathbf{q}^T\mathbf{u})\, S(\mathbf{q})\, \mathrm{d}\mathbf{q} \quad , \tag{2.29}$$

where $\delta(\,.\,)$ denotes the Dirac-delta function. For any point $\mathbf{u}$ on the unit sphere $\mathbb{S}^2$, the FRT is defined as the integral over the corresponding equator, i.e., the set of points perpendicular to $\mathbf{u}$. The approximation was shown to improve for higher b-values [62]. However, recent work has pointed out that the above expression is incomplete, because Tuch [62] ignored the solid angle consideration and the $\hat{r}^2$ term in (2.28) [63–65]. This effectively results in a smoothed estimate of the true dODF. A corrected expression is

$$\mathrm{dODF}(\mathbf{u}) = \frac{1}{4\pi} + \frac{1}{16\pi^2}\mathrm{FRT}\{\Delta_b \ln(\ln S_0 - \ln S(\mathbf{q}))\} \quad , \tag{2.30}$$

where Δ_b is the Laplace-Beltrami operator taking the 2nd derivative in spherical coordinates regardless of the radial component [64]. Both the Funk-Radon transform and the Laplace-Beltrami operator correspond with linear operations in the SH basis, facilitating fast computation of the dODF without the need for interpolation [58, 61].

2.4 Microstructure and tissue modelling

From the early days of diffusion MRI, its use as a probe of neural tissue microstructure was quickly recognized. Thomsen *et al.* [66] observed large regional variations of the ADC in human white matter in vivo, and attributed these differences to anisotropic diffusion in the underlying tissue structure, possibly related to the orientation of myelinated axons. Moseley *et al.* [67] subsequently studied diffusion anisotropy in cat brain, and demonstrated that the ADC was indeed anisotropic in WM and isotropic in GM. Similar observations were made in human spinal cord [68]. The idea of exploiting this anisotropy to reconstruct the neural fibre orientation was launched soon after [69] – a new field of study was born.

Indeed, these early developments gave rise to a myriad of models that relate tissue microstructure to the DWI signal directly. In spite of the proven sensitivity of DWI to tissue microstructure, its exact biophysical origins have not been fully elucidated to this day [15, 70]. Microstructure modelling therefore remains a much debated topic of active research. In this section, we aim to provide a high-level overview of the most popular models, with particular focus on the data-driven approaches employed in this thesis.

2.4.1 Compartment models

By modelling the diffusion characteristics of white matter microstructure directly, compartment models aim to provide specific indices such as axon diameter and neurite dispersion that may help in understanding pathology. Generally, these models decompose the DWI signal in 2 or 3 compartments, related to restricted intra-axonal diffusion, hindered extracellular diffusion, and isotropically restricted diffusion of "trapped" water in glial cells or membranes [71–73]. Each of these are modeled with certain parameters Φ and combined linearly with fractions f_k:

$$\frac{S(b,\mathbf{g})}{S_0} = f_i\, M_i(b,\mathbf{g},\Phi_i) + f_e\, M_e(b,\mathbf{g},\Phi_e) + f_r\, M_r(b,\mathbf{g},\Phi_r) \quad , \tag{2.31}$$

with $0 \leq f_k \leq 1$ and $\sum_k f_k = 1$. Panagiotaki *et al.* [72] classified the various microstructure models in a *taxonomy* of compartments. The intra-axonal compartment is typically modelled by either a *stick* of direction $\mathbf{n}$, axial diffusivity d and zero radius, a *cylinder* of non-zero radius R, or a collection of parallel cylinders of Γ-distributed radii. The extra-axonal compartment is usually an isotropic *ball* of Gaussian hindered diffusion, an axially-symmetric *zeppelin*, or a fully anisotropic diffusion *tensor*. Finally, the isotropically restricted compartment is modelled as a collection of uniformly oriented sticks or cylinders, a restricted *sphere* of radius R_s, or a *dot* of zero radius representing completely trapped water.

Most, if not all, of the microstructure models combine these elementary compartments. Examples include the two-compartment ball-and-stick model [74], the composite hindered and restricted model of diffusion (CHARMED) and AxCaliber that combines intracellular cylinders and an extracellular zeppelin [75–77], and the minimal model of white matter diffusion (MMWMD) that consists of a cylinder, a zeppelin, and a dot [78, 79]. In addition, studies have pointed at the importance of modelling axonal fibre crossings and dispersion [55, 56, 80]. Compartment models have therefore been extended to incorporate fibre crossings as discrete compartments [55, 76, 81, 82] or dispersion as Watson or Bingham distributions of fibre orientation [83–87].

Despite considerable progress in the past decade, the model selection and the model assumptions remain hard to validate and justify. Moreover, their non-linear dependence on model parameters complicates optimization, hampering the robustness to noise and the applicability under clinical time constraints.

2.4.2 Spherical deconvolution

The spherical convolution model

Spherical deconvolution (SD) [88] assumes that white matter fibres along a single axis have a fixed and equal contribution to the DWI signal, also known as the *fibre response function* or *kernel* $H(\theta)$. In single-shell HARDI data, for which this technique was originally developed, the response function is a function on a sphere, symmetric around an axis of low amplitude (large diffusion) and with high amplitude (low diffusion) in the radial plane. In addition, SD assumes that there is essentially no exchange (i.e., of water molecules) between white matter fibres on the time scale of the DWI acquisition. As such, the contribution of individual fibre populations in the voxel is considered independent, and their response functions are added linearly after reorientation along the fibre direction. Consider for example two discrete fibre populations of weights f_1 and f_2 along directions $\mathbf{n}_1$ and $\mathbf{n}_2$ respectively, as illustrated in Fig. 2.6. The predicted signal then equals

$$S(\theta,\phi) = f_1\, H'_{\mathbf{n}_1}(\theta,\phi) + f_2\, H'_{\mathbf{n}_2}(\theta,\phi) \quad , \tag{2.32}$$

where $H'_{\mathbf{n}}(\theta,\phi)$ denotes the kernel rotated along axis $\mathbf{n}$. In Cartesian coordinates $\mathbf{g} = (\cos\phi\,\sin\theta, \sin\phi\,\sin\theta, \cos\theta) \in \mathbb{S}_2$, the rotation becomes $H'_{\mathbf{n}}(\mathbf{g}) = H(\cos^{-1}(\mathbf{n}\cdot\mathbf{g}))$. In general, one may consider a fibre orientation distribution function (fODF) $F(\theta,\phi)$, such that

$$S(\mathbf{g}) = \int_{\mathbb{S}_2} H(\cos^{-1}(\mathbf{n}\cdot\mathbf{g}))\, F(\mathbf{n})\, \mathrm{d}\mathbf{n} \tag{2.33}$$

$$= (H * F)(\mathbf{g}) \quad , \tag{2.34}$$

where the operator $*$ denotes convolution on the unit sphere.

In light of the previous section, the spherical convolution model can thus be considered a "single-compartment" model with all focus on modelling fibre crossings and dispersion. As such, all observed regional white matter differences are attributed to partial volume effects (PVE), both in spatial and angular domains [88]. The required fibre response function is either modelled explicitly [89, 90] or estimated from the data at hand [88, 91–93].

Deconvolution and constraints

In order to estimate the fibre ODF in each voxel, the HARDI data is deconvolved with the fibre response function. This is a direct, linear operation when all functions are represented in the SH basis [58, 88]. Let $s_{\ell,m}$ and $f_{\ell,m}$ denote the

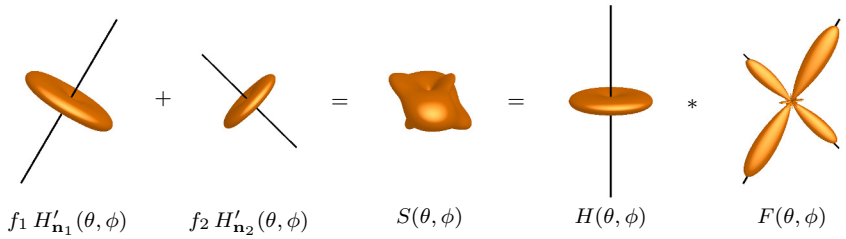

Figure 2.6: The spherical convolution model assumes a fixed and equal *fibre response function* $H(\theta)$ of constant anisotropy. The DWI signal $S(\theta,\phi)$ is a linear combination of this response function rotated along the direction of each individual fibre population in the voxel. For arbitrary fibre geometry, this generalizes to a *spherical convolution* of $H(\theta)$ with a fibre orientation distribution $F(\theta,\phi)$. (Image reproduced from [88])

SH coefficients of order ℓ and degree m of the signal and the fODF respectively. The fibre response function $H(\theta)$ is represented in the same basis with coefficients $h_\ell = h_{\ell,m=0}$ of the zero-degree *zonal* harmonics. Due to the symmetry around the z-axis, all non-zero degree coefficients $h_{\ell,m\neq 0} = 0$. Spherical convolution of H and F then corresponds to a multiplication of their SH coefficients of corresponding order:

$$s_{\ell,m} = \sqrt{\frac{4\pi}{2\ell+1}}\, h_\ell \cdot f_{\ell,m} \quad . \tag{2.35}$$

As such, the fODF could be computed directly from the signal SH coefficients as a simple division, or more commonly as a matrix inversion that incorporates a least-squares fit of the signal coefficients $s_{\ell,m}$ to the HARDI data samples.

However, deconvolution is a highly ill-conditioned operation that basically amplifies any noise in the data. This typically leads to spurious side-lobes, both positive and negative, that are not physically plausible. Initial approaches mediated this problem to some extent by including a low-pass filter in the estimation [88], but the real breakthrough came with the introduction of nonnegativity constrained spherical deconvolution (CSD) [91]. CSD incorporates a nonnegativity constraint on the fODF amplitude, hence prohibiting negative side-lobes. This results in a constrained quadratic programming (QP) problem:

$$\mathbf{f}^\star = \arg\min_{\mathbf{f}} \| \mathbf{S}(\mathbf{g}) - \mathbf{Q}\,\mathbf{H}\,\mathbf{f} \|_F^2 \tag{2.36}$$

$$\text{s.t.} \quad \mathbf{A}\,\mathbf{f} \geq 0 \quad ,$$

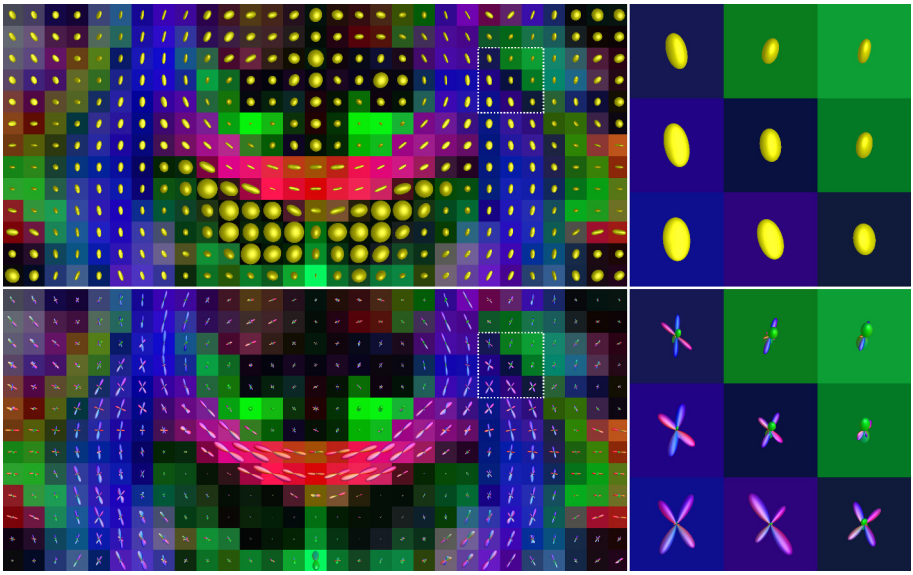

Figure 2.7: *Top:* Rendering of the diffusion tensor (DTI) ellipsoids in a coronal slice of the brain, overlaid onto the DEC-FA map. The highlighted region in the semioval centre is known to contain crossing fibres, but these are not adequately represented by the DTI model. *Bottom:* Corresponding fibre orientation distribution functions (fODF) with constrained spherical deconvolution (CSD). The fODF can represent multiple fibre directions within every single voxel, enabling representation of crossing fibres in the semioval centre.

where $\mathbf{f}$ is the SH coefficient vector of the fODF, $\mathbf{S}(\mathbf{g})$ is a vector of DWI signal measurements at gradient directions $\mathbf{g}$, $\mathbf{Q}$ and $\mathbf{A}$ are matrices that evaluate the SH basis along the gradient directions $\mathbf{g}$ and across a dense set of directions respectively, and $\mathbf{H}$ is a diagonal matrix implementing the convolution operation (2.35). The resulting fODF and its ability to represent crossing fibres is illustrated in Fig. 2.7.

Subsequent research has investigated the benefits of various regularization schemes, priors, and non-Gaussian noise models. One class of methods incorporates spatial regularization to improve robustness to noise in low angular resolution data [94–99]. A fibre continuity prior can furthermore augment the reconstruction to asymmetric fibre ODFs [100]. Other methods have imposed fODF sparsity [101–105], often in a context of compressed sensing [106–108].

Response function estimation

The fibre response function is typically estimated from the data in a mask of high-anisotropy voxels of coherent single-fibre structure. To this end, Tournier *et al.* [91] selected the 300 voxels of highest FA within a white matter mask, and reoriented the data in each of those voxels such that the principal eigenvector of the diffusion tensor is aligned with the z-axis. Zonal spherical harmonics are subsequently fitted to each of those reoriented data samples, and averaged to obtain the fibre response kernel. As such, this procedure is highly data-driven, calibrating the response function to the parameters of the acquisition sequence.

Nevertheless, some authors have highlighted the sensitivity of CSD to inaccurate response function calibration and isotropic partial volume effects [109, 110]. These effects can result in *spurious* (false-positive) peaks of the fODF, reducing specificity and possibly hampering subsequent tractography (see below). One study also found that an alternative deconvolution algorithm based on Richardson-Lucy damping [111, 112] was less affected by perturbations of the response function [109]. Several recursive kernel estimation methods have therefore been introduced [92, 93], which improve the selection and alignment of single-fibre voxels based on extracted fODF peaks from the previous iteration. Alternatively, Schultz and Groeschel [104] estimated optimal response functions in each individual voxel, based on a $L_{0.5}$ sparsity prior.

Apparent fibre density

At high b-values, the fODF amplitude is approximately proportional to the radial DWI signal for the corresponding fibre orientation [113]. Simultaneously, signal from the restricted, intra-axonal compartment is preserved [114, 115], whereas the extra-axonal water signal is strongly attenuated at these high b-values [113]. As such, the fODF amplitude is approximately proportional to the intra-axonal water content, and thus to the fibre density. D. Raffelt *et al.* [113] have therefore introduced the term *apparent fibre density* (AFD) to indicate the fODF peak amplitude as a quantitative measure of the intra-axonal fibre volume, and validated this interpretation in Monte-Carlo simulations. They later refined their definition to the integral of segmented fODF lobes, to improve robustness to fibre dispersion [116]. A similar metric, hindrance modulated orientational anisotropy (HMOA), was proposed independently [117]. These metrics were shown able to characterize white matter changes in pathology [113, 116].

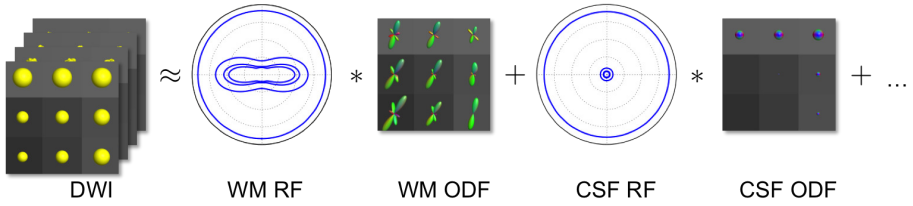

Figure 2.8: Multi-tissue spherical deconvolution of multi-shell DWI data. Given response functions (RF) of white matter (WM), cerebrospinal fluid (CSF) and other tissues, orientation distribution functions (ODF) of those tissues are reconstructed.

2.4.3 Multi-tissue spherical deconvolution

As mentioned previously, spherical deconvolution assumes a single fibre response function, and attributes all regional signal variations to partial voluming of WM in different orientations. However, it ignores *spatial* partial voluming with adjacent tissues such as GM and CSF, which are not adequately modelled with a WM fibre response function. Such non-WM PVE was shown to affect the fODF reconstruction in 35–50% of all WM voxels [110]. Jeurissen *et al.* [118] therefore extended CSD to multiple tissue classes, reconstructing *tissue* ODFs for WM, GM, and CSF. In order to recover these tissue ODFs, multi-shell HARDI data is required with at least as many b-values as the number of tissues. The spherical convolution model (2.34) then generalizes to a sum of N tissues

$$S_b(\mathbf{g}) = \sum_{t=1}^{N} (H_{t,b} * F_t)(\mathbf{g}) \quad , \tag{2.37}$$

with b-value dependent tissue response functions $H_{t,b}(\theta)$ and tissue ODFs $F_t(\theta, \phi)$. Akin to CSD, these tissue ODFs are the solution to a constrained QP problem [118]. Results show that including GM and CSF response functions can substantially improve the precision of the fibre ODF reconstruction and reduce spurious peaks, leading to more reliable AFD measurements [118].

2.5 Tractography

2.5.1 Streamline tractography

Fibre tractography aims at delineating long-range neuronal pathways, integrating local estimates of the axonal fibre direction on the global, full-brain scale. Initial attempts took a streamline approach along the estimated WM orientation, typically provided by the principal eigenvector $\mathbf{e}_1$ of the diffusion tensor [20, 119–123]. Hence, the fibre track $\mathbf{r} : \mathbb{R} \to \mathbb{R}^3 : s \mapsto \mathbf{r}(s)$ is the solution to a first order differential equation

$$\frac{\mathrm{d}\mathbf{r}(s)}{\mathrm{d}s} = \mathbf{e}_1(\mathbf{r}(s)) \quad , \tag{2.38}$$

subject to initial condition $\mathbf{r}(0) = \mathbf{r}_0$ which specifies a seed point for the track [122]. In practice, a first-order Euler integration strategy would be initialized at the seed point and "walk" along the estimated fibre direction with a fixed step size, or a more general Runge-Kutta strategy would account for higher-order derivatives. Seeds are randomly selected in a white matter or brain mask. In addition, stop criteria such as an FA lower-bound and a maximum curvature are required.

Beyond DTI, diffusion and fibre ODFs can have multiple maxima that represent crossing fibre populations. In that case, streamline tracking methods may then select the ODF peak closest to the current tracking direction [55, 90, 124].

2.5.2 Probabilistic tractography

An important drawback of the deterministic streamline approach is its sensitivity to noise on the data. Local perturbations of the estimated fibre direction may accumulate throughout the stepping procedure, resulting in false positive long-range connections. Moreover, a single estimation error can interrupt tracks due to the curvature threshold, resulting in false negative connections. In order to overcome some of these limitations, probabilistic tractography methods relax the strict constraints of streamline tracking by drawing random samples from a probability distribution.

Arguably the most widely used in practice is probabilistic streamline tracking, a class of methods which operate similar to the procedure outlined above but include uncertainty estimates of the local fibre direction [74, 90, 124–134]. These methods improve the sensitivity of deterministic streamline tractography, i.e., they are less prone to false-negative connections. Nevertheless, their specificity towards false positives remains low.

Alternative approaches have addressed fibre tracking at a larger spatial scale, by delineating shortest-path connections between target regions [135–139]. These approaches evaluate the support for each particular track along its entire length, which intends to increase robustness to local perturbations of the data.

2.5.3 Global tractography

In parallel with the development of streamline and probabilistic tractography, a class of methods was developed that adopt a global inverse problem perspective [24, 140–145]. These methods aim to reconstruct the geometry of the complete white matter that best explains the measured DWI data. As such, the resulting tractogram bears a quantitative correspondence to the AFD in the data. Moreover, they address the ill-posed nature of diffusion tractography at the same time, i.e., they are more robust to noise and local reconstruction errors than streamline tracking [146].

In general, global tractography defines an external energy term related to the data likelihood, and an internal energy term related to priors of the expected track configuration. Such priors may, for example, penalize high-curvature tracks.

2.5.4 Track filtering and anatomical priors

In recent years, tractography has gained increasing interest for studying the structural connections between grey matter regions in the brain, the so called *human connectome* [5]. Given a grey matter parcellation, evaluating a connectivity matrix using graph theoretic measures of connectivity facilitates network analysis of the white matter architecture at the global level [147–153]. However, the number of streamlines connecting two regions is not a valid marker of connectivity [154]. With the exception of global tractography, the distribution of generated fibre tracks is fundamentally decoupled from the DWI data and therefore bears no relation with the axonal fibre distribution.

Therefore, a number of track filtering methods have been introduced, which assign a weight to each streamline such that the full brain track distribution matches the apparent fibre density in the DWI data [155–160]. As such, a full brain probabilistic tractogram is subsampled until its regional connectivity characterizes the strength of the diffusion measurement between regions, making it a viable tool for structural connectomics [161].

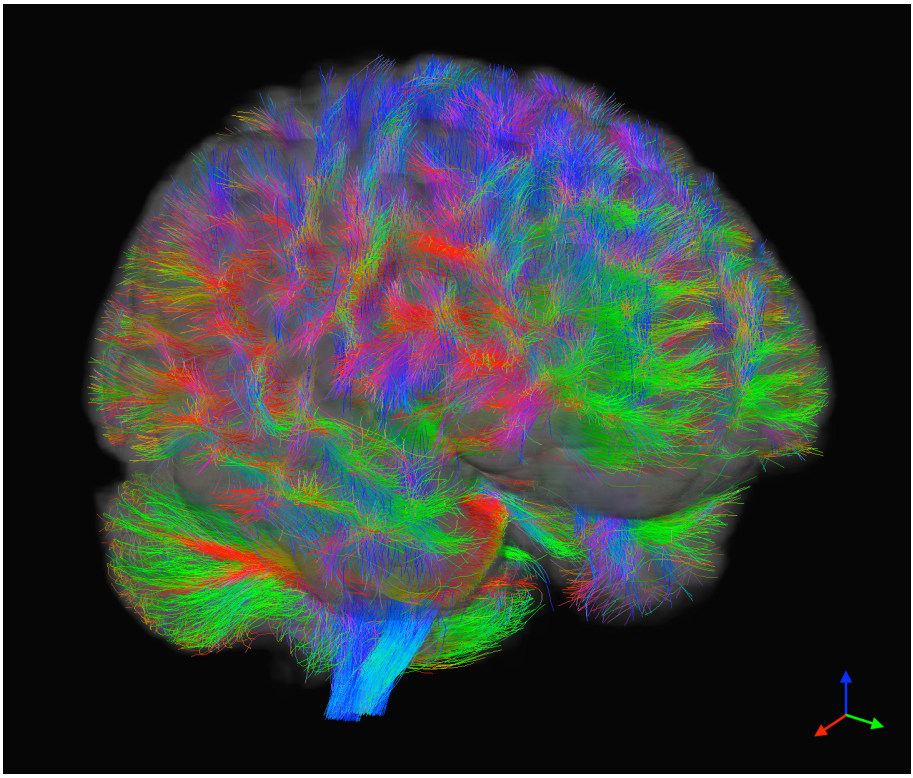

Figure 2.9: Full brain global tractography in the human brain. Tracks are coloured by their local direction: red indicates left-right, green indicates posterior-anterior and blue indicates inferior-superior.

In addition, some methods have incorporated anatomical priors that impose that track endpoints are located in grey matter [144, 162] in an effort to improve specificity of the resulting connections.

2.5.5 Bundle segmentation and clustering

Clinical applications such as neurosurgical planning often demand targeted tracking of particular WM fibre bundles, for example the corticospinal tract and the arcuate fasciculus. Generally, this requires manual delineation of inclusion, exclusion, and seeding regions-of-interest (ROI), which is tedious and subjective work. Therefore, a number of automated bundle segmentation methods have been presented, either based on a predefined parcellation, on unsupervised

clustering techniques, or on a combination of both [163]. Parcellation-based methods [164, 165] use an atlas of predefined ROIs to segment fibre bundles across subjects, similar to the manual process used for defining white matter atlases such as Catani and Thiebaut de Schotten [166]. Track clustering methods [167–171], on the other hand, aim to group tracks into bundles of consistent geometry, without reference to cortical regions. The resulting clusters are subsequently or simultaneously labelled as known anatomical structures based on atlas information [167, 172–177].

2.6 Validation of microstructure and tractography

DWI being unique in its ability to probe neural tissue structure in vivo, a reliable ground truth is unfortunately out of reach. This absence of a gold standard is a major impediment to the validation and comparison of microstructure models and tractography methods. Nevertheless, a number of *indirect* validation strategies can be used, in phantoms, ex vivo and in vivo.

First of all, numerical phantoms are by far the most commonly used for validation of DWI techniques. They consist of simulated data with known ground truth, and offer full control over the parameters. The phantom is either simulated as a combination of basis functions with added noise (e.g. [118, 178, 179]), or using Monte Carlo simulations of water diffusion for a given microstructure geometry (e.g. [78, 180–183]). For microstructure imaging, such phantoms serve primarily to assess the accuracy of the model optimization, as the simulation itself depends on assumptions about the tissue structure and signal. For tractography, simulated phantoms with dedicated fibre bundle configurations allow to measure sensitivity and specificity of fiber tracking techniques [179, 184–186]. Alternatively, physical phantoms based on fibres or capillaries [180, 187–189] are used for evaluating tractography accuracy [190] and for quality assurance of acquisition protocols [191].

Secondly, advanced microscopy techniques can provide detailed information on the tissue microstructure in ex vivo tissue samples [192]. In particular, 3-D polarised light microscopy [193], optical coherence tomography [194] and CLARITY [195–197] are promising techniques. DWI has for instance been compared to microscopy for measuring fibre ODFs [198, 199]. Plausibility of in vivo estimates of microstructure parameters obtained with DWI can be compared to histological measurements, such as for instance cell density [200] or diameter [201]. The main drawback of microscopy is that it can typically only be applied to small tissue samples.

Finally, in the absence of ground truth, assessment of tractography results is often necessarily limited to visual appreciation based on high-level expert knowledge. In this perspective, comparison between methods is facilitated by the use of publicly available DWI data that is specifically acquired for research purposes using dedicated high-resolution imaging protocols, such as the Human Connectome Project (HCP) database [202]. Validation of tractography in real tissue can also be based on injectable tracer studies of long-range connectivity between brain regions in animals [203–207]. While such tracer studies provide highly accurate projections of cortical connectivity, a drawback is that only a single injection per animal can be used [208].

2.7 Conclusion

In this chapter, we introduced the underpinning principles of diffusion-weighted imaging and provided an overview of the current state-of-the-art analysis methodology and validation strategies. We focused in particular on signal and microstructure modelling and on tractography, the research areas to which we will contribute in this thesis. In the next chapters, we will further elaborate these techniques and present our method contributions, experiments and results.

Chapter 3

Multi-shell multi-tissue global tractography

The work in this chapter was published in D. Christiaens *et al.*, "Global tractography of multi-shell diffusion-weighted imaging data using a multi-tissue model", *NeuroImage*, vol. 123, pp. 89–101, Dec. 2015.

3.1 Introduction

Diffusion-weighted imaging (DWI) [12] and tractography [20] provide a unique, non-invasive technique to study the macroscopic structure and connectivity of the white matter in the human brain in vivo (the human *connectome*) [21, 209]. Not only is mapping the connectome one of the biggest challenges in modern neuroscience, a detailed understanding of its structure and organization may also help the neuroscientific community to gain insight in a number of important disease processes [5, 210]. Therefore, diffusion-weighted imaging and tractography are key elements in recent, large-scale efforts for mapping the human brain [202, 211]. Yet, besides large datasets, improved analysis pipelines are needed before connectomics may reliably answer those questions, first and foremost improved microstructural modelling and tractography [210].

While it has been recognized early on that diffusion is sensitive to the underlying fibre geometry [15], understanding the precise link between both is essential for accurate and robust interpretation of the measured data [146, 210]. Hence, considerable effort has gone to modelling this so-called *local inverse problem*,

beyond the (Gaussian) diffusion tensor model [33]. On the one hand, a growing class of methods aims at modelling the biophysical process directly, hence deriving microstructural properties such as axon diameter, neurite density, etc. [72]. On the other hand, data-driven approaches have been developed, which aim at deriving the fibre geometry with as few prior assumptions about its physical properties as possible. Arguably the most popular among these are spherical deconvolution (SD) techniques [90, 91], which reconstruct the fibre orientation distribution function (fODF) based on a fibre response function that may be estimated from the data itself. However, despite the progress in this area, the local inverse problem is inherently incomplete, as the symmetric nature of the diffusion profile cannot discriminate crossing and fanning fibre geometries on a larger scale [210].

Because of the aforementioned limitations of local modelling, Mangin *et al.* [146] recently advocated "a shift toward a *global inverse problem* perspective, namely the global reconstruction of the geometry of the complete white matter". Indeed, accounting for the spatial continuity of neural fibres may help in recovering locally ambiguous configurations, and improve the robustness of the model fitting. Such is the motivation behind a growing class of spatially regularized fODF reconstruction methods [94, 95, 97]. Global tractography (GT) methods [123, 140–143, 145] go even further and aim at reconstructing the entire fibre configuration that best explains the measured diffusion data. Moreover, they address the ill-posed nature of diffusion tractography at the same time, i.e., they are more robust to noise and local reconstruction errors than streamline tracking [146].

Yet, current GT methods rely on specific microstructural models with fixed parameters, which may not always be adapted to the type of data available. Kreher *et al.* [141] and Fillard *et al.* [142] model the fibre response as an axially-symmetric diffusion tensor. Reisert *et al.* [143] use the stick model for the intra-axonal compartment [74], which they have recently extended with a separate extra-axonal compartment, modelled by a diffusion tensor [145]. Besides having to be tuned to the data at hand, these models are typically defined for white matter and therefore fail to take partial volume effects from adjacent tissues into account.

In this chapter, we introduce a multi-shell spherical harmonic response function, measured from the data, into the generative model defined as part of the global tractography method of Reisert *et al.* [143]. In addition, we adopt the multi-tissue model of Jeurissen *et al.* [118] to differentiate between white matter (WM), grey matter (GM) and cerebrospinal fluid (CSF) compartments. As such, our approach explicitly accounts for partial volume effects, and does not require a white matter mask in the reconstruction.

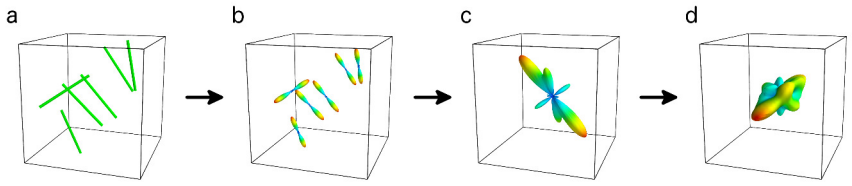

Figure 3.1: Generative model: (a) consider all particles positioned within a voxel; (b) each of them is represented as a Dirac delta function in the spherical harmonics basis; (c) the sum of these functions is the segment orientation distribution function (ODF); (d) the convolution of this ODF with the fibre response function is the simulated signal D'_{WM}.

3.2 Methods

3.2.1 Global tractography in the spherical harmonics basis

Particle-based global tractography methods typically model the neural fibre trajectories as chains of particles (line segments), each characterized by their position $\mathbf{x}_i$ and orientation $\mathbf{n}_i$ [141–143]. The fibre model $\mathcal{M}$ then consists of the set of all segments $\{X_i = (\mathbf{x}_i, \mathbf{n}_i)\}$ and a set of connections between their endpoints. Ultimately, we wish to maximize the posterior probability of $\mathcal{M}$ given the data D, which, according to Bayes' rule and assuming a Gibbs distribution at temperature T, can be written as

$$P(\mathcal{M}|D) \propto P(D|\mathcal{M})\, P(\mathcal{M}) \tag{3.1}$$

$$= e^{-E_{\mathrm{data}}(\mathcal{M},D)/T}\, e^{-E_{\mathrm{con}}(\mathcal{M})/T}\,. \tag{3.2}$$

As such, the problem becomes finding the global minimum of $E(\mathcal{M}) = E_{\mathrm{data}}(\mathcal{M}, D) + E_{\mathrm{con}}(\mathcal{M})$. The data energy E_{data} relates to the data likelihood and is defined as the mean squared error between the measured data D and the predicted data D', simulated from the particle configuration $\mathcal{M}$ using a generative model. The connection energy E_{con} relates to the model prior and promotes connectivity and smoothness of the reconstructed tracks.

Generative model

The central hypothesis in this work is that, for white matter, each segment has a fixed and equal contribution to the *predicted* data D'_{WM}, in the form of a fibre response kernel $K_b(\theta)$. K_b is a spherical function depending only on the

elevation angle θ and the b-value, that models the expected diffusion signal for a single fibre direction along the z-axis. As such, we can simulate the white matter signal for gradient direction $(\mathbf{g}, b)$ by orienting the z-axis of this kernel along all segments, and integrating over all segments in a voxel $\mathbf{r}$, i.e.,

$$D'_{\mathrm{WM}}(\mathbf{r}, \mathbf{g}, b) = \sum_{\substack{(\mathbf{x}_i, \mathbf{n}_i) \\ \mathbf{x}_i \in \mathcal{N}(\mathbf{r})}} w(\|\mathbf{r} - \mathbf{x}_i\|)\, K_b(\arccos(\mathbf{n}_i \cdot \mathbf{g})) \quad . \tag{3.3}$$

In this equation, $\mathcal{N}(\mathbf{r})$ denotes the voxel neighbourhood and $w(\cdot)$ is some spatial weighting function. In the most simple case, w is a block function the size of one voxel. Cast into the basis of real, symmetric spherical harmonics (SH) [90], the kernel reorientation can be described as a convolution with a SH Dirac delta function $\delta_{\mathbf{n}_i}$ along the segment direction $\mathbf{n}_i$. As such, the predicted white matter signal becomes

$$D'_{\mathrm{WM}}(\mathbf{r}, \mathbf{g}, b) = \sum_{\substack{(\mathbf{x}_i, \mathbf{n}_i) \\ \mathbf{x}_i \in \mathcal{N}(\mathbf{r})}} w(\|\mathbf{r} - \mathbf{x}_i\|)\, (K_b * \delta_{\mathbf{n}_i})(\mathbf{g}) \tag{3.4}$$

$$= K_b * \sum_{\substack{(\mathbf{x}_i, \mathbf{n}_i) \\ \mathbf{x}_i \in \mathcal{N}(\mathbf{r})}} w(\|\mathbf{r} - \mathbf{x}_i\|)\, \delta_{\mathbf{n}_i}(\mathbf{g}) \tag{3.5}$$

$$= K_b * \Psi(\mathbf{r}, \mathbf{g}) \quad , \tag{3.6}$$

where $*$ is the spherical convolution operator and $\Psi(\mathbf{r}, \mathbf{u})$ is an SH orientation distribution function (ODF) of the segments in voxel $\mathbf{r}$. Hence, the white matter signal is simulated by converting the segment configuration to a fibre ODF and calculating the convolution with a kernel K_b, as depicted in Fig. 3.1.

In addition, similar to Jeurissen *et al.* [118], we introduce one or more isotropic kernels $c_j(b)$ that account for partial volume contamination of other tissue types. Typically, we will use these to model cerebrospinal fluid (CSF) and grey matter (GM), but it should be noted that these can be used to model any isotropic signal component. Hence our complete model becomes

$$D'(\mathbf{r}, \mathbf{g}, b) = K_b * \Psi(\mathbf{r}, \mathbf{g}) + \sum_j c_j(b)\, f_j(\mathbf{r}) \quad , \tag{3.7}$$

where $f_j(\mathbf{r})$ is the fraction of isotropic component j in voxel $\mathbf{r}$.

Data likelihood and priors

Assuming a Gaussian data likelihood, the data energy is defined as

$$E_{\text{data}}(\mathcal{M}, D) = \kappa \left(\frac{\|D - D'\|^2}{Q\, K_0^2} + \mu\, N_p \right) \quad , \tag{3.8}$$

in which κ is a weighting factor. In the first term, Q is the number of acquired DWI volumes and K_0 is the amplitude of the $b = 0$ WM response function. Hence, this term expresses the mean-squared-error of the data relative to the kernel. Because K_0 is proportional to the intensity of the DWI data, this scaling assures that the reconstruction can handle different acquisition protocols and gradient schemes without needing to adapt the parameters. The second term imposes a L_1-prior on the total number of particles N_p in the model, each of which has an associated cost μ (the *particle potential*). As such, we aim to reconstruct the data as well as possible, with as few particles as needed.

The connection energy is defined as in Reisert *et al.* [143],

$$E_{\text{con}}(\mathcal{M}) = \lambda \left(\sum_{X_i - X_j \in \mathcal{M}} U_{\text{bend}}(X_i - X_j) - \nu\, N_c \right) \quad . \tag{3.9}$$

The first term comprises the total bending energy across all connected segment pairs X_i–X_j, expressed as the distance of the connected endpoints to the midpoint between both segments. The second term introduces a connection potential ν for each connection, with N_c the total number of connections, meant to encourage particles to connect to their neighbouring segments.

The weighting factors κ and λ of the data and connection energy terms determine the balance between both. Generally, a good balance depends on the required number of particles, which is controlled by the segment weight w as defined in (3.3). Additionally, we gradually decrease the weight of the data energy in favour of connection energy throughout the optimization, controlled by the temperature T (see below). In practice, $\kappa = \frac{T}{T_1} \frac{1}{w^2}$ and $\lambda = 1$ is a good default setting for different datasets. The remaining two parameters, the particle and connection potentials, can be adapted by the user to give more or less weight to the priors.

Optimization

The optimization of (3.1) is achieved with a Reversible jump Markov chain Monte Carlo (RJMCMC) algorithm [212], which allows to obtain random samples from the posterior distribution $P(\mathcal{M}|D)$. As in simulated annealing

methods, the temperature T is gradually reduced to increase the likelihood of sampling from the maximum of $P(\mathcal{M}|D)$ (or the minimum of $E(\mathcal{M})$). At each iteration, the algorithm proposes a new state $\mathcal{M}'$, obtained as a random perturbation of the current state $\mathcal{M}$, and evaluates the Green's ratio

$$R = \min\left(1, \frac{e^{-E(\mathcal{M}')/T}}{e^{-E(\mathcal{M})/T}} \frac{p^{\text{prop}}(\mathcal{M}|\mathcal{M}')}{p^{\text{prop}}(\mathcal{M}'|\mathcal{M})}\right) \quad , \tag{3.10}$$

where $p^{\text{prop}}(\text{next}|\text{current})$ is the transition probability from current state to the next state. The proposed state $\mathcal{M}'$ is then accepted with probability R, or discarded otherwise. Transition proposals include creating or removing a particle, changing its position and orientation by either a random perturbation or optimally w.r.t. its connected neighbours, and (dis)connecting a particle's endpoint to the endpoint of another particle in its neighbourhood [141, 143].

Upon every change to the particles in voxel $\mathbf{r}$, the isotropic fractions $f_j(\mathbf{r})$ are updated by evaluating the difference between the measured data D and the predicted WM signal D'_{WM}. By definition (3.7), this difference equals the other tissue compartments, as well as the residual WM, not yet recovered by the optimization. To account for the latter, we introduce an additional isotropic fraction of residual WM f_{resWM} with corresponding kernel $c_{\text{WM}}(b)$, defined as the isotropic part of the white matter kernel $K_b(\theta)$. All isotropic fractions, including the residual WM, are then estimated as a non-negativity constrained, linear least-squares fit to

$$D - D'_{\text{WM}} = \sum_j c_j(b)\, f_j + c_{\text{WM}}(b)\, f_{\text{resWM}} \quad . \tag{3.11}$$

Finally, the data energy is updated by evaluating (3.7)–(3.8).

The presented method was implemented as an add-on to MRtrix (J-D Tournier, Brain Research Institute, Melbourne, Australia, `www.mrtrix.org`) and released to the community.

3.2.2 Response function estimation

So far, we have made no prior assumptions on the acquisition protocol. The presented method can be applied to data of any q-space sampling scheme, as long as $K_b(\theta)$ can be defined. For the remainder of this chapter, we choose to estimate the fibre response function from the data, which requires a multi-shell protocol. The main advantage of this approach is that K_b is easily calibrated to the scanner, the acquisition sequence, and the (group of) subject(s). The white matter response function is estimated as the average signal in a mask of single

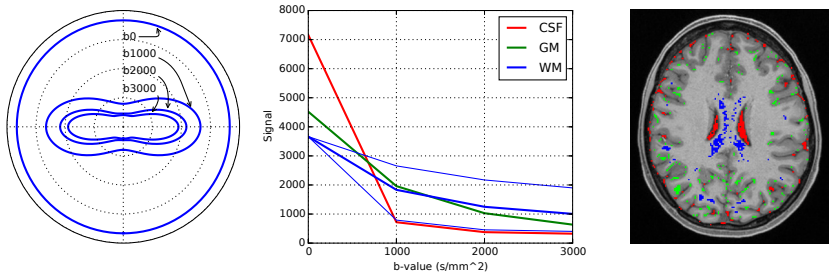

Figure 3.2: Estimated kernels for dataset 1. Left: the fibre response kernel for a fibre along the vertical axis, at different b-values. Middle: the radial attenuation of the CSF and GM kernels, as well as the isotropic part of the WM kernel (thick blue line) and its radial (top thin line) and axial attenuation (bottom thin line). Right: Corresponding masks in which these kernels are estimated.

fibre voxels, after reorienting the gradient tables in these voxels such that the principal eigenvectors of the diffusion tensors align [91]. CSF and GM kernels are estimated as the mean DWI signal per shell, averaged across respective masks.

A single fibre WM mask and isotropic GM and CSF masks can be obtained from a T1w-image and the fractional anisotropy (FA) map, provided that the T1w and DWI data have been co-registered to the same space (see Data below). First, a probabilistic tissue segmentation is generated from a T1w-image using FSL FAST [213] and thresholded at probability $> 95\%$ for WM, GM and CSF separately. Secondly, single fibre voxels are selected from the WM segmentation by thresholding the FA above 0.75. Similarly, isotropic GM and CSF voxels are selected by imposing an FA below 0.1. An example of the resulting masks and kernels are shown in Fig. 3.2.

3.3 Data and Experiments

3.3.1 Data

Simulated phantom

Phantom data with known ground truth was generated using the Phantomas software [179], based on the geometry of the 2nd HARDI reconstruction challenge, organized at ISBI 2013 [186]. This phantom consists of white matter,

grey matter, and CSF mimicking regions, simulated with realistic relaxation times. The white matter contains 27 fibre bundles, including crossing, kissing, and fanning structures, simulated with a multi-tensor model with principal eigenvalue 0.0017 and secondary eigenvalues 0.0002, and corrupted with Rician noise at signal-to-noise ratios (SNR) 5, 10, 20, 30, 40, and 50. The voxel size is 2 mm isotropic; the gradient encoding scheme equals that of the Human Connectome Project (cf. in vivo dataset 1). All tissue-specific response functions are estimated in ground-truth regions on the noise-free dataset.

In vivo dataset 1

Data of a neurologically healthy subject was provided by the WU-Minn Human Connectome Project (HCP) Q3 data release [202]. The diffusion data consists of 3 × 90 gradient directions at b-values 1000, 2000, and 3000 $\mathrm{s/mm^2}$ and 18 non-diffusion weighted images ($b = 0$), at an isotropic voxel size of 1.25 mm, and was corrected for motion, eddy current, and EPI distortions as described in Glasser *et al.* [214]. In addition, a T1-weighted image of isotropic voxel size 0.7 mm is available in the same reference frame.

In vivo dataset 2

A second, healthy subject was scanned on a Philips Achieva 3.0 T TX system, using a diffusion-weighted imaging sequence comprised of 10 $b = 0$ images, 25 images at b-value 700 $\mathrm{s/mm^2}$, 40 images at $b = 1000\,\mathrm{s/mm^2}$, and 75 images at $b = 2800\,\mathrm{s/mm^2}$. The voxel size equals 2.5 mm (isotropic). Additionally, a single $b = 0$ image was acquired with reverse-phase encoding to correct for EPI distortions, as well as motion and eddy current distortions using FSL TOPUP and EDDY tools [215, 216]. A T1w-scan was acquired with a 3D TFE sequence, at voxel size 1.2 mm × 0.98 mm × 0.98 mm.

3.3.2 Parameter settings

The maximal SH order $\ell_{\max} = 10$ was used in all experiments. In the phantom dataset, we use a segment length $2\ell = 4$ mm and a particle weight $w = 0.1$, meaning that on average $w^{-1} = 10$ segments per voxel are needed to reconstruct the white matter. For the in vivo datasets, the segment length 2ℓ is 2 mm. The particle weight is set to $w = 0.1$ for dataset 1 and to $w = 0.0125$ for dataset 2 to account for the larger voxel size. The connection potential ν is fixed at 0.5 for all experiments. The particle potential is set to $\mu = 5\%\, w$.

The optimization starts with a burn-in phase at constant temperature T_0 for the first 10% of the iterations, and then proceeds with an exponential cooling schedule towards the final temperature T_1. For the phantom dataset, we used 10^8 iterations from $T_0 = 0.5$ to $T_1 = 0.001$. For the in vivo data, we used 10^9 iterations, with $T_0 = 0.1$ and $T_1 = 0.001$.

3.3.3 Validation

We compare the proposed multi-shell multi-tissue global tractography (MSMT-GT) method to two alternative (multi-shell) approaches on the simulated phantom:

1. Multi-shell multi-tissue constrained spherical deconvolution (MSMT-CSD) [118], followed by probabilistic streamline tractography using the 2nd order method iFOD2 as implemented in MRtrix [124, 133]. All parameters are set to their default values: the step size is 0.5× voxel size, the maximum angle between consecutive steps is 45°, the fODF amplitude cut-off is 0.1, and the minimum track length is 5× voxel size. Seed points are drawn from a uniform distribution in a full brain mask.

2. The global tractography method of Reisert *et al.* [143], as implemented in MITK [217, 218], which evaluates the ball-and-stick model on the diffusion ODF [57]. We employed the multi-shell diffusion ODF reconstruction method of Aganj *et al.* [64], and set all common parameters such as segment length and temperature equal to those chosen in our own method. Parameters specific to the ball-and-stick model were tuned by MITK with the built-in methods within a WM mask.

Quantitative comparison in the simulated datasets is based on the tractometer approach [185, 219, 220]. Given regions-of-interest (ROIs) at the ends of all bundles in the phantom, we calculate the percentage of valid connections (VC) and invalid connections (IC) between these end regions, and the percentage of no connections (NC), i.e., tracks that reach none or only one of the target ROIs. Ideally, VC is 100 % and IC and NC are 0 %. For ease of interpretation, we also report the total connection ratio VC+IC = 1–NC, which should be large for maximal connectivity, and the valid connection ratio VC/(VC+IC), which should be large for maximal specificity. Finally, we count the number of valid bundles (VB) and invalid bundles (IB), where a bundle is counted as soon as at least one track connects its two end regions. The phantom contains 27 ground truth bundles between 53 end regions, which allows for a maximum of 1351 invalid bundles.

In the in vivo datasets, we provide a visual comparison between these methods in interesting regions and fibre bundles, which allows for a qualitative assessment of the reconstructed tractograms.

3.4 Results

3.4.1 Simulated data

We investigate the effect of the particle potential μ and connection potential ν on the tractometer analysis. First, fixing $\nu = 0.5$, the effect of varying μ is shown on the left in Fig. 3.3. The total connectivity VC+IC is maximum at $\mu = 2\%\, w$ (23.9%), and the valid connection ratio VC/(VC+IC) reaches a maximum of 69.9% for $\mu = 1\%\, w$. The number of valid bundles VB is 27 for most of the range but decreases at $\mu = 10\%\, w$ and beyond. The number of invalid bundles IB shows a clear decreasing trend for increasing particle potential. Secondly, when fixing $\mu = 5\%\, w$ and varying the connection potential ν, the total connection ratio increases for higher ν, while the valid connection ratio decreases. Simultaneously, both VB and IB increase for increasing ν. As such, decreasing the connection potential improves the precision while sacrificing connectivity. It is clear from these graphs that there is no single parameter setting that performs best by all measures. We therefore selected $\nu = 0.5$ and $\mu = 5\%\, w$ as a sensible compromise.

Given these parameters, we compare the presented method to the competing techniques described above across different SNR levels. The resulting metrics are plotted in Fig. 3.4. For SNR 20, we listed the results in Table 3.1 and depicted the reconstructed tracks in Fig. 3.5. The presented MSMT-GT method has the best valid connection ratio of the tested techniques, especially for SNR $\geq$ 10. Streamline tractography consistently outperforms global tractography in terms of the total connection rate. The multi-shell multi-tissue model proves particularly beneficial in the low-SNR range ($\leq$ 20) for both streamline and global tractography, as shown by the higher VC/(VC+IC) and much lower IB. This can also be observed in Fig. 3.5, which shows that MITK-GT results in many spurious tracks in GM regions that are not explicitly accounted for in its ball-and-stick model. Additionally, MITK was never able to reconstruct all 27 fibre bundles in the phantom, while both MSMT approaches did for sufficient SNR.

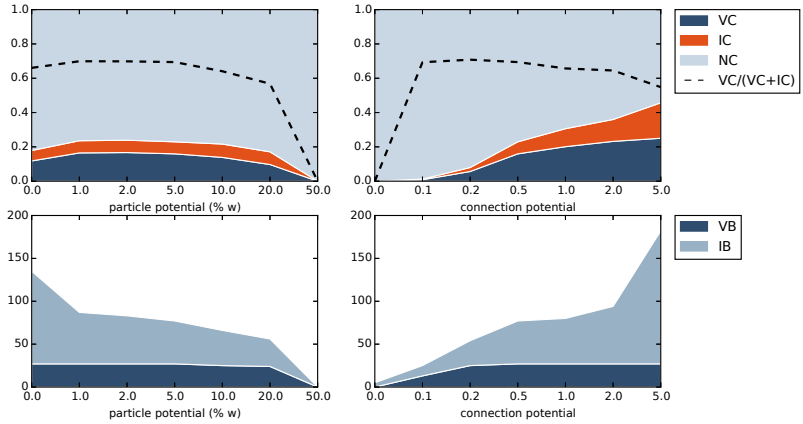

Figure 3.3: Tractometer analysis of the simulated phantom: effect of the particle and connection potentials at SNR 20. In the left plots, the particle potential μ (expressed as a percentage of the particle weight w) is adapted while the connection potential is kept constant at $\nu = 0.5$. In the plots on the right, ν is adapted while μ is fixed at $5\%\, w$.

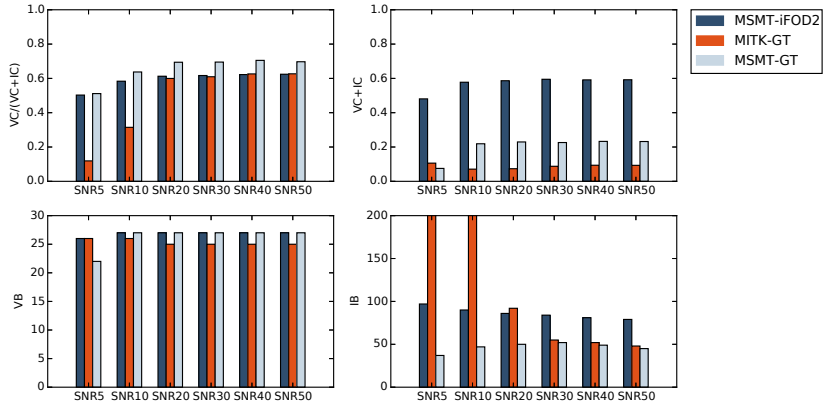

Figure 3.4: Tractometer analysis of the simulated phantom: comparison to streamline tractography and MITK global tractography on for different SNR levels.

Table 3.1: Tractometer results of the simulated phantom at SNR 20. The number of valid connections (VC), invalid connections (IC), and no connections (NC) are expressed as percentages relative to the total number of tracks (#t). The no. valid and invalid bundles (VB and IB) are expressed in absolute terms.

	#t	VC (%)	IC (%)	NC (%)	VC + IC (%)	$\frac{\text{VC}}{\text{VC+IC}}$ (%)	VB	IB
MSMT-iFOD2	10000	35.9	22.7	41.4	**58.6**	61.3	**27**	86
MITK-GT	8511	4.4	3.0	92.6	7.4	59.5	25	92
MSMT-GT	5756	15.9	7.0	77.1	22.9	**69.4**	**27**	**50**

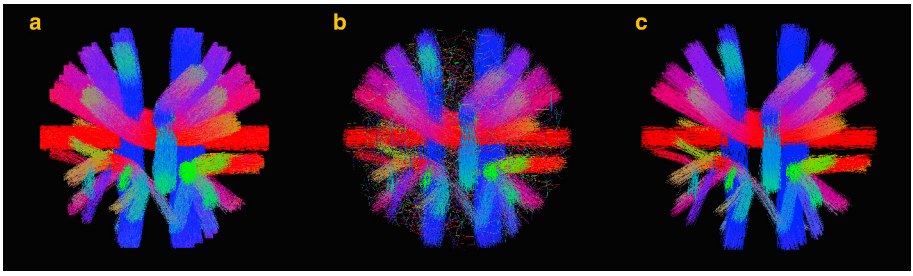

Figure 3.5: Reconstruction of the simulated phantom at SNR 20: (a) probabilistic streamline tracking on the fODF, reconstructed using multi-shell multi-tissue CSD, (b) MITK global tractography, and (c) our method using the multi-shell multi-tissue model.

3.4.2 In vivo data

The total processing time of MSMT-GT for a full brain tractogram with the specified parameter settings was about 4 h for dataset 1 and 3 h for dataset 2 (standard desktop running 4 parallel threads). By comparison, MITK-GT took around 4 h for dataset 1 and 2 h for dataset 2. Streamline tracking (iFOD2) is much faster, but full-brain MSMT-CSD also took over 4 h in dataset 1 and around 30 min in dataset 2.

The estimated volume fractions of all tissues are shown in Fig. 3.6 for both datasets. The segment density map (WM fraction), and the CSF and GM fractions, have the contrast expected from these tissues, although the segment density exhibits a slight drop in crossing fibre regions. The residual error map is expressed as the root-mean-squared (RMS) error between measured and simulated data, relative to the WM scaling, i.e., the square root of the first term in (3.8): $\|D - D'\|/\sqrt{Q}\,K_0$. This relative error is fairly homogeneous in each

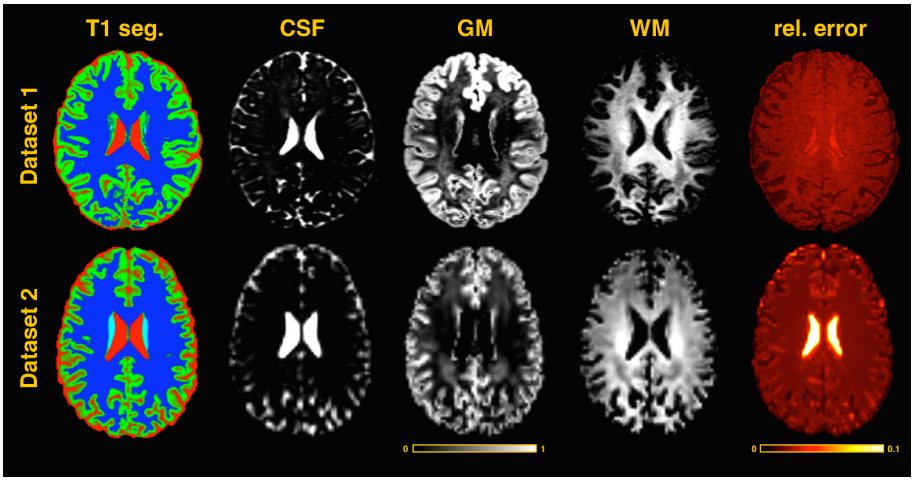

Figure 3.6: Axial slices of the estimated tissue fractions in both datasets: (a) a T1 segmentation for reference, (b) the fraction of cerebrospinal fluid (CSF), (c) the fraction of grey matter (GM), (d) the fraction of white matter (WM), proportional to the segment density, and (e) the residual error map, measured as the relative root-mean-squared (RMS) difference.

tissue and around 2% in WM. Ventricular CSF stands out due to its strong attenuation and high signal at $b = 0$, whereas WM is affected by the particle potential.

In Figs. 3.7–3.9, we show close-ups of the tractography results obtained with the proposed MSMT-GT method for the centrum semiovale, the fornix, and the precentral gyrus, and compare these visually to the results of MITK global tractography and MSMT-CSD. In Fig. 3.7 for dataset 2, the tracks from the corpus callosum radiate laterally, crossing the corona radiata and the superior longitudinal fasciculus. This can also be observed in the fODFs, displayed at the bottom of that figure, which are produced as an ancillary result of our global tractography approach and closely resemble the fODFs produced by MSMT-CSD. With MITK-GT, we observe spurious fibres at the edge of the ventricles and few tracks radiating laterally. Fig. 3.8 shows part of the fornix in the mid-sagittal plane, as well as the corpus callosum and the anterior commissure, overlaid on a map of the estimated CSF fraction. The partial volume effect between the ventricles and the surrounding WM structures is explicitly modelled and introduced little to no spurious peaks in the fODFs. Compared to MITK-GT, our approach produced fewer spurious fibres in PVE regions. Fig. 3.9 shows the association fibres connecting grey matter areas in the

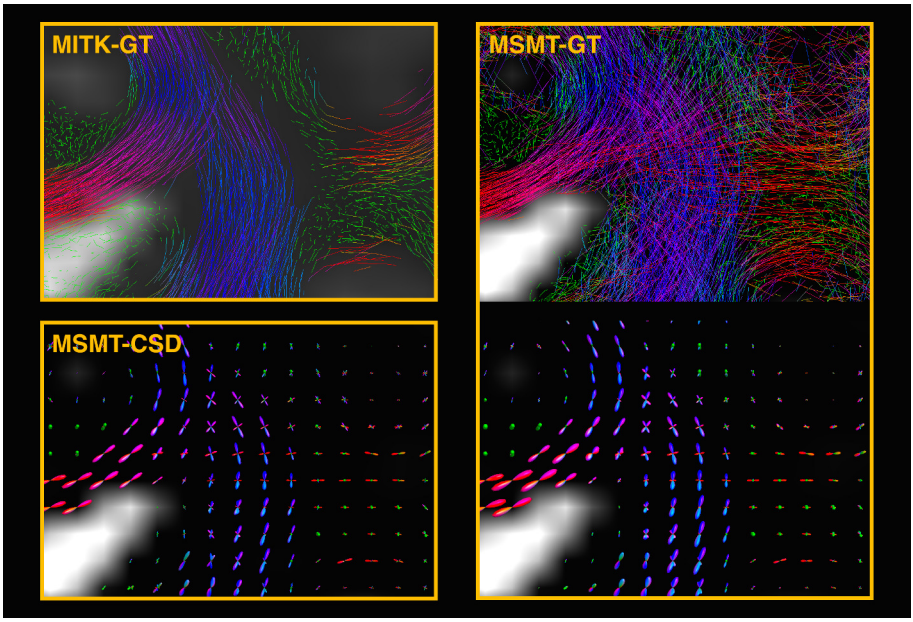

Figure 3.7: Centrum semiovale of in vivo dataset 2. Right: the tracks within a coronal slab of 2.5 mm and the associated fODFs, overlaid on the estimated CSF fraction. Top left: corresponding view of the tracks in MITK-GT, overlaid on the $b = 0$ image. Bottom left: fODFs in MSMT-CSD, overlaid on the CSF fraction estimated in MSMT-CSD.

motor cortex (precentral gyrus) and the premotor cortex (middle frontal gyrus). Compared to MSMT-CSD, our approach underestimates the WM fraction at the WM-GM interface due to the imposed particle potential. Without such prior, tracks run deeper into cortical GM, but also falsely connect through the precentral sulcus.

In addition, we segmented white matter bundles based on the protocol outlined in Wassermann *et al.* [164], which *queries* tracks based on their anatomical position w.r.t. a cortical parcellation. We show 5 segmented fibre bundles in Fig. 3.10 and compare them qualitatively between methods. For the given segmentation, iFOD2 streamline tracking produces dense fibre bundles which successfully delineate the anatomical structures. Global tractography results are less dense due to many short tracks that do not reach the inclusion ROIs. Nevertheless, a clear improvement of the MSMT model over MITK can be observed, particularly in the corpus callosum and the uncinate fasciculus.

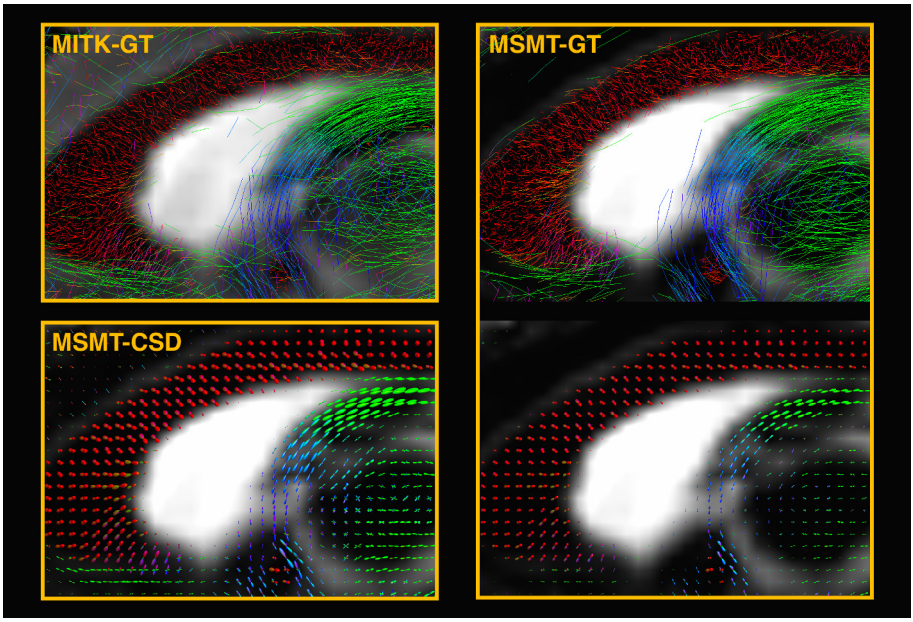

Figure 3.8: Sagittal view of the fornix of in vivo dataset 1. Right: the tracks within a slab of 2.5 mm and the associated fODFs, overlaid on the estimated CSF fraction. Top left: corresponding view of the tracks in MITK-GT, overlaid on the $b = 0$ image. Bottom left: fODFs in MSMT-CSD, overlaid on the CSF fraction estimated in MSMT-CSD.

In dataset 1, we found that 62.9% of all white matter voxels contains crossing fibres, and 32.2% contains a 3-way crossing, which is consistent with previous estimates [56]. The histogram of the track length is shown in Fig. 3.11 and closely fits an exponential distribution.

3.5 Discussion

3.5.1 Multi-shell, multi-tissue global tractography

Mapping the human connectome in vivo by tractography is only meaningful when the track distribution, if not every track, truly represents some property of the neural tissue. At the very least, the density of the reconstructed full-brain tractogram should correspond to the apparent fibre density (AFD) in the measured DWI data [113, 117]. Streamline tractography, due to its dependence

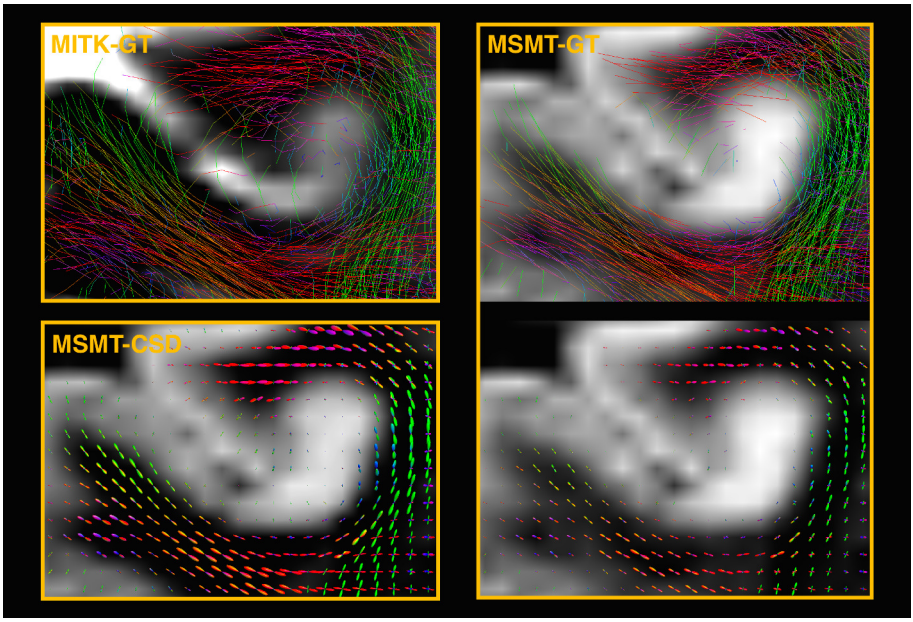

Figure 3.9: Axial view of the inferior part of the precentral gyrus and the middle frontal gyrus of in vivo dataset 1. Right: the tracks within a slab of 2.5 mm and the associated fODFs, overlaid on the estimated GM fraction. Top left: corresponding view of the tracks in MITK-GT, overlaid on the $b = 0$ image. Bottom left: fODFs in MSMT-CSD, overlaid on the GM fraction estimated in MSMT-CSD.

on the seeding distribution and hard thresholds on curvature, FA, or fODF amplitude, lacks any quantitative correspondence to the data and is therefore not suited for measuring connectivity [154].

Both generative and discriminative methods have been presented which ensure this correspondence. Discriminative methods [156, 157, 159, 161] start from a dense superset of fibre tracks and filter it until it corresponds to the fODF or the data in a convex optimization framework. Their main advantage is that anatomical constraints can easily be incorporated [144, 162]. On the downside, these methods have been shown to depend on the input superset [159], especially regarding false negatives. On the other hand, generative global tractography methods [141–143, 145] directly optimize the tractogram to the data given a generative signal model and priors on the track configuration.

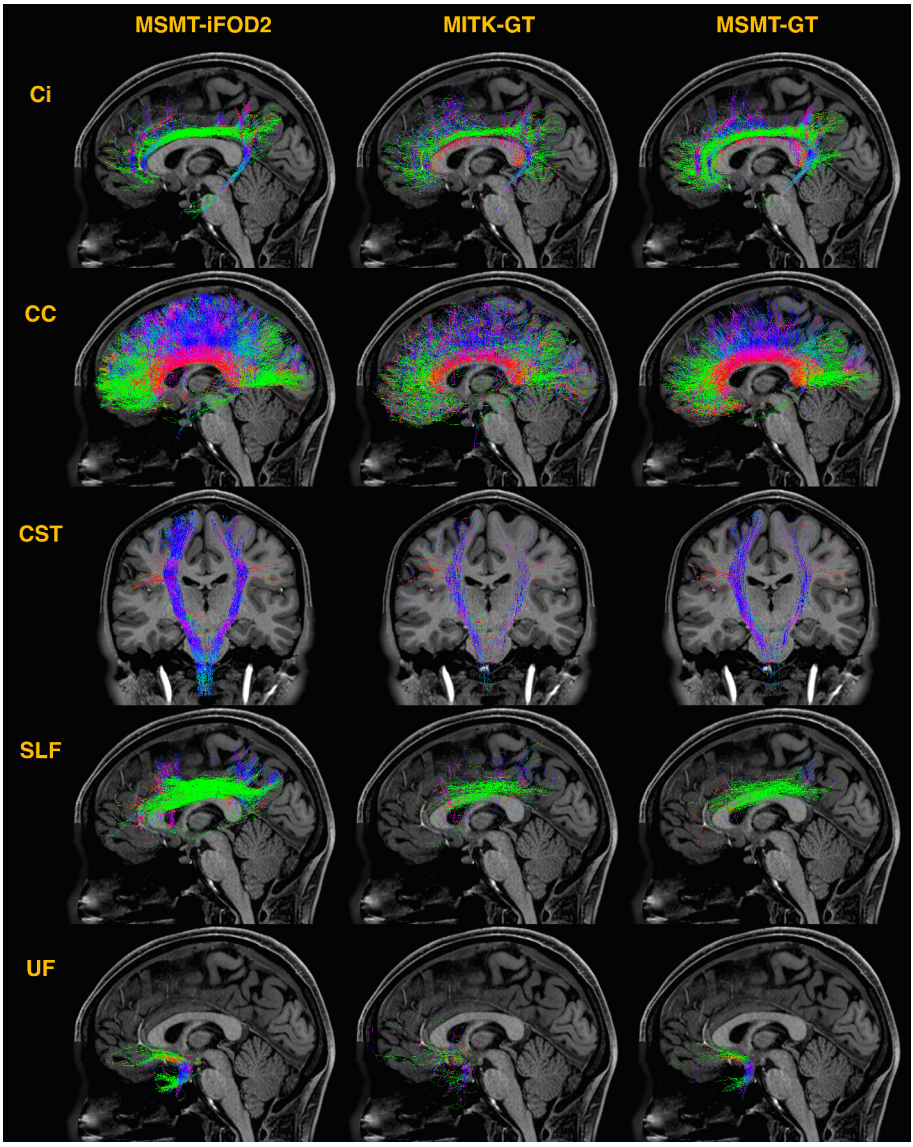

Figure 3.10: Segmented fibre bundles in dataset 1. From top to bottom: the right cingulate tract (Ci), the corpus callosum (CC), the left and right corticospinal tracts (CST), the right superior longitudinal fasciculus (SLF), and the right uncinate fasciculus (UF).

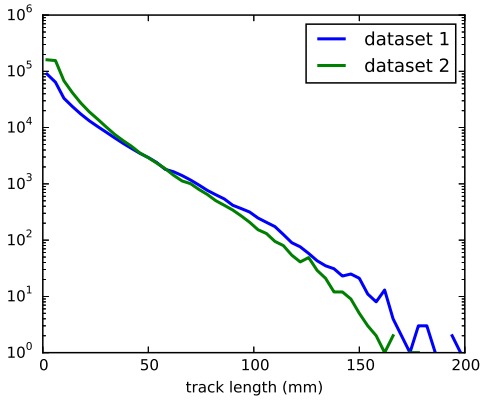

Figure 3.11: Histogram of the track length, computed across 50 bins in the range of 0 to 200 mm. Notice the log-scale on the vertical axis.

Our approach extends the generative signal model to arbitrary, multi-shell fibre response functions. While this kernel can be modelled in many ways, we propose to estimate it from the dataset at hand, specific to a subject or study. In this way, the presented approach is not restricted to fixed microstructural models, unlike previous work [142, 143]. Compared to Reisert *et al.* [145], which jointly estimates the global track configuration and the local parameters of a biexponential microstructure model, our approach is less computationally demanding.

In line with Jeurissen *et al.* [118], we also extended the generative model for multiple tissue classes to explicitly account for partial volume effects (PVE). By including isotropic response functions for non-white matter tissues such as grey matter and CSF, we can obtain a probabilistic segmentation of these tissues in the raw diffusion data, as illustrated in Fig. 3.6. As such, our GT method only requires a (rough) brain mask, whereas current global tractography methods typically require a white matter mask.

The global tractography method is, at the same time, a spatially-regularized fODF reconstruction method, adapted for multi-shell HARDI data and multiple tissue types. The fODF is produced as an ancillary result, based on the segment distribution, in a similar way as the track orientation distribution (TOD) [221]. However, as global tractography matches the track density to the underlying data, the TOD becomes the fODF. The spatial regularization stems from the interaction between neighbouring segments, rather than voxels, which allows to adapt its scale to the structures of interest.

Finally, while the data energy of our global tractography method assumes Gaussian noise, the noise model in real data is Rice or noncentral χ distributed, depending on the image reconstruction, and may bias tractography [222, 223]. However, by estimating the tissue response functions from the data under the same assumption, the kernels incorporate this noise bias as well, and represent not the actual tissue response, but rather expectations of the actual response under non-Gaussian noise. As such, our data-driven approach counteracts some of the effects of a Rician noise bias under the more general assumption of stationary (spatially dependent) noise. In accelerated imaging techniques, the noise distribution is not stationary, but can be well approximated as Gaussian for sufficiently high SNR [223]. Both datasets used in this work are of sufficient quality to support this approximation: for dataset 1 (HCP), Sotiropoulos *et al.* [224] reported SNR values around 10 for shell $b = 3000\,\mathrm{s/mm^2}$; for (in-house) dataset 2, Veraart *et al.* [225] estimated the median SNR at 8.42 for shell $b = 2800\,\mathrm{s/mm^2}$.

3.5.2 Response function estimation

In this work, we have used a *supervised* kernel estimation method, based on tissue segmentations obtained from a T_1-weighted image (T1). The advantage of such approach is that it allows the user to carefully select the desired kernels. The disadvantage is that T1 needs to be available and needs to be aligned to the DWI data[1]. When this is not the case, tissue classes might be segmented directly on the DWI data [226, 227] or a number of representative (low PVE) voxels can be manually delineated. Alternatively, one can resort to an *unsupervised* method, independent of any prior tissue segmentation. In the Appendix to this chapter, we describe a method, based on non-negative matrix factorization, in which an arbitrary number of isotropic kernels are automatically estimated from the data. The resulting kernels closely match those of the supervised procedure, as does the global fibre reconstruction. We further extend this method to anisotropic kernels in Chapter 6.

One limitation of the selected WM/GM/CSF representation, is that spurious segments can occur in non-WM regions that are not explicitly modelled, particularly in the dura mater and the cerebellar tentorium. Trapped water in these membranes yields a low signal attenuation with increasing b-value, which is most closely represented by the WM kernel. As shown in Fig. 3.2, white matter has the lowest attenuation of the modelled tissues, and therefore fits well in highly restrictive compartments. This touches upon a fundamental limitation of the multi-shell multi-tissue model, which we call *kernel conditioning*. The

[1] Actually, the DWI data should be corrected for EPI distortions, for example using a reverse-phase encoding acquisition protocol [215].

b-value attenuation of all kernels must be sufficiently distinctive to allow robust segmentation of the corresponding tissue types. Nevertheless, the effect of not modelling surrounding tissues such as the dura can be largely mediated with a proper brain mask and with the use of the particle potential.

3.5.3 Tractometer results

Tractometer analysis of the effect of the particle and connection potential has shown that no single parameter setting performs best by all measures. Instead, they can be tuned by the user depending on the application. For example, for connectome analysis one could maximize VC/(VC+IC) by decreasing the connection potential, at the cost of a reduced total connection rate. For bundle segmentation, on the other hand, a higher connection potential could increase VC (to be segmented) at the cost of a higher IC (to be excluded by the segmentation). Similar observations have been made in streamline tractography, where it has been pointed out that no single parameter setting for, e.g., the step size or the maximum curvature, optimizes all tractometer metrics [185, 219].

The comparison to alternative methods shown in Fig. 3.4 demonstrates that the presented approach yields a high valid connection ratio and low IB. Compared to the ball-and-stick model used in MITK, the multi-shell multi-tissue model strongly improves the reconstruction, especially in the low SNR range. As shown in Fig. 3.5, explicitly accounting for multiple tissue types in global tractography reduces spurious fibres in GM regions. Additionally, we found that the improvement in VB between MITK and our approach also relates to PVE, particularly in bundles near phantom “CSF” regions. Furthermore, calibrating the white matter model to the data at hand helps to increase VC and reduce NC, which ultimately reflects in an improved VC/(VC+IC) ratio.

Compared to probabilistic streamline tractography on fODFs obtained from MSMT-CSD [118], our method has a higher valid connection rate but a lower total connectivity rate. This relates to a general issue with global tractography that tracks can start or end in WM due to their segment representation. Moreover, this phantom is inherently difficult for global tractography, as it assumes constant AFD in crossings (without increasing the volume of the crossing bundles), which is in conflict with the superposition of segments in our model. Streamline tracking, which does not ensure corresponding fibre density, is not affected by this assumption of the phantom.

3.5.4 In vivo results

The resulting full brain reconstructions are consistent with known anatomy, and correctly trace challenging structures, including the anterior commissure and short association fibres. The volume fraction maps shown in Fig. 3.6 exhibit the contrast expected from these tissues. However, the segment density contains a slight decrease in crossing regions, whereas the grey matter fraction is elevated at the corresponding positions. The WM signal in crossings can be more isotropic and can therefore more closely resemble grey matter, especially in combination with the particle potential. However, the reconstruction of the centrum semiovale (Fig. 3.7) shows that this effect is small in practice.

Figs. 3.7–3.9 illustrate that the presented method explicitly models partial volume effects between neighbouring tissues, and hence produces fODFs that are qualitatively similar to results obtained from MSMT-CSD [118]. However, while MSMT-CSD optimizes the data likelihood only, MSMT-GT imposes additional priors on the particles and connections. As such, additional spatial regularization and sparsity is achieved. For example, in Fig. 3.9, the particle potential has slightly suppressed the track reconstruction at the WM-GM interface, where the data provides less evidence, and hence avoided false connections through thin sulci. Similarly, the connection potential increases support for segments that align well with their neighbouring segments. Ultimately, these priors aim to improve the specificity of the track reconstruction.

For the purpose of bundle segmentation, the results of MSMT-GT are on par with probabilistic streamline tractography and show improvement over MITK-GT. Streamline tractography delineates the long-range WM bundles nicely, facilitated by the absence of any requirement to match AFD. MSMT-GT was able to reconstruct similar fibre bundles, except for the inferior part of the CST that is missing from the segmentation. By comparison, MITK-GT produced less organized tracks, particularly in the corpus callosum.

The track length histograms in Fig. 3.11 show a strongly skewed distribution, with high prevalence of short fibres and much lewer long-range connections. This result supports existing hypotheses about the efficient organization of the brain in which proximate regions are more densely connected [228–231], and is consistent with recent observations by R. E. Smith *et al.* [161]. Nevertheless, it is yet unclear if this truly represents the distribution of the neuronal fibre length, and to which extent it is affected by the global tractography method.

3.5.5 Future perspectives

The proposed method is calibrated to the data at hand, via a kernel that represents healthy tissue across the entire brain. A first area of future research lies in evaluating the method on pathological cases, possibly including kernels for tumour and edema tissue. Another extension would be to adapt the fibre response function to the local microstructure by allowing some degrees of freedom, in line with recent work by Reisert *et al.* [145].

Secondly, global tractography may benefit from including additional priors on the expected track configuration, e.g., enforcing anatomical constraints [144, 162] or imposing a prior on the local track orientation [24]. Such priors may improve the quality of the track reconstruction or increase its robustness against low resolution or low SNR data. Furthermore, the ability of our method to simultaneously segment the WM-GM interface without relying on atlases or other imaging modalities opens new possibilities for defining priors on, e.g., track bending or endpoints.

3.6 Conclusion

The goal of this work was to introduce a data-driven approach to global tractography, independent of a specific biophysical model. Instead, we rely on multi-shell tissue response functions, estimated from the data itself and adapted to the subject or study, for jointly reconstructing white matter fibres and the fODF, and estimating volume fractions of adjacent tissues. The findings that we have presented suggest that calibrating the fibre response and handling partial voluming in this way improves the quality of tractography. As such, we have integrated local and global reconstruction of white matter, matched to the apparent fibre density in the DWI data, and segmentation of grey matter and CSF into one comprehensive framework. The presented work is an important step towards quantitative tractography, and ultimately assessing white matter structure and connectivity in healthy subjects and patients.

Appendix: Unsupervised kernel estimation

The estimation of the isotropic kernels for CSF and GM as described in Section 3.2.2 was based on a tissue segmentation from a T1-weighted image. Here, we propose an alternative, unsupervised kernel estimation method that relies only on the DWI data at hand.

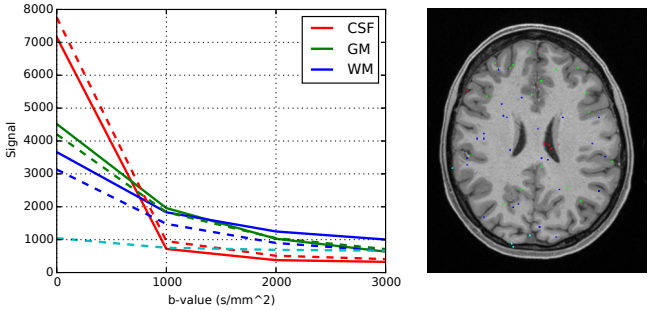

Figure 3.12: Unsupervised kernel estimation. Left: Plot of the isotropic kernels estimated as described in Section 3.2.2 and shown in Fig. 3.2 (solid lines), and the four kernels estimated by the unsupervised method (dashed lines) on dataset 1. Right: Voxels of which these kernels are a weighted average, depicted in the corresponding colours.

We average the raw diffusion signal on every shell to obtain, in each voxel $\mathbf{r}$, a vector of the mean isotropic diffusion signal per b-value, $\hat{D}(\mathbf{r}, b)$. Then, by the isotropic part of (3.7), $\hat{D} \approx C\,F$, in which C is a matrix containing the isotropic kernels for all tissues, including WM, in its columns, and F contains the isotropic fractions of those tissues. We then minimize $\|\hat{D} - C\,F\|^2$, s.t. $C > 0, F > 0, \mathbf{1}^T F = 1$, and impose the additional constraint that all kernels should be a convex combination of the original data points $\hat{D}$. This problem is commonly known as convex non-negative matrix factorization (CNMF) [232].

We took a random subsample of 3000 voxels within the brain mask of dataset 1, and solved the CNMF problem using the iterative algorithm outlined in Ding *et al.* [232]. The kernels were initialized with the centroids of a k-means clustering in the 4-dimensional space of this dataset (b-values). When using 4 kernels, we obtained a close correspondence to the original WM, GM and CSF kernels used in this chapter, as well as a fourth kernel of low attenuation that corresponds to a highly restrictive compartment (Fig. 3.12 left). The right part of Fig. 3.12 shows the weights by which each voxel contributes to the kernels of corresponding colour, which converge to a sparse set in CNMF [232]. The voxels contributing to the CSF and GM kernels are indeed sampled in the respective tissues. The fourth component is sampled in the dura. This illustrates that tissue kernels can be estimated from multi-shell DWI data directly, even when no T1w-image is available.

Acknowledgements Data were provided in part by the Human Connectome Project, WU-Minn Consortium (Principal Investigators: David Van Essen and Kamil Ugurbil; 1U54MH091657) funded by the 16 NIH Institutes and Centers that support the NIH Blueprint for Neuroscience Research; and by the McDonnell Center for Systems Neuroscience at Washington University. The authors also wish to thank Emmanuel Caruyer for providing the software phantom, Thibo Billiet for providing in house dataset 2, and Jelle Veraart for estimating the noise level in this dataset.

Chapter 4

Population priors in global tractography

The work in this chapter was published in

D. Christiaens *et al.*, "Atlas-guided global tractography: Imposing a prior on the local track orientation", in *Computational Diffusion MRI – MICCAI Workshop*, L. O'Donnell *et al.*, Eds., ser. Mathematics and Visualization, Cambridge, MA, USA: Springer International Publishing, Sep. 2014, pp. 115–123

and

D. Christiaens *et al.*, "Imposing label priors in global tractography can resolve crossing fibre ambiguities", in *International Society for Magnetic Resonance in Medicine (ISMRM) 23th Annual Meeting & Exhibtion*, vol. 23, Toronto, Ontario, Canada, May 2015, p. 2258.

4.1 Introduction

Since its introduction over a decade ago, diffusion tractography has come a long way from local, deterministic, then probabilistic approaches, towards global tractography [146, 210], steadily gaining importance for *in vivo* neuroanatomy studies and neurosurgical planning. Deterministic streamline approaches [20] are highly sensitive to local estimation errors, leading to low accuracy, sensitivity and specificity of the reconstructed tracks in the presence of noise, modelling errors, and partial volume effects [210, 233]. Probabilistic fibre tracking can

accommodate for this uncertainty [233], but won't improve the accuracy of each individual streamline. Moreover, streamline tractography is inherently difficult to quantify due to its dependence on the seeding distribution. Global fibre tracking methods [140–143] aim to reconstruct the ensemble of fibres that best explain the measured DWI data [146]. By addressing the problem at a global scale, these methods can be less sensitive to local estimation errors and maintain a quantifiable correspondence to the data.

Yet, the development of tractography methods has been largely focused on single subject data, and very little on cross-population analysis and inter-subject variability. Indeed, while atlases are at the core of state-of-the-art segmentation and label fusion methods [234], their use in diffusion tractography is mostly limited to automated and consistent delineation of regions of interest for seeding, inclusion, and exclusion in streamline tractography, and for clustering and labelling of the resulting fibre tracks [163]. In regard to streamline tractography, Cook *et al.* [235] have demonstrated the use of a diffusion tensor atlas as a prior distribution for the fibre orientation. Yap *et al.* [236] have similarly used a distribution of the maxima of the fibre orientation distributions (FOD) in different subjects, as a means of improving tractography of the average atlas. At the global image scale, R. E. Smith *et al.* [162] and Lemkaddem *et al.* [144] have imposed anatomical constraints on the track end points in streamline and global tractography. In addition, Yendiki *et al.* [237] have imposed a shape prior on individual pathways connecting segmented end regions in a Bayesian semi-global tractography framework [238].

Here, we extend the global tractography framework developed in the previous chapter with local and global population priors in the form of an atlas. We hypothesize that these priors may improve the overall quality and specificity of the fibre reconstruction, as they may guide the MCMC optimization towards the global minimum and/or exclude anatomically implausible solutions. Local and global priors were evaluated in two separate experiments: one imposes a prior on the local track orientation, the other imposes a prior on the global bundle label that individual fibres belong to. Both of course require atlases of different form, which we will assume are given for the purpose of this chapter. In Chapter 5, we will then discuss atlas construction from population data in more detail.

4.2 Imposing a prior on the local track orientation

First, we incorporate a local fibre orientation prior, represented as a population atlas of the track orientation distribution (TOD) [221]. This atlas is derived from 20 normal subjects and represented in the basis of spherical harmonics (SH). The TOD captures both the expected fibre directions and their support by the local neighbourhood. We expect this atlas to guide the global tractography towards a more targeted reconstruction, due to its high angular contrast.

4.2.1 Method

Given an atlas A of the local track orientation, the posterior probability of the fibre model (3.1) of the previous chapter is extended to

$$P(\mathcal{M}|D, A) \propto P(D|\mathcal{M}, A)\, P(\mathcal{M}|A) \tag{4.1}$$

$$\propto P(D|\mathcal{M})\, P(A|\mathcal{M})\, P(\mathcal{M}) \quad , \tag{4.2}$$

using Bayes' rule and assuming the subject data is independent of the atlas. Hence, the posterior probability of the fibre model $\mathcal{M}$ is proportional to the data likelihood, the atlas likelihood, and the internal prior of the fibre model itself. Assuming the usual Gibbs distribution, the new energy function becomes

$$E(\mathcal{M}) = E_{\text{data}}(\mathcal{M}, D) + E_{\text{atlas}}(\mathcal{M}, A) + E_{\text{con}}(\mathcal{M}) \; . \tag{4.3}$$

Hence, the atlas prior directly extends the global tractography framework introduced in Chapter 3 with an additional energy term. The resulting fibre configuration can thus be optimized in the same way.

We define the atlas energy $E_{\text{atlas}}(\mathcal{M}, A)$ as the L_2-distance between the predicted fibre ODF $\tilde{\Psi}(\mathbf{r}, \mathbf{u})$ and the atlas TOD $\tilde{\Psi}_a(\mathbf{r}, \mathbf{u})$. The predicted fODF is related to the intermediary segment ODF $\Psi(\mathbf{u})$ introduced in (3.6) by convolution with an apodized point spread function (aPSF) [239], i.e., $\tilde{\Psi}(\mathbf{u}) = \text{aPSF} * \Psi(\mathbf{u})$. This apodized PSF is defined as the sharpest nonnegative function that can be represented in the SH basis of order $\ell_{\max}$. The convolution thus results in a nonnegative distribution that is more robust to SH aliasing effects. The atlas TOD is similarly assumed to be a strictly nonnegative representation of the local orientation of the tractogram.

According to Parseval's theorem, the L_2-distance between ODFs equals the sum of squared differences between their corresponding SH coefficients. In the spirit of Dhollander *et al.* [221], we propose to use a minimum track length threshold for the atlas TOD, which emphasizes neighbourhood support of the local track

orientation. As discussed in Chapter 3, the distinction between the fibre ODF, which relates to the data, and the TOD, which is a direct representation of *any* tractogram, is mute in global tractography where the latter is directly optimized to correspond to the former. However, if the tractogram is postprocessed by imposing a minimum track length, the distinction does matter.

4.2.2 Experimental setup

Data

Data of 25 neurologically healthy subjects between ages 22 and 35 years old were provided by the WU-Minn Human Connectome Project (HCP) Q3 data release [202]. The diffusion data consists of 3×90 gradient directions at b-values 1000, 2000, and 3000 $\mathrm{s/mm^2}$ and 18 non-diffusion weighted images ($b = 0$), at an isotropic voxel size of 1.25 mm, and was corrected for motion and EPI distortions as described in [214]. In each subject, the white matter (WM) response function was estimated in a fractional anisotropy (FA ≥ 0.75) mask using standard techniques for all shells [91]. Isotropic grey matter (GM) and cerebrospinal fluid (CSF) kernels were estimated as the average signal in manually delineated regions. Finally, the kernels of all subjects were averaged to obtain one mean WM, GM and CSF kernel.

Atlas Construction

The atlas was constructed out of 20 randomly selected subjects, using global tractography without atlas prior as described in Chapter 3 in each subject individually. The segment length was set to 2 mm, the maximal order of the SH basis to $\ell_{\max} = 10$, and the weight of each segment to 0.1, such that on average 10 segments per white matter voxel are reconstructed. We ran the MH sampler for 10^9 iterations, which took around 10 hours (single-threaded) on a standard desktop computer.

The resulting fibre segments were normalized to MNI space, using the non-linear warps provided by the HCP and originally obtained with FSL FNIRT [214, 240, 241]. The centre point of each segment is transformed to MNI space and its direction is reoriented according to the Jacobian of the local deformation field. Next, we imposed a minimum track length threshold, such that only tracks consisting of at least 10 segments remained, corresponding with a minimum track length of 20 mm. These segments were subsequently transformed and reoriented to the space of the 5 remaining subjects for testing. Finally, the set of transformed and filtered segments of all subjects was converted to an ODF

Table 4.1: Mean track length and total number of tracks for all test subjects.

	uniform prior		atlas prior	
Subject	avg. length	no. tracks	avg. length	no. tracks
1	16.05 mm	281 403	19.27 mm	131 196
2	17.04 mm	211 759	21.93 mm	112 591
3	16.16 mm	249 838	20.48 mm	119 286
4	16.79 mm	199 610	21.93 mm	109 324
5	16.98 mm	221 455	21.57 mm	116 499

representation using aPSFs as described in Section 4.2.1. Conceptually, this is identical to existing methods for ODF reorientation and atlas construction [26, 239], except that those methods first fit a weighted sum of uniformly oriented aPSFs to the data in every voxel. The segment representation, used in global tractography, allows to avoid this fitting step.

4.2.3 Results

The effect of the proposed atlas prior was evaluated in the 5 remaining subjects, using identical parameter settings as for the initial global tractography. First of all, the mean track length, reported in Table 4.1, is exponentially distributed and increases significantly with the atlas prior (F-test, p-value 10^{-6}) by about 25 %. Simultaneously, the imposed atlas prior reduces the number of tracks by approximately 50 %. These observations indicate that while the overall density decreases, mostly the number of short, incomplete or interrupted tracks is reduced by the atlas prior.

Figure 4.1 shows a cross-section of the reconstructed tractogram of test subject 1, and illustrates that the decreased track density with use of the atlas prior is mainly located in the distal gyri. All major WM bundles are present in the reconstruction, and the crossing of the corpus callosum, the corona radiata, and the superior longitudinal fasciculus, sometimes challenging for tractography, is successfully recovered in both global tractography reconstructions, with and without the atlas prior. However, a close-up of the fibre ODF in this region, as shown in Fig. 4.2, illustrates that the main fibre directions are more consistent across neighbouring voxels when using the atlas prior. Similar results were observed in the remaining test subjects (not shown). This result demonstrates that, although the information contained in the atlas is only local, the imposed minimum track length ensures “track-like local support” in the neighbouring voxels [221], which guides the fibre reconstruction to more targeted results.

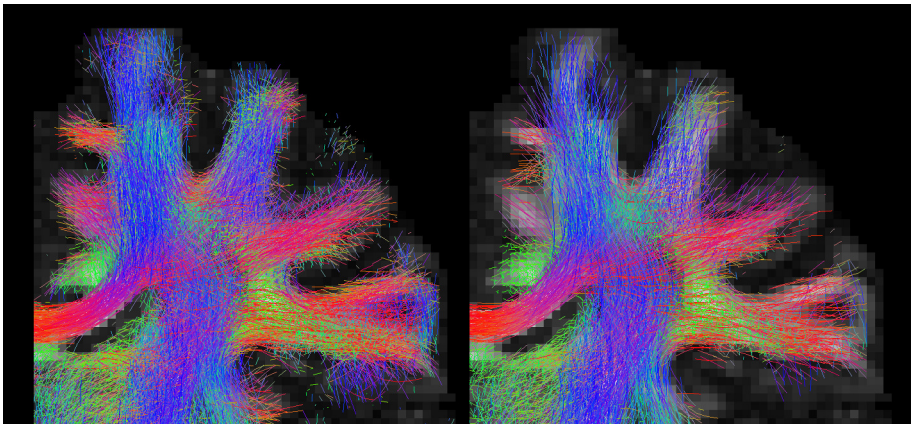

Figure 4.1: Coronal slab (5 mm) of the reconstructed tractogram in the cerebrum, overlaid on a fractional anisotropy map, without atlas prior (*left*), and with atlas prior (*right*).

Nevertheless, Figs. 4.2 and 4.1 also show a shortcoming of the proposed strategy in their top left corners. Namely, the fibres in distal gyri are strongly suppressed with the imposed atlas prior. Indeed, the L_2-distance used in the definition of the atlas energy is sensitive to track density, which may affect the reconstruction if a null-prior is mapped to a certain region due to registration effects. Distal gyri are particularly sensitive to this effect due to their proximity to sulci and cortical grey matter.

Finally, we segmented the left cingulate tract in both reconstructions based on a WM parcellation obtained with FreeSurfer [242] following the protocol described in [164]. As shown in Fig. 4.3, the atlas prior strongly reduces the amount of false positive tracks that run from the cingulum into the corpus callosum. This illustrates that incorporating the atlas prior can improve specificity and suppress spurious fibres in the reconstruction.

4.3 Imposing global label priors

Conventional tractography suffers from ambiguous local fibre configurations, due to partial voluming and the symmetry of DWI data [146, 210]. It is, for example, not possible to discriminate between crossing and kissing fibre bundles, as illustrated in Fig. 4.4, or between bending and fanning configurations. This local ambiguity is a leading cause of spurious (false positive) fibre tracks, as

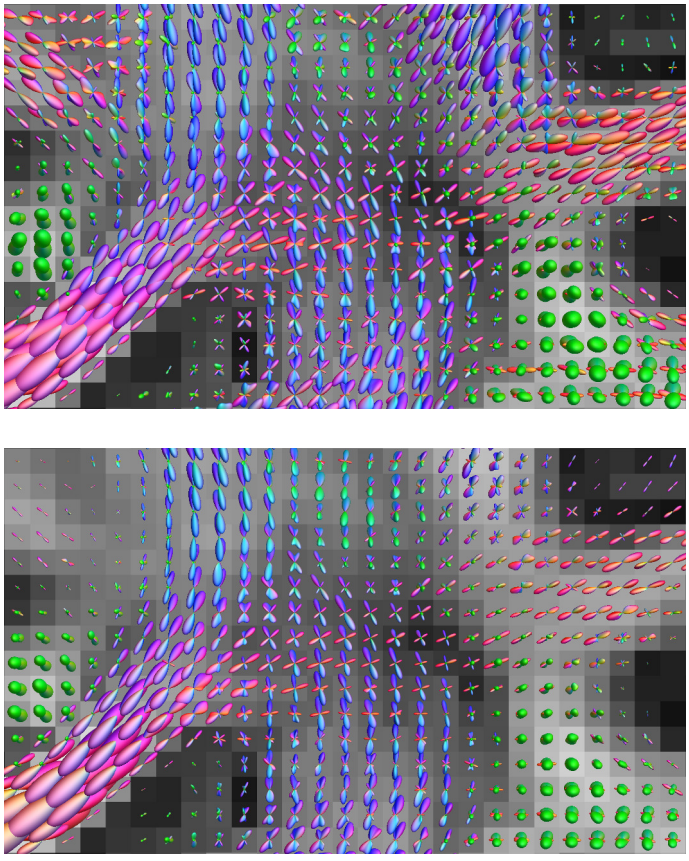

Figure 4.2: Fibre orientation distribution in the centrum semiovale, obtained without atlas prior (*top*), and with atlas prior (*bottom*). With atlas prior, the track orientations are more consistent across neighbouring voxels.

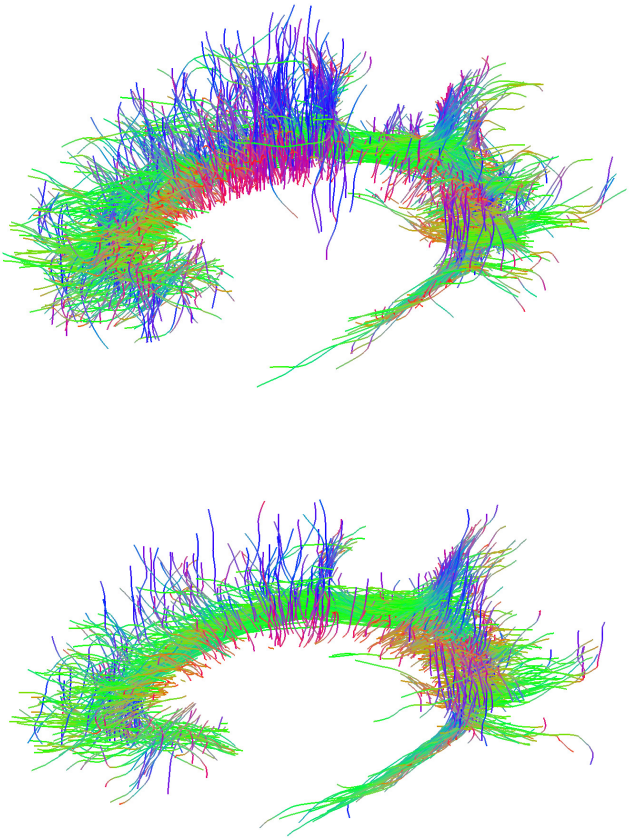

Figure 4.3: Sagittal view of the left cingulate tract, segmented from the global fibre reconstruction without atlas prior (*top*), and with atlas prior (*bottom*). Notice that with the prior, the number of false positive connections to the corpus callosum is reduced.

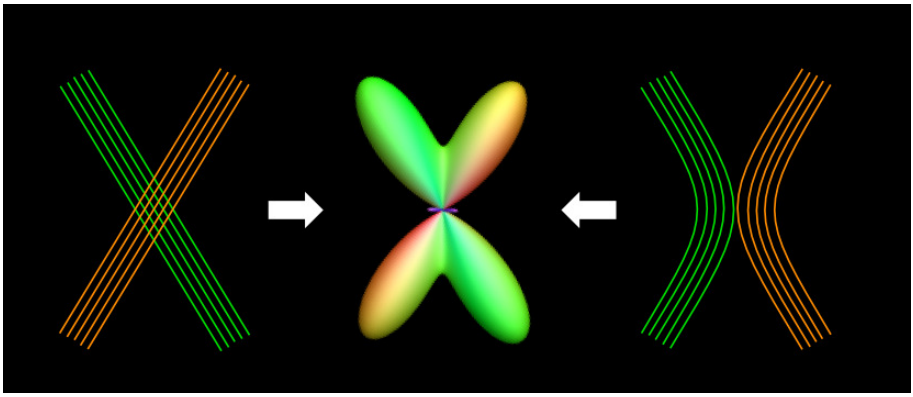

Figure 4.4: Illustration of the crossing fibre ambiguity problem. Due to the inherent symmetry of DWI data, the crossing fibre configuration on the left can not be discriminated from the kissing fibre configuration on the right while relying on local information only.

conventional tractography will typically reconstruct a mixture of all possible configurations. Selecting the "correct" configuration requires addressing the issue at a global scale, beyond the voxel.

Global tractography methods partly achieve this by optimizing the fibre density across the entire image, thus taking the AFD in adjacent voxels into account. An additional prior on the shape of the main white matter pathways could furthermore facilitate resolving such local ambiguities by explicitly excluding implausible tracks. Such is the motivation behind this second experiment, in which we use fibre bundle labels (e.g., green and orange in Fig. 4.4) as an additional prior in global tractography. We hypothesize that such prior will reduce false positive fibres. In addition, it enables *online* probabilistic segmentation of the resulting tracks in white matter bundles.

4.3.1 Method

We introduce a white matter atlas that provides a collection of label probability maps, i.e., at every position $\mathbf{x}$ the atlas determines probability $P(L_\mathbf{x} = l)$ of a bundle label $L_\mathbf{x}$ [173, 237]. We assume that the total label probability adds to one at every position, i.e., $\forall\, \mathbf{x} : \sum_l P(L_\mathbf{x} = l) = 1$. In unlabelled regions we use a uniform prior. The label probability of a track t is then defined as

$$P(L_t = l) = \prod_{\mathbf{x} \in t} P(L_\mathbf{x} = l) \quad , \tag{4.4}$$

and the total prior probability of track t given the atlas is $\sum_l P(L_t = l)$. As such, a track connecting two disjoint bundles has prior probability 0, while a track within a single bundle will have label probability 1. In practice, bundle label maps will overlap in crossings and due to atlas uncertainty, such that the attributed probabilities will not be binary. The atlas will therefore penalize tracks in these regions of uncertainty, counteracting the connection potential between segments.

The prior track probability given a label atlas could be incorporated as an additional energy term in the global optimization. However, in the context of MCMC optimization we found it more convenient to modify the acceptance probability (Green's ratio) of connection, disconnection, and move proposals. For instance, given two "half tracks" t_1 and t_2 as shown in Fig. 4.5, the Green's ratio for connecting both is weighted by the probability of their labels to be equal:

$$P(L_{t_1} = L_{t_2}) = \frac{\sum_l P(L_{t_1} = l)\, P(L_{t_2} = l)}{\sum_l P(L_{t_1} = l) \cdot \sum_l P(L_{t_2} = l)} \quad . \tag{4.5}$$

In this expression, the numerator equals the probability of the connected track t_1–t_2, whereas the denominator denotes the probability of two unconnected tracks. Segment move proposals are similarly adapted to incorporate the prior. Note that evaluating these label probabilities requires traversing the entire track, which impedes a parallel implementation.

4.3.2 Results

In silico phantom

As proof of concept, we use the Phantomas software [179] to generate data with known ground truth fibre bundles according to the ISBI Challenge geometry. The data is sampled with the HCP gradient scheme, at SNR 30 with respect to the average signal at $b = 0$. The label probability atlas is based on the ground truth fibre bundles, using equal probability of different labels in crossing bundle regions and uniform probability outside white matter. Figure 4.6 shows the full tractogram, reconstructed with MSMT-GT including these label priors. The tracks are coloured by their maximum likelihood label, which demonstrates how this framework enables atlas-based bundle segmentation. In this case, the resulting fibre bundles show high correspondence to the ground truth: no mislabelled tracks were observed, nor any tracks connecting unassociated target regions.

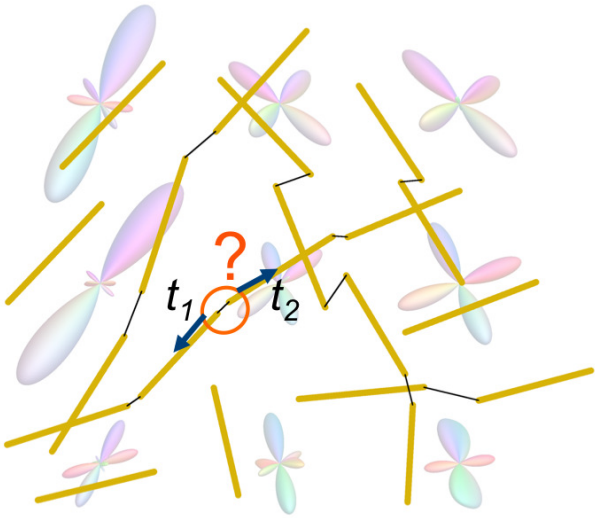

Figure 4.5: Illustration of the connection proposal with label prior. While evaluating the connection probability between two "half tracks" t_1 and t_2, the total probability of their labels to be equal is taken into account.

Table 4.2 compares the Tractometer metrics of this result to those without the label prior. With the prior, invalid connections (IC) are suppressed in favour of valid connections (VC) and at the cost of slightly increased no connections (NC). The resulting valid connection ratio increases to an almost perfect 99 %. This conceptually demonstrates that imposing a "perfect" label prior effectively suppresses false positive connections. The few invalid connections that do occur either run through the grey matter area where the prior is uniform, or they are misclassified due to edge effects at the target ROIs.

In vivo data

Data of a single subject is provided by the NIH Human Connectome Project, WU-Minn Consortium [202]: 18 gradients at $b = 0\,\mathrm{s/mm^2}$, 3×90 gradients at $b = 1000\,\mathrm{s/mm^2}$, $2000\,\mathrm{s/mm^2}$, and $3000\,\mathrm{s/mm^2}$, 1.25 mm isotropic voxel size. We use the publicly available, manually segmented DTI tractography atlas of Catani and Thiebaut de Schotten [166] that contains label probabilities of 30 white

Table 4.2: Tractometer metrics with and without atlas label prior, evaluated in the Phantomas dataset at SNR 30. The number of valid connections (VC), invalid connections (IC), and no connections (NC) are expressed as percentages relative to the total number of tracks. The no. valid and invalid bundles (VB and IB) are expressed in absolute terms.

	VC (%)	IC (%)	NC (%)	VC + IC (%)	$\frac{\text{VC}}{\text{VC+IC}}$ (%)	VB	IB
no prior	15.9	6.9	77.1	**22.8**	69.7	27	56
label prior	19.2	0.2	80.6	19.4	**99.0**	27	**9**

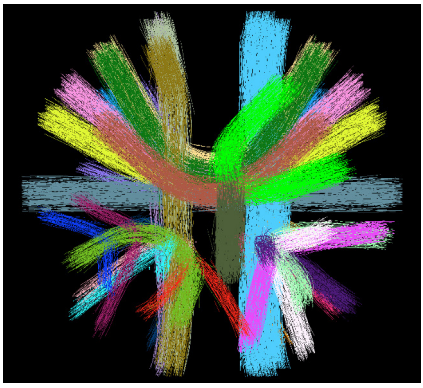

Figure 4.6: Labelled global track reconstruction in the Phantomas dataset, with 27 fibre bundles coloured by their assigned label.

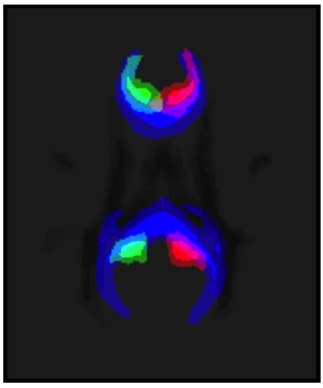

Figure 4.7: Atlas representation of corpus callosum (blue) and cingulum (green and red) label priors based on Catani and Thiebaut de Schotten [166].

matter tracts. We normalize these label probabilities at each position and use a uniform prior in unlabelled regions to create an atlas in the required format, shown in Fig. 4.7. This atlas is subsequently registered to subject-space with FSL FNIRT [240, 241].

Global track reconstruction with this label prior produces a full brain tractogram that displays similar density as without the prior. All output tracks are assigned a bundle label and an associated probability. In Fig. 4.8, these tracks are shown for label probabilities thresholded above 95 %. At this confidence level, the deep white matter tracks such as the cingulum, the fornix, and the inferior network, are reasonably well segmented. Fibres closer to the cortex, such as the arcuate and corticospinal tracts, are more challenging due to the proximity of gyral U-fibres and the tensor-based nature of the atlas. This may be improved with more detailed atlases, possibly incorporating directional label priors as well.

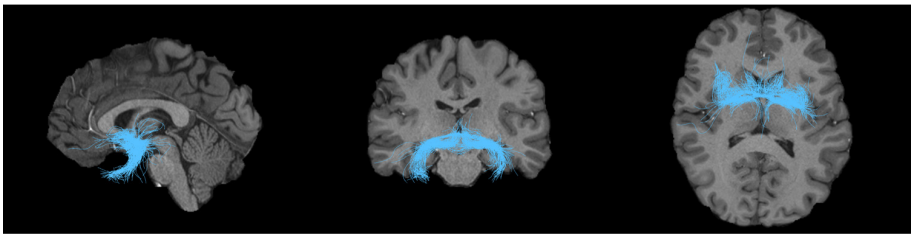

(a) Anterior commissure.

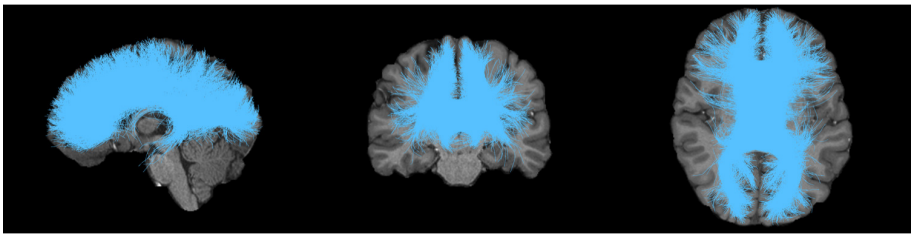

(b) Corpus callosum.

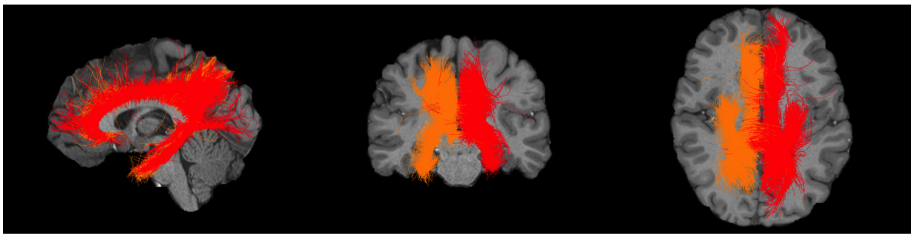

(c) Left (red) and right (orange) cingulum.

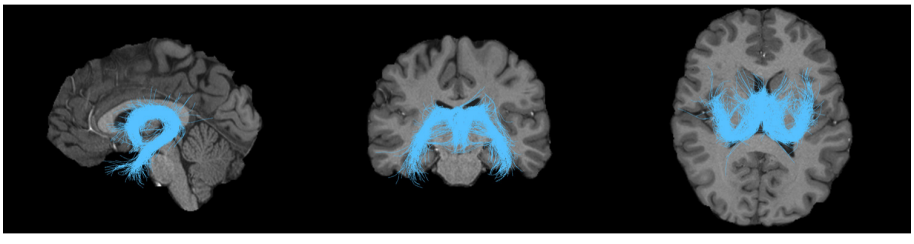

(d) Fornix.

Figure 4.8: Bundle segmentation results in global tractography with atlas label priors, thresholded at posterior label probability $p > 95\%$.

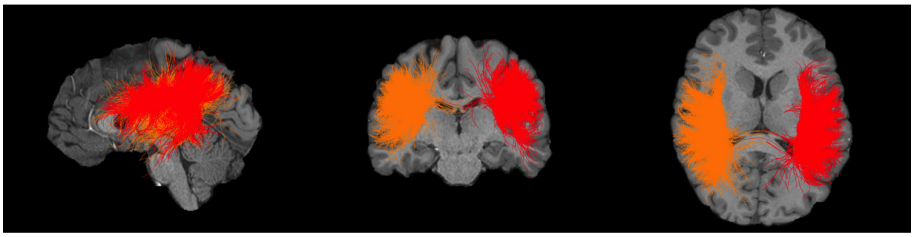

(e) Left (red) and right (orange) arcuate fasciculus.

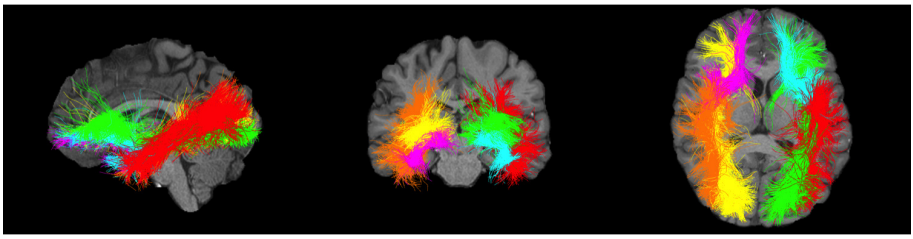

(f) Inferior network: left (red) and right (orange) inferior longitudinal fasciculus; left (cyan) and right (magenta) uncinate fasciculus; left (green) and right (yellow) inferior fronto-occipital fasciculus.

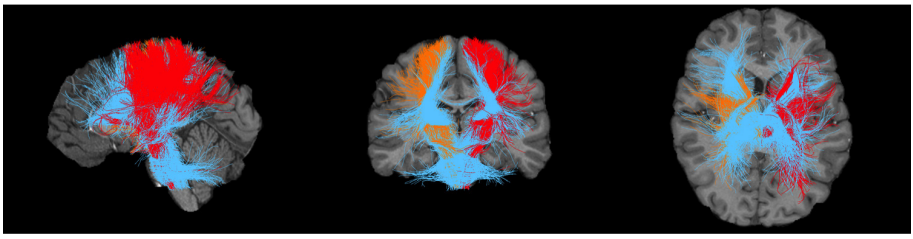

(g) Projection network: internal capsule and corona radiata (blue); left (red) and right (orange) corticospinal tract.

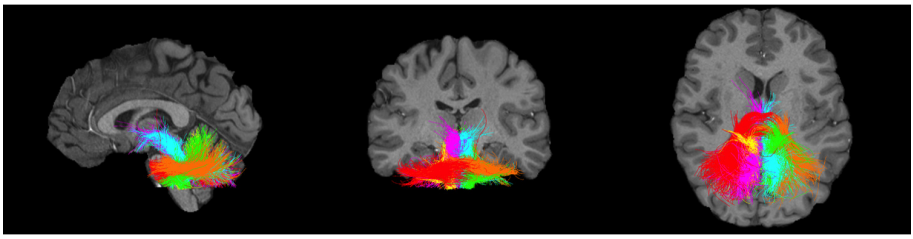

(h) Cerebellar network: left (red) and right (orange) cortico-ponto-cerebellar tract; left (cyan) and right (magenta) superior cerebellar tract; left (green) and right (yellow) inferior cerebellar tract.

Figure 4.9: Bundle segmentation results (continued).

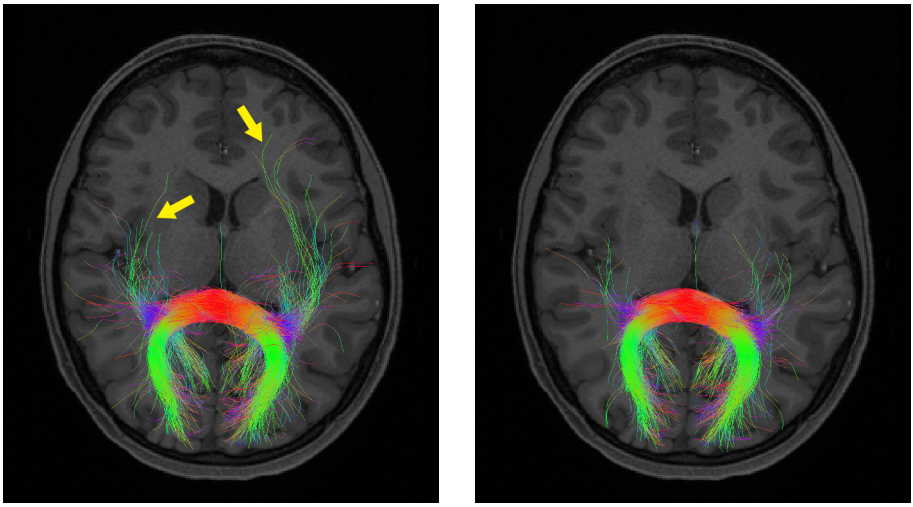

Figure 4.10: Segmentation of the forceps major without label prior (left) and with label prior (right), based on a single inclusion ROI in the splenium of the corpus callosum.

In line with the conceptual phantom evaluation, we also observe improvement of the fibre reconstruction itself. An example is shown in Fig. 4.10, in which we segmented the forceps major, the posterior substructure of the corpus callosum, with a single inclusion ROI in the mid-sagittal plane of the splenium. Without the label prior, fibres are reconstructed running towards the anterior temporal lobes. These tracts are not included in the atlas of Catani and Thiebaut de Schotten [166], and therefore implausible w.r.t. the current input. Imposing the prior reduces reconstruction of such false positive fibres. Hence, in addition to providing a probabilistic bundle segmentation, a population atlas of global tract labels can improve the fibre reconstruction itself.

4.4 Discussion and Conclusion

At a conceptual level, there are many analogies between tractography and segmentation. Both aim to delineate structures of interest, both rely on neighbourhood information for doing so, and both aim to reconstruct shapes with remarkable similarity across subjects. As such, we can expect that tractography, like segmentation, can benefit from inter-subject information in the shape of an atlas that captures the expected anatomy.

The global tractography framework is well suited for the inclusion of such atlas prior, as it aims to reconstruct the optimal fibre configuration in the whole image volume. Indeed, we have demonstrated that both local and global atlas priors of the expected track configuration can be elegantly included as additional energy terms or directly as prior probabilities in the Green's acceptance ratio during optimization. Atlas priors hence augment the internal bending and connection energy of the segment model in global tractography with additional information that may benefit accuracy and specificity of the reconstruction.

With a local track orientation prior, we observed more consistent track orientations and fewer spurious connections thanks to local support induced by the minimum length constraint. This approach is essentially interpolating between the subject and a co-registered atlas. A useful application of this technique could be to use a high-resolution atlas, built from HCP data, in conjunction with data of lower spatial and angular resolution. As such, the reconstruction of clinical data with fast acquisition schemes may be improved. However, as the reconstruction depends on the track density of the atlas, this local prior may conceal pathology-induced changes and ultimately replicate the template rather than reconstruct the subject data. Atlas energy metrics based on cross-correlation or mutual information may therefore be a wiser choice, as these are insensitive to density scaling effects.

The global label prior introduced in Section 4.3, on the other hand, contributes an entirely new source of information. This prior facilitates joint tractography and fibre bundle segmentation, which could never be achieved without atlas information. As such, a probabilistic segmentation of the white matter tracts is obtained, which can be applied in neurosurgery planning and for quantifying (micro)structural changes across pathways. In addition, we demonstrated that false positive connections are reduced in this setup, as the global label prior partly resolves the problem of local ambiguity due to DWI symmetry. This illustrates the benefits of an integrated approach, and is reminiscent of the consistency clustering framework [173] that incorporates track labelling and outlier rejection to improve specificity in streamline tractography.

Nevertheless, joint tractography and bundle labelling remains challenging in human brain data, as the atlas is inherently incomplete. Not all bundles are – and may never be – labelled, or may need to be subdivided in several hierarchical levels. In addition, some bundles are undersegmented due to the tensor-based nature of this particular atlas, e.g., the radial projections of the corpus callosum. Therefore, a prime area of improvement for this method is the development of more detailed white matter atlases based on HARDI data and across large populations.

In general, atlas-guided tractography also suffers from some of the limitations of atlas-based segmentation methods. Foremost, the required atlas-to-subject registration can introduce misalignment artefacts that make for a fuzzy prior at best, and a plain wrong one at worst. Multi-atlas and label-fusion approaches may help in this regard. Secondly, the robustness of atlas-guided tractography to pathology is in question, as registration in the presence of (tumourous) lesions is still an open issue. However, we argue that this issue should be addressed at the level of the registration, and progress is being made in this area [243].

Chapter 5

Population-based atlas construction

The work in this chapter was published in

D. Christiaens *et al.*, "Groupwise deformable registration of fiber track sets using track orientation distributions", in *Computational Diffusion MRI and Brain Connectivity – MICCAI Workshop*, T. Schultz *et al.*, Eds., ser. Mathematics and Visualization, Nagoya, Japan: Springer International Publishing, Sep. 2013, pp. 151–161

and

D. Vercruysse, D. Christiaens, *et al.*, "Fiber bundle segmentation using spectral embedding and supervised learning", in *Computational Diffusion MRI – MICCAI Workshop*, L. O'Donnell, G. Nedjati-Gilani, *et al.*, Eds., ser. Mathematics and Visualization, Cambridge, MA, USA: Springer International Publishing, Sep. 2014, pp. 103–114.

5.1 Introduction

In the previous chapter, we have illustrated the possible benefits of atlas-guided tractography, but also highlighted the dependency of such methods on the availability of a population atlas of the expected track configuration. In addition, such tractography atlases facilitate clustering and labelling of tracks

into anatomical bundles [167, 169, 175] and population-based variability analysis of tractography [244]. However, the success of these methods depends on the quality of the required atlas-to-subject registration and the atlas' level of detail.

In this chapter, we therefore investigate several aspects of atlas construction. A first and crucial step is spatial normalization of individual subject images to atlas space, both between images in the population of which the atlas is built (groupwise registration) and between the resulting atlas and the image to be analyzed (atlas-to-image registration). Although this registration step is typically carried out via the anatomical images of the different subjects, it has been pointed out that direct registration of the extracted tractograms may be better suited for population-based analysis of the track configuration [244, 245], as the matching criterion is directly related to the structures of interest. In Section 5.2, we therefore introduce a novel method for non-rigid track set registration, applicable in both atlas-to-subject and groupwise registration and fully diffeomorphic. This registration method is well suited to construct track orientation atlases as used in Section 4.2 and generally applicable for labelled tractography atlases too.

In Section 5.3, we assume that all subject data is already aligned in a common atlas space and discuss the topic of fibre bundle segmentation, i.e., labelling individual tracks as part of anatomical WM structures. While this is often done manually, (semi-)automated approaches have been described in literature, either based on predefined anatomical regions-of-interest (ROI) or on clustering strategies [163]. ROI-based approaches have high specificity and reproducibility but low sensitivity, whereas clustering techniques are sensitive but not specific. In Section 5.3, we introduce a hybrid method that combines advantages of both and demonstrate its use in bundle segmentation of individual subjects. This technique can help neuroanatomy experts to segment and label WM bundles in large track sets and define labelled tractography atlases.

5.2 Groupwise diffeomorphic track set registration

Current methods for non-rigid track-based registration (e.g., [244, 246, 247]) require a pre-existing segmentation of WM bundles. Registration of unsegmented, full-brain tractography data has, to our knowledge, been limited to affine transformations [245, 248, 249]. Moreover, the effectiveness of these methods has only been demonstrated for deterministic, DTI-based tractography. Secondly, many of these methods are based on distance measures between a compact set of sample tracks [245, 249], feature points [247] or "fibre modes" [248], and thereby neglect part of the information contained in dense

track sets. A notable exception is the metric on currents [244], in which the distance is defined based on the spatial distribution of the mean local track direction. In regions of crossings or track dispersion, however, this mean track direction is ill-defined.

In this work, we examine the use of an image-domain representation of the spatial and angular distribution of full-brain track sets for deformable registration and atlas construction. In contrast to the current state-of-the-art, our method does not depend on a pre-existing bundle segmentation and is able to handle crossings and dispersion. We evaluate our method on artificially deformed data of a single subject (known ground-truth) and on HARDI-based probabilistic tractography data of 15 normal subjects, and compare the results to image registration methods based on the fractional anisotropy (FA) and the fibre orientation distribution (FOD).

5.2.1 Methods

Track Orientation Distribution

Our main idea is to represent the tractogram as a probability distribution function (PDF) in the image domain, rather than a set of individual tracks (samples from this distribution). One example of such representation is the map resulting from track-density imaging (TDI) [250], in which the intensity of each voxel is determined by the number of tracks that cross that voxel. TDI was later generalized to incorporate angular information as well [221]. As such, a full spatio-angular PDF of the tractogram is obtained, named the track orientation distribution (TOD).

Suppose each track t that crosses a voxel $\mathbf{r}$ is linearly parametrized by ε according to the length along the track, and ε_1 and ε_2 are the values of this parametrization at the voxel boundaries. The TOD in that voxel is a function in $\mathbf{u} \in \mathbb{S}^2$ and is formally defined as

$$\mathrm{TOD}(\mathbf{r}, \mathbf{u}) = \sum_t \int_{\varepsilon_1}^{\varepsilon_2} \frac{\tilde{\delta}_{\mathbf{z}_t(\varepsilon)}(\mathbf{u})}{\varepsilon_2 - \varepsilon_1} \, \mathrm{d}\varepsilon \ , \tag{5.1}$$

where $\mathbf{z}_t(\varepsilon)$ is the local direction of t at position ε and $\tilde{\delta}_{\mathbf{z}_t(\varepsilon)}(\mathbf{u})$ is the apodized point spread function (PSF) oriented along this direction. The apodized PSF [113] is the closest strictly-positive approximation of a Dirac δ-function in the spherical harmonics (SH) basis [60] of order $\ell_{\max}$, as shown in blue in Fig. 5.1. Hence, each track additively contributes to the TOD in a voxel by averaging the apodized PSF along its intersecting part (through integration and normalization).

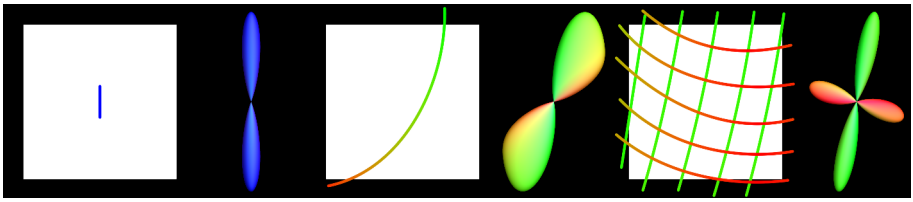

Figure 5.1: Illustration of the track orientation distribution of SH order 16 for 3 different track configurations: a single line segment (*left*), a curved track (*middle*) and a crossing of 2 fibre track bundles (*right*).

Note that the TOD in Fig. 5.1 resembles the fibre orientation distribution (FOD) [91], but while they are of similar qualitative nature, they have an entirely different meaning [221]. The FOD estimates the local fibre distribution from DWI data, whereas the TOD is a direct representation of *any* given tractogram, as generated by a given algorithm. Hence, the TOD incorporates more global information, while the FOD is directly related to the DWI data in a single voxel.

TOD registration and reorientation

The TODs of N different subjects are represented as images of their coefficients in the SH basis of order $\ell_{\max} = 4$. As such, the track set registration problem is redefined as a more convenient image registration problem. Inspired by existing work on FOD registration [251], we minimize the sum of squared differences (SSD) between all pairs of transformed TOD coefficients. By Parseval's theorem for spherical harmonics, this corresponds to minimizing the squared amplitude difference between the transformed TODs, integrated over $\mathbb{S}^2$.

In this study, we use the diffeomorphic demons algorithm [252], adapted for groupwise, multi-channel registration as in [253]. The SSD is minimized between the corresponding TOD coefficients $c_i[k]$ and $c_i[j]$ of all subject pairs $[k, j]$ by calculating the symmetric demons forces

$$\mathbf{F}_i[k,j] = -\frac{(c_i[k] - c_i[j])\,(\nabla c_i[k] + \nabla c_i[j])/2}{\|(\nabla c_i[k] + \nabla c_i[j])/2\|^2 + (c_i[k] - c_i[j])^2/(2\eta)^2} \quad , \tag{5.2}$$

where η is the maximum step size. The total pairwise force $\mathbf{F}[k,j]$ is the (weighted) average of all channels, and the final force acting on subject k is defined as the average force exerted by all other subjects, i.e.,

$$\mathbf{F}[k] = \frac{1}{N-1} \sum_{\substack{j=1 \\ j \neq k}}^{N} \sum_{i} w_i \, \mathbf{F}_i[k,j] \quad . \tag{5.3}$$

The weights w_i are defined such that the total weight of all coefficients of every order ℓ is the same, i.e., the 0th order coefficient has weight $\frac{1}{3}$, the 5 coefficients of order 2 each have weight $\frac{1}{5 \cdot 3}$ and the 9 4th order coefficients have weight $\frac{1}{9 \cdot 3}$. In our experience, these weights improve the robustness of the registration against challenging initialization. Note that as $\mathbf{F}[k,j] = -\mathbf{F}[j,k]$, $N\,(N-1)/2$ pairwise force fields need to be computed. The algorithm proceeds as in [252]: fluid regularization is applied by smoothing the total force field; the exponential of this update field is composed with the total deformation field; and finally diffusion regularization is applied by smoothing the total deformation field.

After each iteration, the TOD in every voxel is reoriented by applying the method of D. Raffelt *et al.* [239]. To this end, the TOD is decomposed into a mixture of apodized PSFs along equally distributed directions and reoriented by rotating and recomposing each of these PSFs, based on the Jacobian of the local deformation. In terms of computation time, reorienting the TOD is much more efficient than recomputing the TOD of the transformed tracks, especially for large track sets.

5.2.2 Experiments and results

Data, processing and fibre tracking

HARDI images of $N = 15$ healthy subjects were acquired with a Siemens 3T system, using a twice-refocussed spin-echo sequence and an isotropic voxel size of 2.5 mm. For each subject, DW images in 75 uniformly distributed gradient directions at $b = 2800\,\mathrm{s/mm^2}$ and 10 non-DW images ($b = 0\,\mathrm{s/mm^2}$) were acquired. Using MRtrix [124], we obtained the FODs of SH order 8 with constrained spherical deconvolution [91] and computed 2 million tracks for each subject using probabilistic streamline tracking with uniform seeding in a full brain mask, step size 0.2 mm, minimum curvature radius 1 mm, FOD amplitude cutoff 0.1, and minimum track length 10 mm.

Experiment 1: Synthetically deformed single subject

In this first experiment, we aim to evaluate our registration method on tractography data of multiple deformed copies of a single subject with known anatomical correspondences. Therefore, we randomly selected 1 subject in the group, and warped and reoriented its FODs onto each of the 14 other subjects according to the deformation fields obtained from groupwise demons registration of b0, FA and MD channels [253]. As such, we obtained 14 synthetic images and ground-truth deformation fields between each pair. We then generated fibre tracks in each of these images individually and computed the TODs. By deforming the FOD images, instead of the tractography data, this setup allows to test the algorithm's robustness against inter-subject differences in seeding and track density.

We ran the proposed registration method on the 14 synthetic TOD images using a multi-scale strategy. The registration starts with maximum step size η and regularization kernel widths σ_{fluid} and σ_{diff} all equal to 5.0 mm, then proceeds at 2.5 mm and finally at 1.25 mm, with 500 iterations at each scale. In our experience, this is sufficient to ensure convergence. The resulting deformation fields and their inverse were composed in order to obtain all pairwise deformation fields. The accuracy of the registration is assessed by computing maps of the Euclidean distance between these deformations and their corresponding ground-truth. The mean of the distance maps of deformations that map onto the same subject then provides a measure of the registration accuracy of that subject.

In addition, we compared to the accuracy of direct image registration by performing the same groupwise demons algorithm with identical parameter settings on the FA (single channel) and on the FOD coefficients (cutoff at $\ell_{\max} = 4$) of the 14 synthetic images. For comparability, all distance maps (defined in the space of the different images) are warped to the *original* atlas space, i.e., the atlas that was used to generate the synthetic data and the ground-truth deformations. As such, we can average all distance maps across subjects and properly compare FA, FOD and TOD as features for registration.

Figure 5.2 shows these maps of the averaged deformation distance, masked to the full brain. The figures suggest that the accuracy of FA and FOD registration is relatively uniform across the brain, while TOD registration achieves a higher accuracy in dense white matter yet lower in the frontal lobe and the distal gyri. The box plots in the bottom row of Fig. 5.2 confirm this observation: the median registration error in the full brain mask is 2.52 mm for FA registration, 2.55 mm for FOD registration, and 2.45 mm for TOD registration, but the variability of the TOD registration error is larger. If we define a WM mask by thresholding

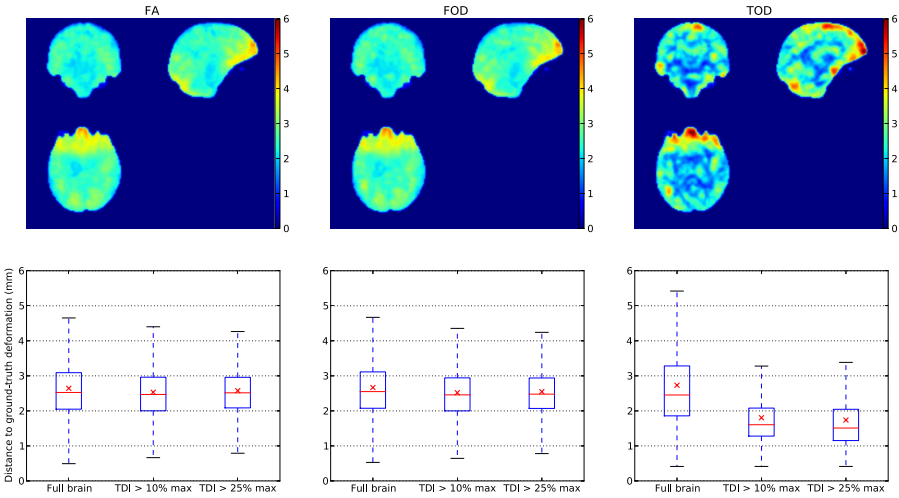

Figure 5.2: Results of Experiment 1. Euclidean distance between inter-subject deformation fields and their ground-truths, for FA (*left*), FOD (*middle*) and TOD (*right*) based registration. The top row shows the deformation errors mapped to a common atlas space. The bottom row shows box plots of the registration error in all voxels in a brain mask, and voxels where the track density is larger than 10% and 25% of the maximum. All box plots represent the 10, 25, 50, 75, and 90 percentiles and mark the mean with a cross.

the TDI map of each subject at 25% of its maximum, the accuracy of FA and FOD registration remains approximately unchanged, while the median error of TOD registration drops to 1.51 mm.

Experiment 2: Multiple subjects

We applied the presented registration method to the track sets of the 15 different subjects, using the same multi-scale setup and the same parameters as in Experiment 1. The outcome is the mean TOD atlas shown in Fig. 5.3, as well as 15 deformation fields that map the subjects onto atlas space. Figure 5.4 shows a subsample of the original, probabilistic track sets of all subjects, and the same tracks warped to atlas space. The results demonstrate that the dense white matter structures are successfully aligned and clearly reflected in the mean TOD atlas. Remaining alignment errors are located in the caudal end of the corticospinal tract, at the interface of WM and cerebrospinal fluid (CSF) in the ventricles, and in the cortical gyri.

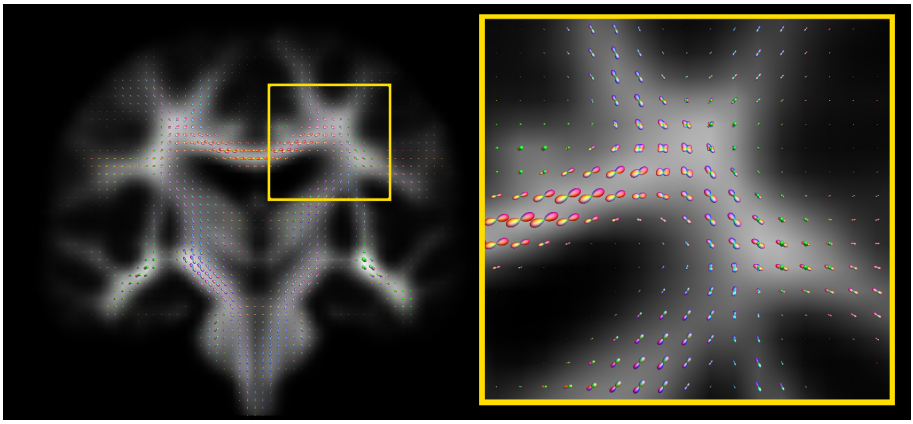

Figure 5.3: Results of Experiment 2. Coronal slice of the mean TOD atlas and a close-up of the crossing of the corpus callosum and the corticospinal tract. The 0th order coefficient of the TOD (the TDI map) is overlaid with spherical plots of the TOD ($\ell_{\max} = 4$) in all voxels.

We repeated this experiment using FA and FOD based registration, like we did in Experiment 1. Next, we use the resulting deformation fields to transform the original tracks of all subjects to the space of each atlas, and recompute the TOD of the transformed tracks at order $\ell_{\max} = 8$. Note that this exceeds the order used for registration, and hence contains more detailed angular information. We then assess the quality of the registration by mapping the angular correlation coefficient of the TOD of all subject pairs. The angular correlation coefficient r_A between 2 SH functions $U(\theta, \phi) = \sum_{i=0}^{n} u_i Y_i(\theta, \phi)$ and $V(\theta, \phi) = \sum_{i=0}^{n} v_i Y_i(\theta, \phi)$ is defined as

$$r_A = \frac{\sum_{i=1}^{n} u_i \cdot v_i}{\sqrt{\sum_{i=1}^{n} u_i^2} \cdot \sqrt{\sum_{i=1}^{n} v_i^2}}, \tag{5.4}$$

and scales between -1 and 1 [89]. The results are displayed in Fig. 5.5, and show that in deep white matter, i.e., in high track density masks, the angular correlation of the TOD atlas is significantly higher than for the FA and FOD atlases.

5.2.3 Discussion

The TOD offers a new solution to the track set registration problem, akin to the use of Gaussian mixture models in point cloud registration. By modelling the (discrete) tractogram as a (continuous) probability distribution, we can

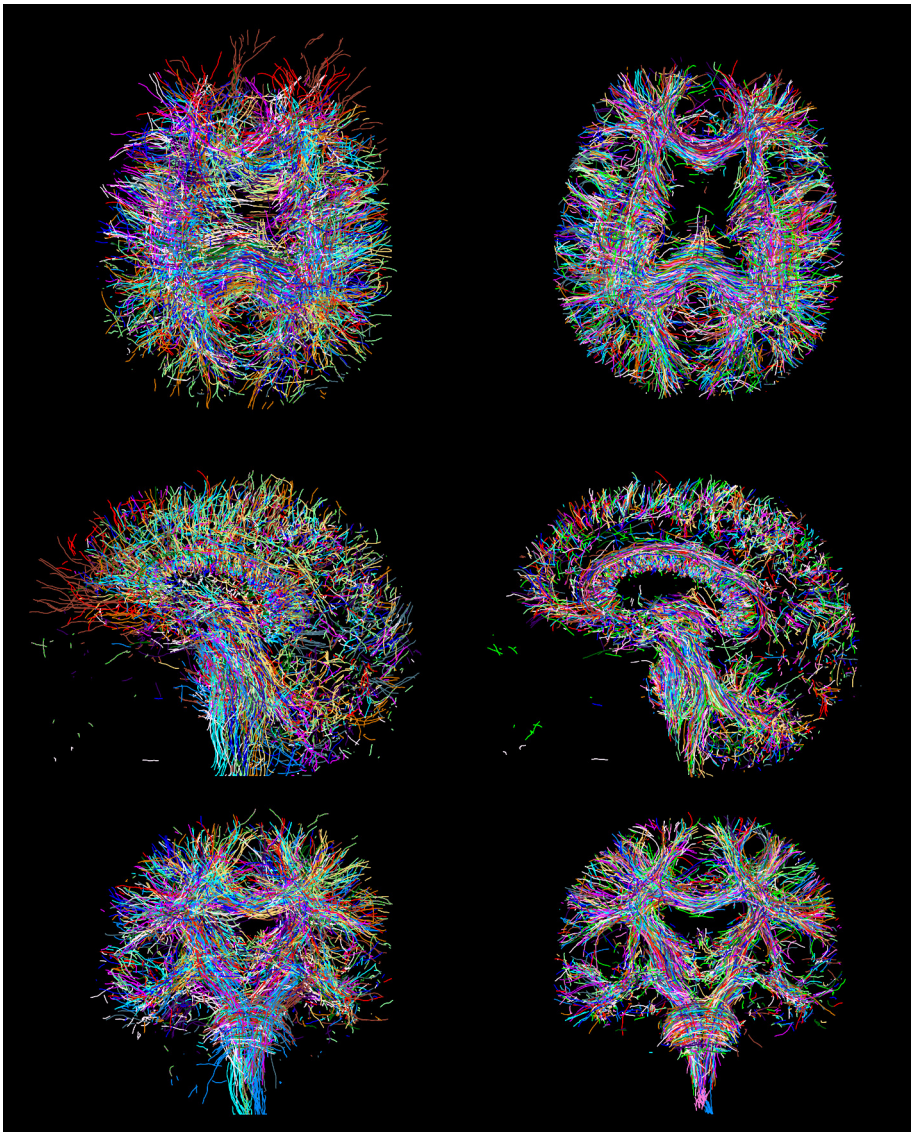

Figure 5.4: Results of Experiment 2. Axial, sagittal and coronal slabs (thickness 7.5 mm) of the subsampled tractograms (1000 tracks) of all subjects before (*left*) and after (*right*) registration. Each subject is represented in a unique colour.

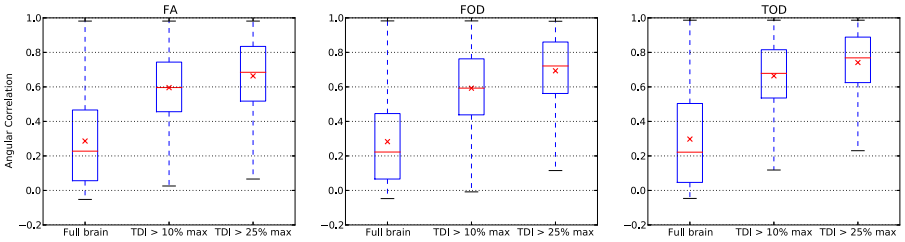

Figure 5.5: Results of Experiment 2. Box plots of the angular correlation coefficient between the TOD (SH order 8) of the transformed tracks, for FA (*left*), FOD (*middle*) and TOD (*right*) based registration. Box plots are shown for all voxels in a brain mask, and for voxels where the track density is larger than 10% and 25% of the maximum. All box plots represent the 10, 25, 50, 75, and 90 percentiles and mark the mean with a cross.

successfully register track sets without relying on correspondences or prior segmentation. This is especially important for the very large (on the order of millions), probabilistic tractography datasets that are increasingly popular.

As opposed to existing track set registration methods, the TOD neglects the long-range *connectivity* information contained in the track set. The TOD, like the FOD, can not discriminate crossing, kissing and fanning configurations. For the purpose of registration, however, this enhances the robustness against spurious tracks. It is precisely because ambiguous FOD configurations often result in false positive tracks, that we wish to exclude long-range information from the matching criterion.

The representational power of the TOD depends on the maximal harmonic order $\ell_{\max}$ of the SH basis, i.e., higher orders allow to model more complex track configurations. However, this high-order information may not contribute much additional information to the matching criterion, especially at the expense of the additional computation time that higher orders impose on the registration and reorientation. We therefore selected $\ell_{\max} = 4$ as a compromise between both. Fig. 5.3 shows that 4th order TODs, while relatively smooth, are sufficient to capture the main directions of crossing bundles.

The experiments show that the presented method can successfully align large probabilistic track sets of 15 subjects. The resulting atlas (Fig. 5.3) models the expected local track configuration. The mean registration accuracy on data with known ground truth is on the order of the voxel size and improves in regions of high track density, i.e., where the TOD contains the most information. We have compared these results to more conventional image registration methods based on the FA and the FOD, as registration of the underlying DWI data is

currently the only alternative to non-rigid alignment of probabilistic track sets. Figure 5.2 shows that the registration accuracy in the FA and FOD atlas is homogeneous over the whole brain and of the same order as the accuracy of TOD registration. However, the misalignment errors of the TOD registration are localized to regions where the tractogram is sparse (e.g., in the frontal lobe, where magnetic field homogeneities are known to affect the reconstruction). With a track density threshold as low as 10% of the maximum, the TOD registration significantly outperforms image registration (t-test, $p < 0.01$).

With respect to DWI registration in general, the improved quality of the registration in white matter is promising for group analysis of WM-targeted pathologies, although we must stress that the robustness of our method against pathological data has not yet been evaluated. In addition, the sensitivity of TOD registration to the tracking algorithm and its parameters should be investigated prior to such analysis, but this goes beyond the scope of this work.

Several potential improvements remain to be explored. For one, the current similarity measure, i.e., SSD on the TOD coefficients, is sensitive to track density differences and might therefore cause misalignment errors. Entropy- or correlation-based similarity metrics might perform better in that respect. Moreover, similar to the approach taken in D. Raffelt *et al.* [251] for FOD registration, the current set-up applies reorientation after each iteration, but ignores it in the calculation of the diffeomorphic update field. Accounting for SH reorientation in the optimization is a daunting task and has, to the best of our knowledge, only been done in the LDDMM framework [254]. However, it could lead to faster convergence and more accurate registration, particularly in the distal gyri. Secondly, as the TOD can be represented on an arbitrary voxel grid, future work may investigate if the registration can benefit from a multi-resolution optimization scheme. Finally, as suggested by Siless *et al.* [255], T1-weighted images can provide additional contrast in CSF and grey matter, although this requires accurate correction of susceptibility-induced distortion of the DWI data (e.g., using a reverse-phase encoding acquisition protocol [256]). In fact, as the TOD is represented in the image domain, the proposed method is very well suited to be extended with other modalities.

5.3 Fibre bundle segmentation

We introduced fibre bundle segmentation in Section 2.5.5, and discriminated parcellation-based methods and track clustering methods. Parcellation-based methods are well suited for building labelled tractography atlases thanks to their high specificity and reproducibility. While initial strategies were often based on

manually defined ROIs [166, 257], automated approaches based on anatomically defined ROIs in a common atlas space have also been presented [164, 165]. In Section 4.3, we demonstrated the use of such labelled tractography atlases as a label prior in global tractography to reduce false positives, jointly facilitating probabilistic track labelling in individual subjects. Here, we illustrate automated atlas construction by means of the white matter query language (WMQL) [164] and apply the resulting atlas for labelling streamline tractography data using a new, hybrid method based on spectral embedding and supervised learning.

5.3.1 Materials and methods

The proposed method is based on spectral embedding, a dimensionality reduction technique that represents each track as a point in an embedding space such that nearby tracks (provided some distance metric), are mapped onto nearby embedding vectors. O'Donnell and Westin [167] have demonstrated spectral embedding for fibre clustering using unsupervised k-means clustering in the embedding space. Instead, we propose to use supervised learning, specifically support vector machines (SVM) and random forests, on the embedding vectors. The required training data is generated with WMQL labelling.

Materials

Data of 25 healthy subjects were provided by the Human Conectome Project (HCP), WU-Minn consortium [202]. DWI data consists of 3×90 gradient directions at b-values 1000, 2000, and 3000 s/mm^2 and 18 non-diffusion weighted images ($b = 0$), at an isotropic voxel size of 1.25 mm, and was corrected for motion and EPI distortions as described in [214]. The fODF, and subsequent deterministic and probabilistic full-brain tractography (50 000 each), were reconstructed with MRtrix [91] using default parameters. All tracks are warped to MNI space using nonlinear deformation fields provided by the HCP [240, 241]. Data of 20 subjects is used in the training set (atlas), the remaining 5 subjects are used for evaluation.

Parcellation-based labelling

The tracks were segmented into WM bundles based on a structural parcellation of white matter and the cortex provided by the HCP and originally obtained with FreeSurfer [242]. This parcellation-based labelling is automated with the white matter query language (WMQL), which defines queries for fibre bundles based on 1) *anatomical terms* that state if a fibre tract traverses or ends in a

certain anatomical region of the brain, 2) *relative position terms* that state if a tract lies, for instance, lateral or frontal of a certain anatomical structure such as the amygdala and 3) *logical operations* that are for example conjunctions, disjunctions or exclusions of the previous two types of terms [164]. As such, neuroanatomy expert knowledge is formalized, thus improving reproducibility. By default, WMQL defines 44 queries for the most prominent WM bundles. Applying these to our tractography data resulted in approximately 4500 labelled tracks for each subject, i.e., about 9 % of all tracks are labelled, the remaining tracks are considered outliers.

Spectral embedding

Spectral embedding is a common dimensionality reduction technique for clustering, in which each track is represented as a point in embedding space based on a certain affinity measure [167]. This representation should preferably cluster data points of high affinity. Assuming that fibres belonging to the same anatomical bundle following a similar trajectory, the pairwise fibre affinity w_{ij} between tracks i and j is defined based on the symmetrized mean closest point (MCP) distance $d_{ij} = d_{ji} = (\mathrm{MCP}_{ij} + \mathrm{MCP}_{ji})/2$ via a Gaussian kernel, i.e., $w_{ij} = \exp\left(-\frac{d_{ij}^2}{\sigma^2}\right)$ where $\sigma = 60\,\mathrm{mm}$ in our experiments. These affinities are computed between all pairs of fibres, resulting in a symmetric affinity matrix $\mathbf{W}$. Based on the Normalized Cuts algorithm by Shi and Malik [258], the embedding vectors are then computed using the eigenvectors $\mathbf{U}$ of the normalized affinity matrix $\mathcal{W} = \mathbf{D}^{-\frac{1}{2}}\,\mathbf{W}\,\mathbf{D}^{-\frac{1}{2}}$, where $\mathbf{D}$ is a diagonal matrix containing the row sums of $\mathbf{W}$. The number of eigenvectors determines the dimension of the embedding space [167] and is fixed to $e = 25$ in our experiments.

In practice, the entire affinity matrix is too large to compute. Therefore, as described in Fowlkes *et al.* [259], its eigenvectors are approximated using the Nyström method. Instead of calculating all pairwise fibre affinities, a random subset of tracks is chosen (containing an equal amount of fibre trajectories from each subject) and only the affinities from all subjects to this subset are computed. The layout of the entire affinity matrix is shown in Fig. 5.6. Submatrix $\mathbf{A}$ contains the pairwise affinities between the fibres of the subset and $\mathbf{B}$ those of the rest of the fibres to the subset. The largest submatrix $\mathbf{C}$ is not calculated, considerably reducing the computation time. In our experiments, submatrix $\mathbf{A}$ contains a random sample of 4000 tracks.

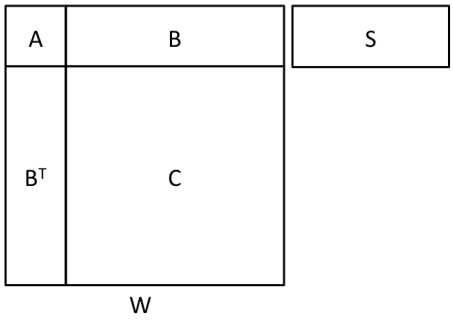

Figure 5.6: Block structure of the normalized affinity matrix $\mathcal{W}$, used in the Nyström method. The regions in submatrices **A** and **B** denote the individual subjects. Submatrix **C** represents the part that does not need to be calculated when using the Nyström method. For the automatic segmentation of a new subject, matrix **S** contains the affinity values between the new tracks and the subset of matrix **A**. (reproduced from [167])

Note that in order to make a multi-subject atlas, spectral clustering needs to be performed in all subjects together. Therefore, registration to a common space is required, such as the normalization to MNI space used in this experiment. As such, the fibres of all subjects are treated as if they originate from one brain for training, which results in one embedding space.

Supervised classification

We propose to cluster the embedding vectors into anatomically relevant bundles using supervised machine learning techniques, assuming the the assigned WMQL labels as ground truth. We compare three classifiers: linear support vector machines (SVM) [260], SVMs with a Gaussian radial basis function (RBF) kernel and a forest of extremely randomized decision trees (ExtraTrees) [261, 262]. 5-fold cross-validation is used to avoid overfitting.

As such, a white matter atlas is created which can be used for the automatic segmentation of fibre bundles from novel subjects. First, the new tracks must be registered or transformed to the atlas (MNI) space. Secondly, the affinity between the tracks of the new subject and the atlas is calculated. As illustrated in Fig. 5.6, a matrix **S** is calculated that contains the affinity values between the new tracks and the subset of tracks used for calculating **A**. Note that **S** also has to be normalized [167]. Next, each new fibre will be embedded in the same

Table 5.1: Total accuracy of the multi-label classification problem for deterministic and probabilistic streamline tractography. In both cases, accuracy improves when using supervised techniques. The best classifier performance is obtained with support vector machines (SVM) with a Gaussian RBF kernel.

	deterministic	probabilistic
k-means ($k = 200$)	83.41 %	80.84 %
linear SVM	94.90 %	93.75 %
RBF-SVM	95.78 %	95.63 %
ExtraTrees	95.07 %	94.77 %

embedding space as created for the original clustering, as outlined in O'Donnell and Westin [167]. The final step is to predict classifier labels based on these new embedding vectors.

5.3.2 Results

Accuracy in labelled tracks

The proposed method is evaluated in the 5 test subjects. First, we evaluate the accuracy of the predicted labels for all tracks that have been segmented by WMQL, assuming their WMQL labels as ground truth. Accuracy is defined as the total number of correctly classified tracks divided by the total number of tracks. The results are compared to k-means clustering in the embedding space using 200 clusters and assigning labels based on majority voting, identical to O'Donnell and Westin [167]. The total accuracy of each classifiers and tractography method is listed in Table 5.1.

Results show that the accuracy of the supervised methods is largely in the same range around 95 %, strongly outperforming unsupervised k-means clustering with accuracy below 85 %. The SVM classifier with Gaussian RBF kernel achieved highest performance, and in all algorithms deterministic tractography data are more easily labelled than their probabilistic counterparts. Performance evaluation across individual bundles showed that the results are in the same range for most bundles, except for three bundles that contain little to no tracks in the training set.

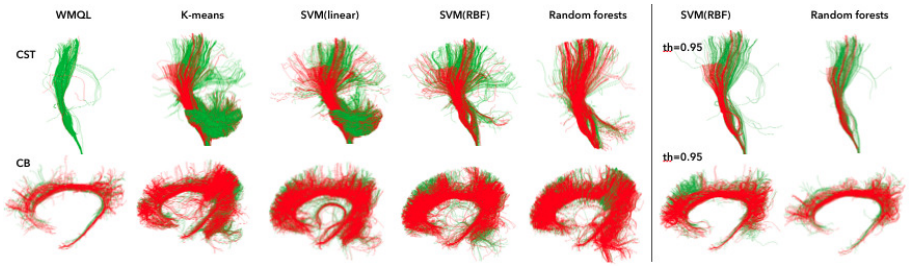

Figure 5.7: Segmentation results on deterministic, whole brain tractography data, using the white matter query language (WMQL), k-means clustering, support vector classifiers (SVM) with linear and Gaussian RBF kernels, and random forests, shown for the corticospinal tract (CST) and the cingulum bundle (CB). The effect of a label probability threshold above 95 % is shown on the right.

Qualitative results in unlabelled tracks

When the full-brain track set is used as input, including many spurious tracks (i.e., false positives) and interrupted tracks that were not labelled by the WMQL, it is no longer possible to use the labels generated by the WMQL as ground truth to evaluate classifier accuracy. Therefore, the results can only be analyzed visually by comparing the resulting segmentation with the WMQL output bundles, and with neuroanatomical expert knowledge.

First, the results are studied without considering the label probability, i.e., using maximum-likelihood classification. This is shown in the left panel of Fig. 5.7 for deterministic tractography in a single subject. The top row shows the segmentation of the corticospinal tract (CST). Notice the misclassified cerebellar tracks, which are not defined in the WMQL queries, in the k-means and linear SVM segmentation. Additionally, all classifiers label sagittal dispersions in the corona radiata as CST. The segmentation of the cingulum bundle (CB) contains misclassified tracks of the fornix, also unlabelled in WMQL, and dispersing tracks from the corpus callosum (CC).

When the label probabilities of the RBF-SVM and ExtraTrees classifiers are thresholded above 95 %, part of these outlier tracks are excluded from the result. As shown on the right in Fig. 5.7, imposing such threshold excludes the corona radiata tracks from the CST segmentation. In addition, note that the cut off tracks of the left CST bundle (red) are still correctly labelled, in contrast to the WMQL segmentation. The CB segmentation contains less dispersions into the CC with a high threshold and the tracks from the fornix are also eliminated.

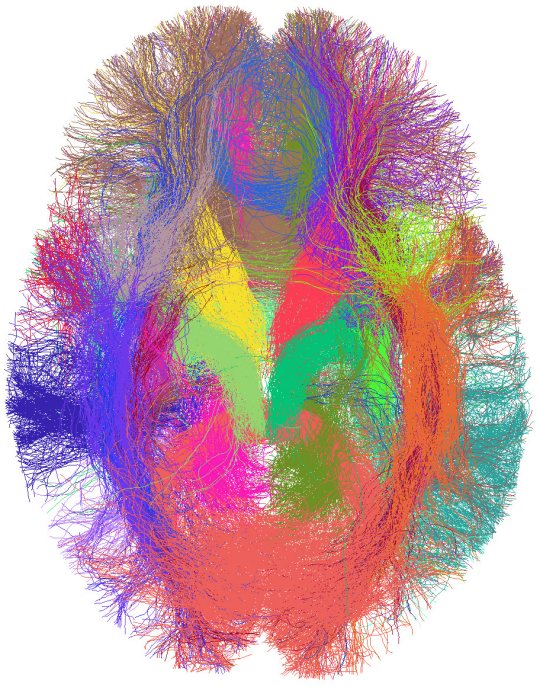

Figure 5.8: Axial slab of the full brain tractogram in a single subject, with all tracks coloured according to their WM bundle label for probability $> 95\,\%$.

The resulting bundel segmentation and outlier rejection at $p > 95\,\%$ of a full brain probabilistic tractogram in a single subject is depicted in Fig. 5.8. This result, possibly averaged across a population, may serve as labelled tractography atlas in which the probability threshold can be used to modify the confidence level of the segmentation.

5.3.3 Discussion

With this experiment, we illustrated the use of an automated, parcellation-based labelling approach to create tractography atlases across a population of subjects and adopted its output as ground truth training data for bundle segmentation in test subjects. However, it is clear that this ground truth is prone to false negatives, as for example shown in Fig. 5.7 where WMQL failed to recover the left CST due to an artefact in the deterministic tractography

data. Therefore, such *binary* label assignment may be overly restrictive. In addition, the assumed ground truth is inherently incomplete, as some bundles may remain unsegmented due to artefacts of the tractography algorithm or missing WM queries.

Nevertheless, we successfully applied this imperfect ground truth as training data in our experiments, facilitating *probabilistic* label assignment in full brain tractography. We demonstrated that the predicted labelling outperforms state-of-the-art clustering techniques and qualitatively improves WM bundle segmentation when using a label probability threshold. Setting this threshold effectively creates a virtual outlier class that eliminates spurious tracks, although optimizing its value remains a topic of future work.

Ultimately, this method can be used for building probabilistic labelled tractography atlases. The remaining challenges and requirements are first and foremost to complement the training data with queries for missing fibre bundles such as the fornix. In addition, future work may explore hierarchical decompositions that could include small WM bundles and substructures.

5.4 Conclusion

This chapter introduced two methods for building tractography atlases from population data. First, we presented a novel method for deformable registration of fibre track sets. Rather than comparing individual fibres, we seek to optimize the similarity between the TODs, spatio-angular probability distributions of the full-brain track configuration, of all subjects. Our method does not require track correspondences or prior bundle segmentation, is robust against interrupted and spurious tracks, and is able to handle crossings and probabilistic tractography data. The resulting population atlas is well suited as local track orientation prior in global tractography as introduced in Section 4.2. In addition, the groupwise registration method is applicable in track clustering methods [167, 169, 175] as it avoids bias towards the underlying DWI data. Indeed, the results indicate that direct registration of the tractograms outperforms conventional image registration methods in dense white matter. While these experiments were conducted on streamline tractography data, the method is directly applicable to global tractography data as well.

Secondly, we presented an automated strategy for creating labelled tractography atlases based on an anatomical parcellation and reproducible bundle *queries*, and demonstrated its use in segmenting streamline fibre bundles. The initial atlas is based on a binary segmentation, and even though it is adopted as ground truth in the subsequent classifier training, this initial segmentation may contain

false negatives due to tractography or registration artefacts. Our proposed approach facilitates probabilistic bundle segmentation instead, which learns the expected bundle patterns across the population. Quantitative and qualitative results indicated increased sensitivity, while the label probability still enables outlier exclusion.

In future work, both contributions can be employed to improve the atlas priors discussed in Chapter 4. Spatial normalization is essential in all atlas-based methods and therefore highly relevant to both local and global priors. Yet the common TOD representation of the groupwise registration framework in Section 5.2 directly complements the local atlas prior in Section 4.2. This may ultimately enable to integrate both contributions into a joint framework, iteratively updating a groupwise tractography-based atlas and atlas-based tractography in all subjects. The global label prior in Section 4.3 additionally requires probabilistic track labels in atlas space, which our contributions of Section 5.3 can provide. The main area of future improvement is to incorporate WM bundles that are currently missing from the initial WMQL labelling into the atlas.

Chapter 6

Nonnegative factorization of diffusion-weighted images

The work in this chapter was published in

D. Christiaens *et al.*, "Convex non-negative spherical factorization of multi-shell diffusion-weighted images", in *Medical Image Computing and Computer-Assisted Intervention – MICCAI 2015*, N. Navab *et al.*, Eds., ser. Lecture Notes in Computer Science, vol. 9349, Munich, Germany: Springer International Publishing, Oct. 2015, pp. 166–173

and is currently in revision as an extended journal article.

6.1 Introduction

Diffusion-weighted imaging (DWI) is a non-invasive magnetic resonance imaging technique with the unique ability to probe tissue microstructure in vivo, by measuring its hinderance to water diffusion [12]. The water diffusion process is sensitive to the cellular structure of the surrounding tissue, in particular the presence of cell membranes and intracellular organelles [15]. DWI is applied in both neuroscientific research and clinical practice, for studying brain organization, detecting pathology, and measuring disease progression.

The DWI signal can be represented in many ways, including the spherical harmonics (SH) basis [59] and the cumulant expansion [53] of which diffusion tensor imaging (DTI) [33] is a special case. Parameters such as fractional

anisotropy (FA) introduced in the context of such signal representations, are sensitive to changes in the underlying tissue microstructure. However, their interpretation at the cellular level is less straightforward.

In an effort to provide more specific measures, a myriad of models have been introduced that relate the measured signal to neural tissue structure. These models typically decompose the diffusion signal into cellular compartments, such as intra- and extra-axonal space or free water [72], weighted by their respective volume fractions. Similarly, nonnegativity-constrained spherical deconvolution (CSD) adopts a single fibre compartment of fixed anisotropy, the fibre response function (RF), which contributes linearly and independently to the DWI signal across all fibre orientations in the voxel [88, 91]. Deconvolution then facilitates estimating the orientation distribution function (ODF) of fibres in that voxel, a metric of apparent fibre density (AFD) in white matter [113, 117]. CSD was later extended to multi-tissue (MT-)CSD [118], which incorporates partial voluming with adjacent tissues that are not adequately modelled by the fibre response function [109, 110]. Each tissue compartment is then characterized by a fixed response function, assumed to be known a priori.

The work in this chapter generalizes MT-CSD to a blind source separation problem, akin to nonnegative matrix factorization (NMF). NMF decomposes each input vector as a nonnegative linear combination of unknown source vectors. Similarly, our approach expands the diffusion signal in a basis of response functions, adapted to the tissue structure and to the DWI data at hand. The resulting components can be associated to known tissues, and generalize to certain types of pathology. As such, our method strikes a balance between signal representation and tissue modelling: it seeks a decomposition that closely represents the data, subject to minimal constraints that give structural interpretation to the component basis functions.

In addition, this method addresses a very practical problem regarding multi-tissue CSD, namely estimating response functions from the data at hand. Originally, white matter (WM) fibre response functions were fitted to the DWI data in a single-fibre mask of high FA, after reorientation of the diffusion tensor eigenvectors [88, 91]. Alternative recursive approaches have been introduced, which segment single-fibre voxels and reorient the data based on the peaks of the fODFs iteratively [92, 93], or which calibrate the kernel anisotropy in each voxel separately under sparsity constraints [104]. However, these techniques do not directly generalize to other tissue types, such as grey matter (GM) and cerebrospinal fluid (CSF). Current literature therefore relies on tissue segmentation of T_1-weighted images (T1) to define GM and CSF kernels, which requires the T1 to be aligned to the DWI data [118]. As this is rarely the case in practice, direct DWI tissue segmentation methods have been introduced independently and simultaneously, based on sparsity-constrained NMF [263] or

convexity-constrained NMF [23, Appendix A] of the isotropic mean DWI signal per shell. These methods circumvent T1 requirement and are thus applicable in any reference frame without external input, but still rely on the diffusion tensor model for reorienting the DWI data in each single-fibre voxel. Here, we account for the full anisotropy of the DWI signal by extending NMF to convolution in spherical harmonics.

In related work, Xie *et al.* [264] applied NMF to single-shell diffusion tensor data. Reisert *et al.* [265] have introduced a more general dictionary learning method that imposes sparsity on the tissue ODFs. In contrast to their approach, we do not impose any constraints on the ODFs except for nonnegativity. Instead, we constrain the tissue RFs to be convex combinations of the data voxels. As such, physical plausibility of the tissue responses is ensured in a purely data-driven manner.

Extending our previous conference paper [27], we made improvements to the initialization, the optimization, and the convergence criterion, improving the overall performance and speed of the algorithm. The accuracy and precision of our convexity- and nonnegativity-constrained spherical factorization (CNSF) technique are evaluated in Monte Carlo simulations at various noise levels. In addition, we include results on healthy brain data, both in vivo and ex vivo, and in the presence of pathology, and show that the decomposition can be associated to known anatomy.

6.2 Method

6.2.1 Multi-tissue spherical convolution

As explained in Section 2.4.3, multi-tissue spherical convolution [91, 118] assumes linear partial volume effect (PVE) to decompose the DWI signal into N tissue components, each of which is the spherical convolution of a response function (RF) and an orientation distribution function (ODF). The response function is an axially symmetric function $H_{t,b}(\theta)$ that is constant for each component t and that characterizes the signal anisotropy and attenuation across b-values. The ODF $F_t(\theta, \phi)$ is a nonnegative function on the sphere that determines the local directionality and density of that particular component in the voxel. As such, the diffusion signal $S_b(\mathbf{g})$ in each voxel, for gradient direction $\mathbf{g}$ and given b-value, becomes

$$S_b(\mathbf{g}) \approx \sum_{t=1}^{N} (H_{t,b} * F_t)(\mathbf{g}) \quad . \tag{6.1}$$

All functions are commonly represented in the basis of real, symmetric spherical harmonics (SH) of maximum order $\ell_{\max}$ [90, 91, 118]. As such, the convolution reduces to a multiplication of the coefficients of corresponding order ℓ, i.e., $s_b(\ell, m) = \sum_t \sqrt{\frac{4\pi}{2\ell+1}} h_{t,b}(\ell)\, f_t(\ell, m)$ with $\ell \in \{0, 2, \ldots, \ell_{\max}\}$ and $m \in [-\ell, \ell]$. The response functions are axially-symmetric, and therefore constrained to the spherical harmonics of phase $m = 0$, known as zonal harmonics (ZH).

For this work, we structure the SH coefficients of the DWI signal in tensor $\bar{S}$, indexed by the voxel v and shell b, and rewrite (6.1) as

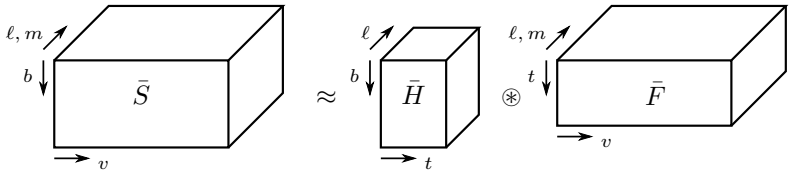

. (6.2)

In this equation, $\bar{H}$ contains the ZH coefficients of the response functions, indexed by component t and shell b. $\bar{F}$ contains the SH coefficients of the ODFs, indexed by voxel v and component t. The operator $\circledast$ is introduced to denote spherical convolution in the SH basis, and corresponds to the matrix product of every slice $F_{\cdot,\cdot,(\ell,m)}$ with slice $H_{\cdot,\cdot,\ell}$ of corresponding order ℓ. Note that the $\ell = 0$ coefficients of $\bar{F}$ represent the isotropic volume fraction or density of each tissue.

6.2.2 Convexity- and nonnegativity-constrained spherical factorization

Considering both the response functions $\bar{H}$ and the ODFs $\bar{F}$ as unknown, expression (6.2) can be seen as a blind source separation problem akin to nonnegative matrix factorization (NMF), in which a data matrix is decomposed as the product of a source matrix and a nonnegative weight matrix [176, 266, 267]. In this case, the unknown sources are the response functions of separate components, the weights are the associated ODFs, and we aim to find

$$\bar{H}^\star, \bar{F}^\star = \arg\min_{(\bar{H},\bar{F})} \|\bar{S} - \bar{H} \circledast \bar{F}\|_F^2 \tag{6.3}$$

$$\text{s.t. } A\,\mathbf{f}_{v,t,\cdot} \geq 0 \quad .$$

The matrix A evaluates the SH basis across a dense set of directions, to impose nonnegativity of the estimated ODFs denoted by vector slices $\mathbf{f}_{v,t,\cdot}$. The vector $\mathbf{f}_{v,t,\cdot}$ thus contains the ODF SH coefficients at index (v,t). The only parameters in this framework are the number of components N and the maximal harmonic order $\ell_{\max}$ of each component.

However, the solution to (6.3) is not unique. As illustrated in Fig. 6.1, the response functions $\bar{H}$ span a N-gonal *simplicial* cone in the high-dimensional data space, radiating outwards from the origin $\mathbf{0}$. Only voxels "within" this cone are represented exactly; data points "outside" this cone give rise to the residual under minimization in (6.3). As such, any combination of RFs that envelops all observed data points gives rise to a zero residual, but may not necessarily be physically meaningful. Therefore, we impose a convexity constraint [232], which ensures that all sources H_t are a convex combination of the measured signal after reorientation. In other words, the convexity constraint ensures that all response functions are observed in the data, typically in voxels with low PVE in both spatial and angular domains. The RFs are thus represented as a contracted tensor-matrix product along the dimension of voxels v:

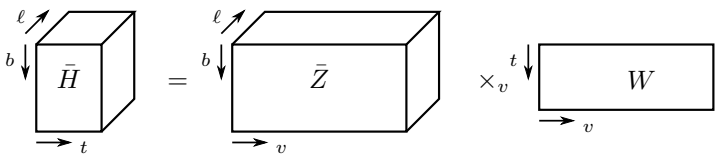

, (6.4)

such that each coefficient $h_{t,b,\ell} = \mathbf{z}_{\cdot,b,\ell} \cdot \mathbf{w}_{t,\cdot}$ with voxel weights $W \geq 0$ and $\|\mathbf{w}_{t,\cdot}\|_1 = 1$. The auxiliary tensor $\bar{Z}$ contains the coefficients of the best fitting zonal harmonics to the data $\bar{S}$, across all possible orientations of a symmetry axis. These best fitting zonal harmonics are precomputed in each voxel, by reorienting the signal such that axis (θ, ϕ) coincides with the z-axis and evaluating the residual as the energy across coefficients of phase $m \neq 0$. This residual is an antipodally symmetric function on the sphere, and its minimum is selected with an exhaustive search across a dense set of directions. For a corpus callosum voxel, the result typically resembles a single-fibre white matter response function. For voxels in grey matter or CSF regions, the best fitting zonal harmonic is more isotropic.

6.2.3 Optimization

The resulting factorization problem is computed iteratively, alternately solving for $\bar{F}$ given $\bar{H}$, and for $\bar{H}$ – implicitly represented by W – given $\bar{F}$. This procedure is initialized with k-means and repeated until convergence.

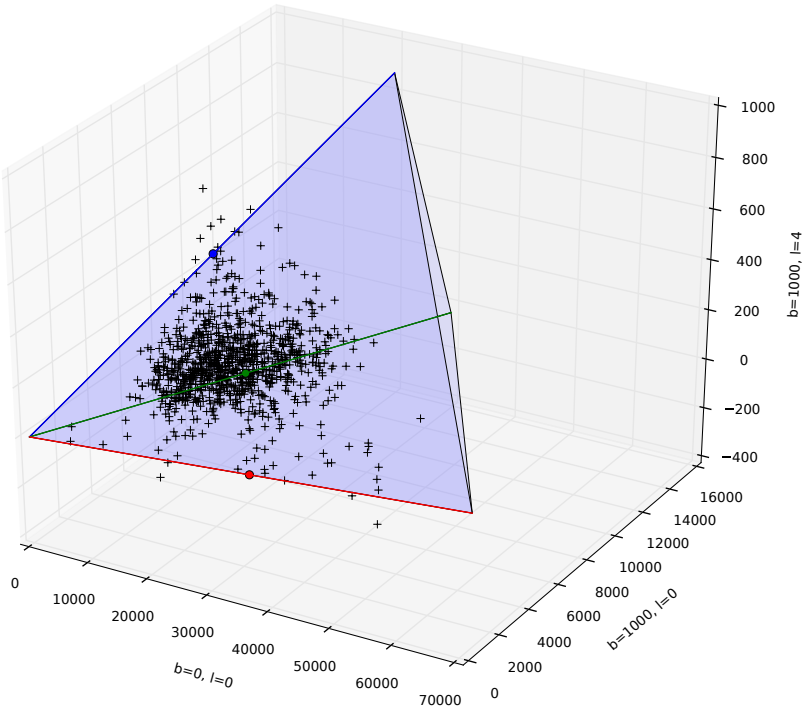

Figure 6.1: Illustration of the simplicial cone spanned by 3 response functions (RF) shown in red, green, and blue, and projected into a 3-dimensional subspace. The best fitting zonal harmonic in each voxel is similarly depicted in this subspace in black. Data points scattered within the simplicial cone are exactly represented as nonnegative combinations of the RFs. Data points outside this cone can not be represented exactly and give rise to a residual fitting error. The convexity constraint ensures that all RFs are convex combinations of the data points, i.e., located within the point cloud itself and typically driven towards its extremes throughout optimization.

Initialization The response functions $\bar{H}$ are initialized with *spherical* k-means clustering of the best-fitting zonal harmonics $\bar{Z}$. Spherical k-means [268] is identical to the standard k-means algorithm [269], but uses the cosine distance instead of the Euclidian distance between data points. Because of Parseval's theorem in spherical harmonics, this metric minimizes intra-cluster covariance. The initialization is therefore independent of scaling effects, similar to any nonnegative factorization method. Moreover, this k-means initialization obeys the convexity constraint: there exists a $W^{(0)}$ for which the initialization $\bar{H}^{(0)} = \bar{Z} \times_v W^{(0)}$.

In addition, the initialization is adapted to N response functions of given $\ell_{\max}$ each, by projecting all centroids to the appropriate subspace in each k-means iteration. The appropriate subspace is chosen by selecting the permutation of centroids that minimizes the projection residual. Finally, since k-means itself is randomly initialized, the entire procedure is repeated 10 times to ensure robustness, and the result of minimal residual is selected.

Solve for $\bar{F}^{(k)}$ Given response functions $\bar{H}^{(k)}$, the tissue ODFs become

$$\bar{F}^{(k)} = \arg\min_{\bar{F}} \|\bar{S} - \bar{H}^{(k)} \circledast \bar{F}\|_F^2 \tag{6.5}$$

$$\text{s.t. } A\,\mathbf{f}_{v,t,\cdot} \geq 0 \quad .$$

When unfolding all tensors along the dimensions of shells and SH coefficients, this results in a constrained least squares problem for every voxel v. This minimization problem is solved with quadratic programming (QP) subject to non-negativity constraints on $\bar{F}$. Expression (6.5) is identical to multi-shell multi-tissue spherical deconvolution [118].

Solve for $\bar{H}^{(k+1)}$ Subsequently, given ODFs $\bar{F}^{(k)}$, the new response functions become

$$W^{(k+1)} = \arg\min_{W} \|\bar{S} - (\bar{Z} \times_v W) \circledast \bar{F}^{(k)}\|_F^2 \tag{6.6}$$

$$\text{s.t. } W \geq 0$$

$$\|\mathbf{w}_{t,\cdot}\|_1 = 1 \quad .$$

This expression is cast as one global constrained least squares problem, by unfolding all tensors across voxels, shells, and SH coefficients. The optimal RF weights W are then computed with QP, using an interior point method initialized with the solution of the previous iteration.

Convergence The alternating least squares optimization procedure is repeated until the residual $r^{(k)} = \|\bar{S} - \bar{H}^{(k)} \circledast \bar{F}^{(k)}\|_F^2$ converges to a stable minimum. The convergence criterion is met when the relative decrease in residual $(r^{(k)} - r^{(k+1)})/r^{(k)}$ is smaller than a threshold $\epsilon = 0.5\%$.

6.2.4 Implementation

The procedure was implemented in Python, using custom code for evaluating the SH basis and CVXOPT [270] for QP optimization. Each shell is weighted by its number of gradient directions, in order to equalize their respective noise levels. For practical purposes, the iterative procedure is run on a subset of 1000 voxels, randomly selected across a brain mask after applying a 3-pass erosion filter. Afterwards, the ODFs are computed for the entire image based on the resulting RFs $\bar{H}^\star$ in a single run of minimization problem 6.5.

6.3 Validation

6.3.1 Phantom simulation

The accuracy and precision of the proposed technique are evaluated in a simulated phantom, consisting of 3 components with geometry shown in Fig. 6.2. Component 1 mimics anisotropic WM, represented at $\ell_{\max} = 8$. Components 2 and 3 mimic GM and CSF respectively, both simulated as isotropic tissues at $\ell_{\max} = 0$. DWI data are subsequently simulated with ground-truth RFs, originally estimated from in vivo data.

1. The phantom geometry is generated on a 100×100 voxel grid. WM fibre ODFs are simulated by adding Dirac-δ functions in the SH basis.
2. Noise-free DWI data is simulated with forward convolution according to (6.1). The resulting DWI data is the subsampled to a 20×20 voxel grid to induce partial voluming.
3. The DWI signal is then sampled with a uniform gradient scheme adapted to multi-shell data [271]. This scheme contains 150 gradient directions: 5 unweighted images ($b = 0$), 20 diffusion-weighted images at $b = 1000\,\mathrm{s/mm^2}$, 45 images at $b = 2000\,\mathrm{s/mm^2}$, and 80 images at $b = 3000\,\mathrm{s/mm^2}$.
4. Finally, Rician noise is added to all data, for signal-to-noise ratios (SNR) ranging from 5 to ∞. SNR is defined w.r.t. the mean $b = 0$ intensity of WM.

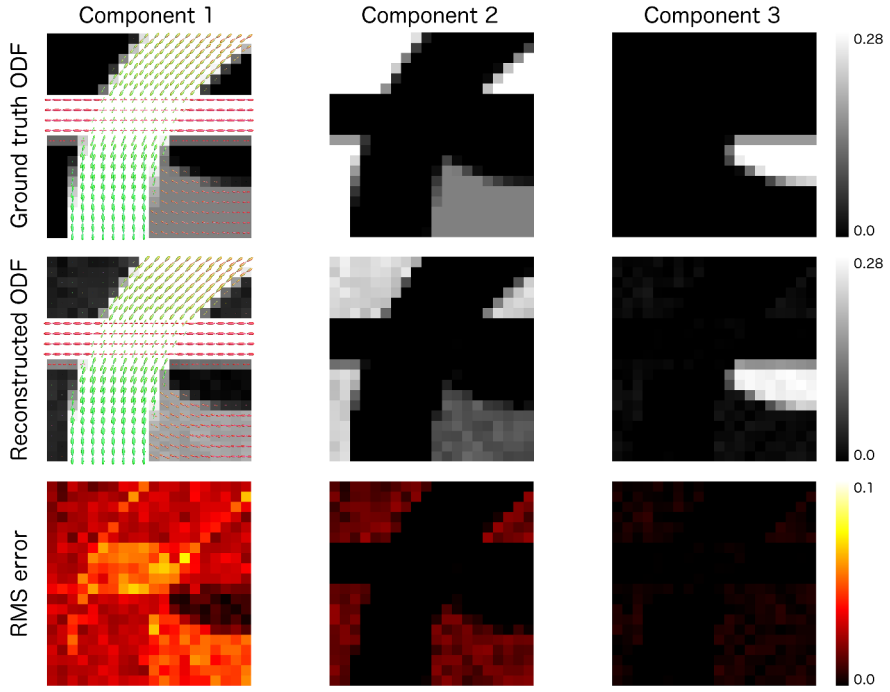

Figure 6.2: Simulated phantom dataset. Top row: ground-truth tissue ODFs of simulated WM, GM, and CSF components. Middle row: ODFs obtained with the presented factorization method at SNR = 20. Bottom row: root-mean-squared error between estimated and ground-truth ODFs.

6.3.2 Accuracy and precision

Applying the proposed method, each noisy realization of the phantom is factorized in 3 components, one at $\ell_{\max} = 8$ and two at $\ell_{\max} = 0$. In Fig. 6.2, the resulting tissue ODFs in one such realization at SNR 20 are illustrated and compared to the ground truth, after convolution of the latter with apodized point spread functions to remove negative side lobes [239]. Their difference is measured with the root-mean-squared (RMS) value $E_{\text{rms}}(f) = \sqrt{\int_{\mathbb{S}_2} f^2(\theta,\phi)\mathrm{d}\Omega} = \|\mathbf{f}\|_2/\sqrt{4\pi}$ of spherical function $f(\theta,\phi)$ with SH coefficients $\mathbf{f}$, where the second identity follows from Parseval's theorem. Fig. 6.2 shows that all components are successfully recovered, including the orientational structure in component 1. The RMS error is highest in the anisotropic component, particularly in regions of partial voluming, and lowest in component 3.

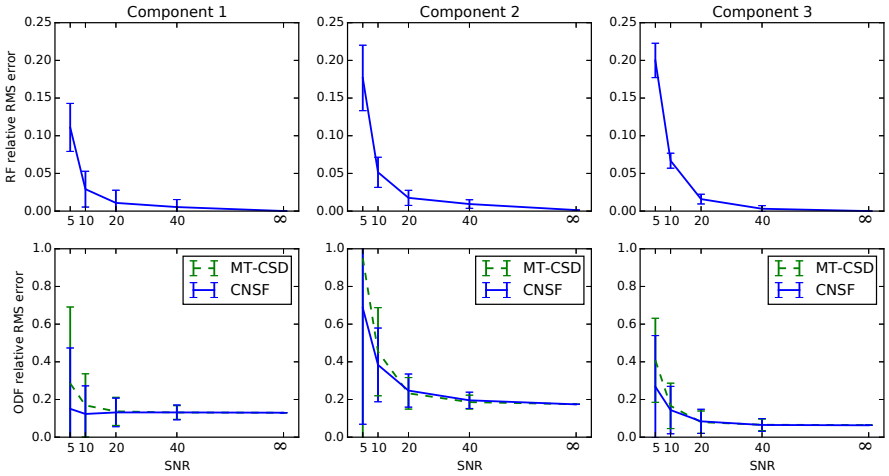

Figure 6.3: Accuracy ± precision of the estimated RFs (top) and ODFs (bottom) in Monte-Carlo simulations (blue lines). The ODF is compared to direct MT-CSD with the ground truth RFs (green dashed lines).

Accuracy and precision of CNSF are measured by repeating this procedure across 100 noise instances at each given SNR. Accuracy of each RF and ODF is defined as the RMS error between the mean result of all noise realizations and the ground truth, relative to the RMS value of the ground truth itself. Precision is defined as the mean RMS error between each RF or ODF and its mean across noise instances, relative to the RMS value of that mean RF or ODF. In addition, direct MT-CSD with the ground truth RFs is applied in all noise simulations, and similarly compared to the ground truth ODFs. The results are plotted in Fig. 6.3, and show that accuracy and precision improve with increasing SNR. The relative RMS error of all RFs reduces to zero at SNR $= \infty$. The ODF error is never entirely eliminated due to the nonnegativity constraint, but does converge to the same accuracy of MT-CSD. Notably, the accuracy of CNSF outperforms MT-CSD in the low-SNR range. Their precision is in the same range. This indicates that CNSF adapts the estimated RF to the Rician noise distribution.

6.4 Data and results

6.4.1 Data and preprocessing

Dataset 1 Data of a neurologically healthy subject were provided by the WU-Minn Human Connectome Project (HCP) [202]. The diffusion data consist of 3×90 gradient directions at b-values 1000, 2000, and 3000 s/mm^2 and 18 non-diffusion-weighted images ($b = 0$), at an isotropic voxel size of 1.25 mm, and was corrected for motion, eddy current, and EPI distortions [214]. In addition, a T1 of isotropic voxel size 0.7 mm is available in the same reference frame. All data are corrected for intensity inhomogeneity using the T1 bias field estimated with FSL FAST [213].

Dataset 2 A multi-shell HARDI dataset of a healthy volunteer was acquired with b-values 700, 1000 and 2800 s/mm^2 along 25, 40 and 75 directions respectively, and 8 $b = 0$ images. In addition, 3 $b = 0$ images were acquired with reverse-phase encoding. The isotropic voxel size equals 2.5 mm, TR = 7800 ms, TE = 90 ms [54]. The diffusion dataset was corrected for motion, eddy current, and EPI distortion using FSL EDDY and TOPUP [215, 272], as well as intensity inhomogeneity with N4 bias field estimation [273]. In addition, a T1 image is acquired at voxel size $1 \times 1 \times 1.2$ mm and rigidly coregistered to the corrected DWI.

Dataset 3 This dataset originates from a patient who suffered a grade IV glioma in the right temporal lobe, and was acquired after tumour resection. The acquisition protocol is identical to that of dataset 2, except for the absence of reverse-phase encoded $b = 0$ images. DWI images are therefore not corrected for EPI distortion and not accurately aligned to T1.

Dataset 4 DWI data of an ex vivo rhesus macaque brain were provided by the Duke Center for In Vivo Microscopy. The original acquisition, described in Calabrese *et al.* [274], consisted of a high-resolution DTI dataset and a HARDI dataset of lower resolution. The former contains 12 DWI volumes at b-value 1500 s/mm^2 and a single $b = 0$ image, at an isotropic voxel size of 130 μm. The latter consists of 30 DWI volumes at $b = 4000$ s/mm^2 and one $b = 0$ image, at an isotropic voxel size of 200 μm. The high-resolution DTI dataset is subsampled to the HARDI resolution after affine registration of their corresponding $b = 0$ images.

6.4.2 Results

First, the presented DWI factorization method is applied to healthy human brain datasets 1 and 2. In line with the validation experiment, we select 3 components: one anisotropic component at $\ell_{\max} = 8$ and two isotropic components at $\ell_{\max} = 0$. In dataset 1, a single run in a subset of 1000 randomly selected voxels took 8 iterations until convergence, or 4 min 59 s on a standard desktop. In dataset 2, a single run took 13 iterations in 3 min 20 s. The precision of the anisotropic RF equals 3.3% in dataset 1 and 5.6% in dataset 2. Hence, this random subsampling enables fast convergence while maintaining sufficient robustness.

The resulting decomposition in RFs and ODFs is shown in Figs. 6.4 and 6.5. Figure 6.4 visualizes the ODFs of all components in the full images. In both datasets, anisotropic component 1 is strongly associated with WM and its ODF lobes are well aligned with the expected fibre structure. Similarly, components 2 and 3 are associated with GM and CSF contrasts. Since both components are imposed isotropic, their ODFs are isotropic volume fraction maps that correspond to the $\ell = 0$ SH coefficient. Note that CNSF produces these components in random order, and we manually sorted them for WM, GM, CSF correspondence. Figure 6.5a-b depicts the resulting RFs, which resemble the anisotropy and attenuation expected of those tissues. Figure 6.5c shows that the residual decreases throughout optimization and converges rapidly. Finally, Fig. 6.5d plots voxel weights W that represent the estimated RFs upon convergence. As shown, these weights evolve to a sparse combination of voxels, consistent with theoretical proof [232].

Next, we compare the results to MT-CSD as implemented in MRtrix3[1] [124]. A single-fibre WM RF and isotropic GM and CSF RFs are estimated from the DWI data based on a T1 tissue segmentation as described in Jeurissen *et al.* [118]. The WM single-fibre mask is obtained with an iterative procedure based on Tournier *et al.* [92]. These WM, GM, and CSF response functions are depicted in dashed lines in Fig. 6.5. As shown, the RFs estimated with CNSF exhibit similar attenuation across b-values, up to a scaling factor. The anisotropic RF of component 1 closely resembles the WM RF when rescaled to equalize their $b = 0$ shells. In addition, Fig. 6.5c shows that the residual of CNSF upon convergence is smaller than the residual of MT-CSD, indicating that a better fit of the data is obtained. In Figures 6.6 and 6.7, the ODF of component 1 is compared to the WM fibre ODF obtained with MT-CSD. Both are qualitatively very similar, showing fibre structure and partial voluming

[1] J-D Tournier, Brain Research Institute, Melbourne, Australia, https://github.com/MRtrix3/mrtrix3

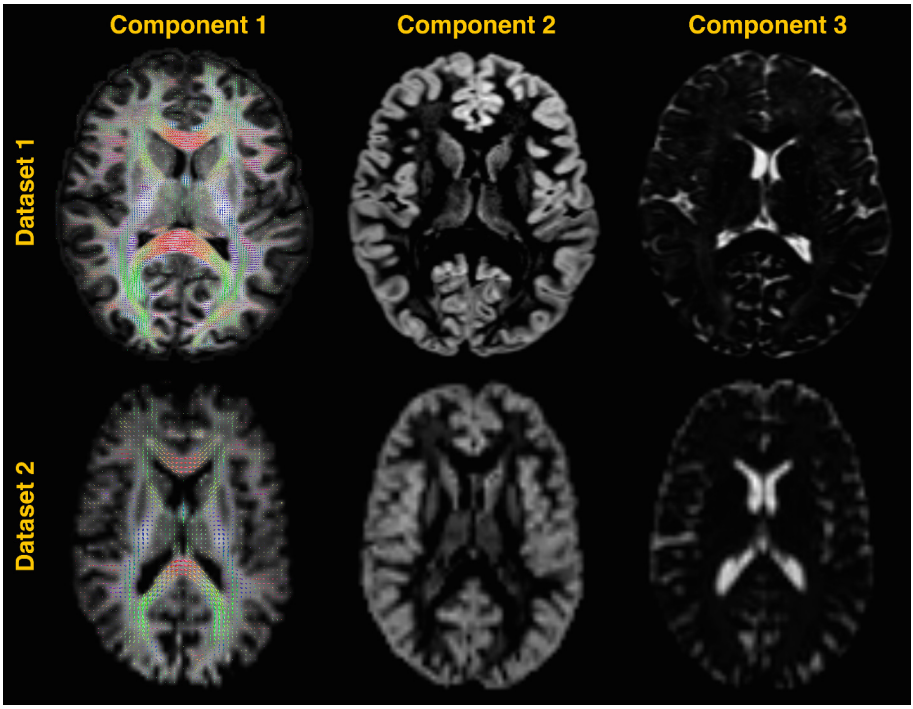

Figure 6.4: Factorization results with 3 components in healthy human brain datasets 1 and 2: Axial slices of the orientation distribution function (ODF) of each component. ODF 1 includes directional information associated with white matter fibre structure, ODF 2 and 3 are isotropic and are associated with GM, and CSF volume fractions.

with adjacent tissue types. Therefore, the proposed DWI factorization method enables the benefits of multi-tissue deconvolution, without relying on T1 or external inputs.

In dataset 3, which contains residual edema, a decomposition in 4 components was chosen, 3 of which are constrained to isotropic RFs. As can be seen in Figs. 6.8 and 6.9, the anisotropic component is again associated with WM, whereas the first isotropic components is associated with GM and the second one with CSF. Notice how this component detects CSF in the surgical cavity, as well as in the ventricles. The third isotropic component is associated with edema in the area surrounding the resected tumour. As shown in Fig. 6.9, the WM fibre ODF detected in component 1 traverses this region homogeneously. While

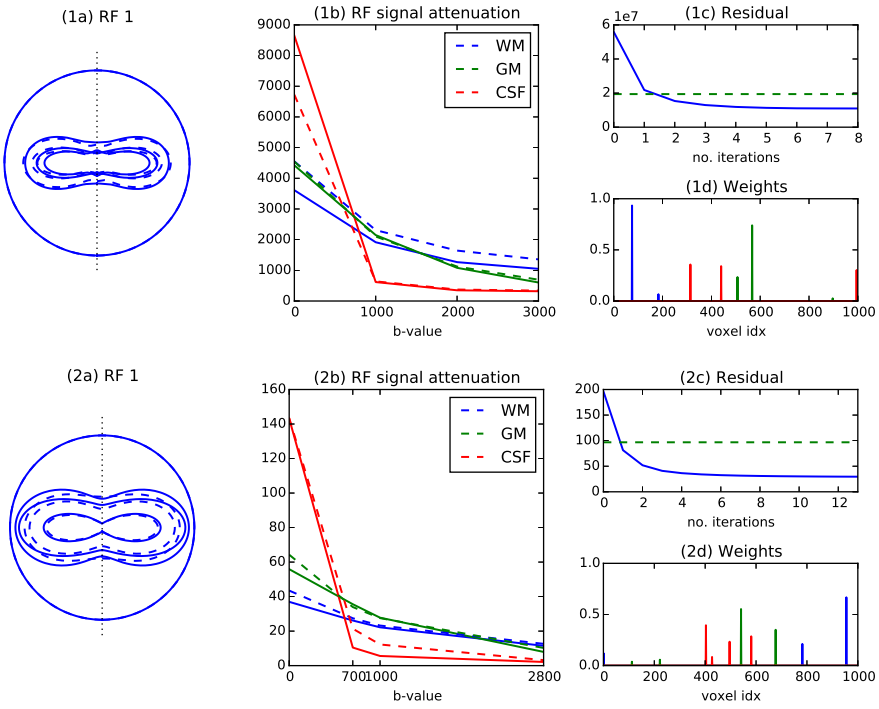

Figure 6.5: Factorization results with 3 components in dataset 1 (top) and in dataset 2 (bottom). (a) The anisotropic response function (RF) of component 1 (full lines) compared to the WM SF response (dashed lines) after equalizing their $b = 0$ amplitudes. (b) The RF attenuation across shells (full), compared to WM, GM, and CSF response functions (dashed). (c) The residual throughout optimization (blue curve), compared to the residual of MT-CSD (green dashed level). (d) Voxel weights encoding the estimated RFs.

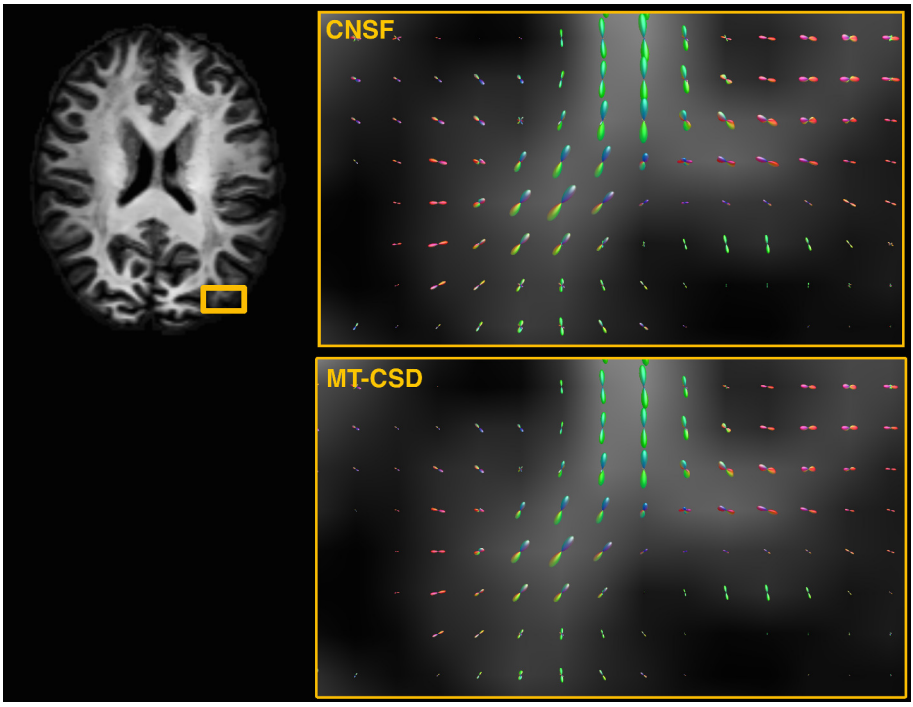

Figure 6.6: The ODF of the anisotropic CNSF component in dataset 1, compared to the white matter fibre ODF obtained with multi-tissue CSD. A close-up of the WM-GM interface shows fibres running through the gyrus and protruding into cortical grey matter. In both cases, explicit modelling of partial volume contamination produces a clean result with little spurious fibre directions.

CNSF is not directly intended for lesion segmentation, this result illustrates how an unsupervised approach can discriminate pathology and adapt to outliers in abnormal data.

Finally, the ex vivo brain in dataset 4 contains little CSF. As shown in Figs. 6.10 and 6.11, factorization into two components produces ODFs associated with WM and GM. At the exceptional spatial resolution in this dataset, multi-tissue decomposition reveals WM fibres traversing distal gyri and protruding into cortical GM. For example, Fig. 6.12 shows ODF 1 in a coronal slice of the temporal lobe, overlaid onto the volume fraction of component 2. Similarly, Fig. 6.13 shows ODF 1 in the cerebellum, and reveals a tree-like branching fibre structure.

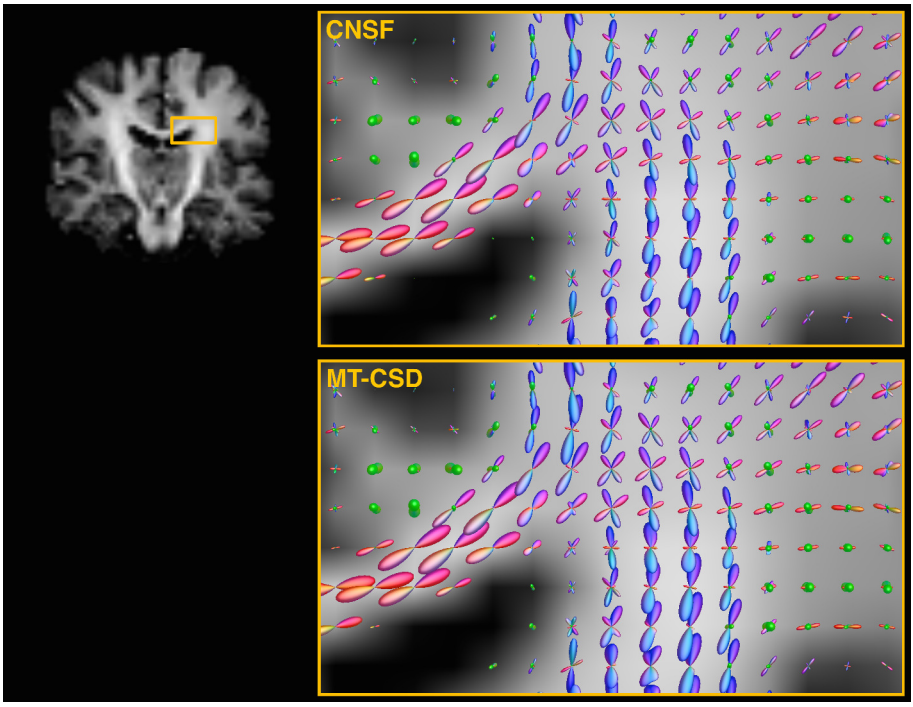

Figure 6.7: The ODF of the anisotropic CNSF component in dataset 2, compared to the white matter fibre ODF obtained with multi-tissue CSD. A close-up of the semioval centre shows that unsupervised CNSF factorization recovers intra-voxel fibre crossings highly similar to results of supervised MT-CSD deconvolution. In the ventricles and at the WM-CSF interface, little partial volume contamination is observed.

6.5 Discussion

6.5.1 Unsupervised DWI factorization

As a direct extension of convex nonnegative matrix factorization [232] to spherical data, CNSF is an unsupervised method: it aims to discover structure in the data, without additional input. The data is represented in a generative model predicated on two minimal assumptions. First, CNSF assumes linear partial voluming between a set of tissue components, each represented by a

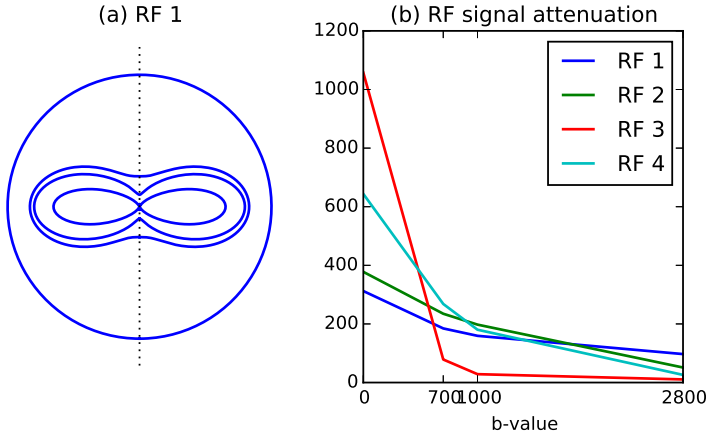

Figure 6.8: Response functions of 4 factorization components in dataset 3, one anisotropic component (RF 1) and three isotropic components (RF 2 – RF 4). RF 1 has the oblate shape characterizing of single-fibre white matter. RF 2 and RF 3 have signal attenuations expected of GM and CSF respectively. Finally, RF 4 has an attenuation profile between CSF and GM, associated with edema.

rotationally-invariant response function. Second, it assumes that these response functions are plausible, i.e., evidence of their existence must be found in the data.

MT-CSD [118] also adopts the first assumption, but additionally assumes that all RFs are known a priori or estimated from the data using a prior tissue segmentation. Therefore, we consider MT-CSD a *supervised* method that estimates tissue ODFs specifically related to the input tissue types. In contrast, CNSF looks for general components that best explain the data under the stated assumptions, fully *unsupervised*. While our results show that in many cases these components are associated with known anatomy, this is never explicitly enforced.

Hence, both methods have a different interpretation and therefore also serve a different purpose. CNSF is primarily suited for exploratory analysis of multi-shell DWI data in which a prior tissue segmentation is unknown or hard to obtain. One example are cases where T1 is unavailable or not perfectly aligned to the DWI data. As demonstrated in datasets 1 and 2, CNSF successfully decomposes the DWI into WM, GM, and CSF-related contrasts, without requiring T1. A second example are cases of pathology, in which the microstructure may be altered to the extent that it is no longer accurately described by a WM-GM-

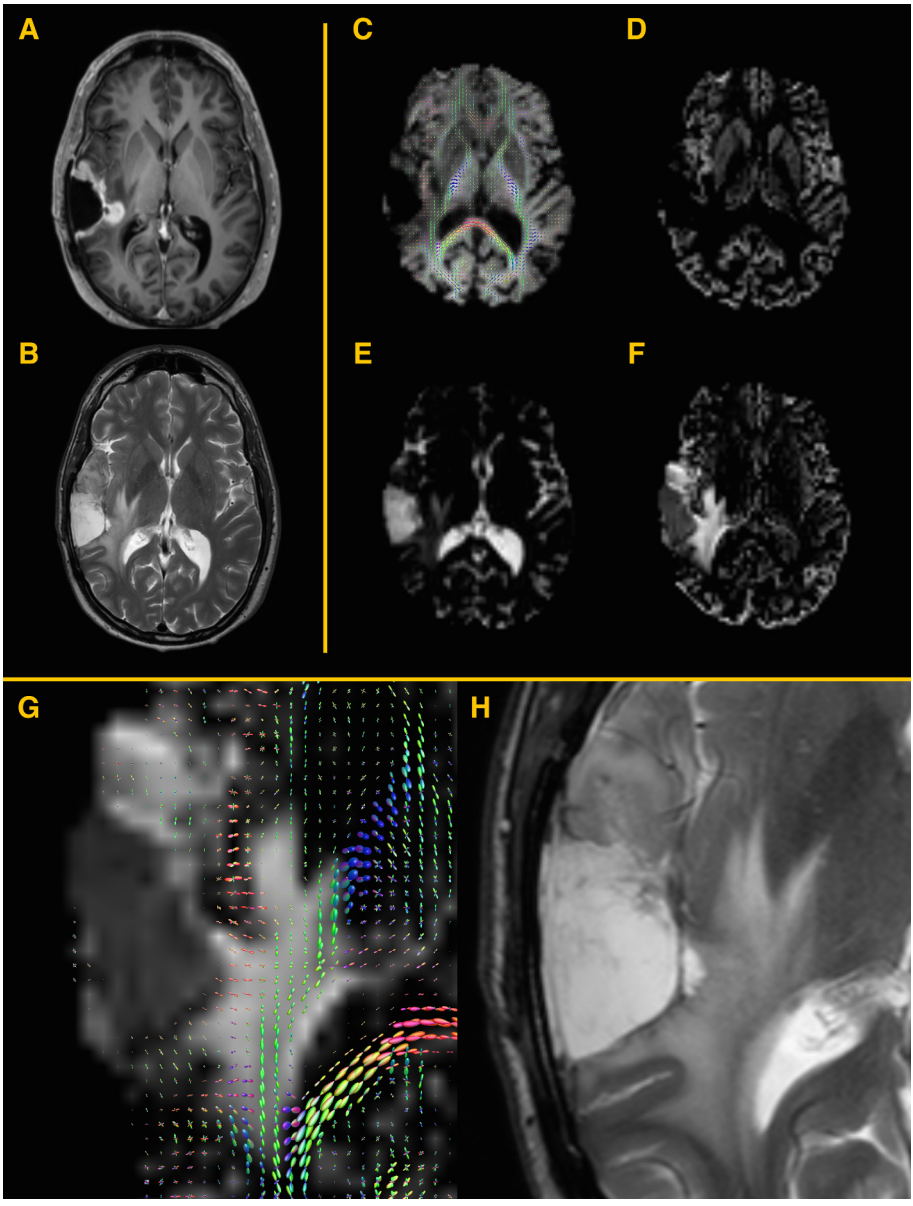

Figure 6.9: (A–B) T_1- and T_2-weighted images of dataset 3, illustrating the resected tumour and residual edema. (C–F) ODFs of components 1–4 obtained with CNSF factorization. ODF 1 recovers white matter fibre orientation. ODF 2 is associated with grey matter. ODF 3 displays CSF contrast in the ventricles and in the surgical cavity. ODF 4 highlights the edemous region surrounding the resected tumour. (G–H) A close-up of this region in ODF 1, overlaid onto component 4, shows WM fibres traversing the edemous area. A corresponding close-up of the T_2-weighted image is provided for reference.

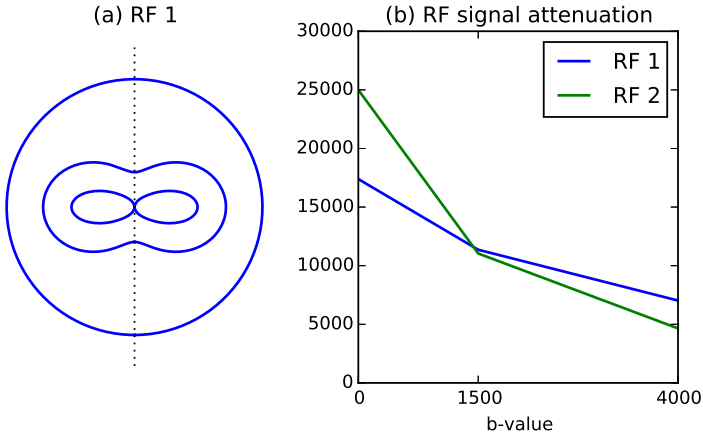

Figure 6.10: Response functions of 2 factorization components in dataset 4, one anisotropic component (RF 1) and one isotropic components (RF 2). RF 1 is asociated with single-fibre white matter. RF 2 is associated with grey matter.

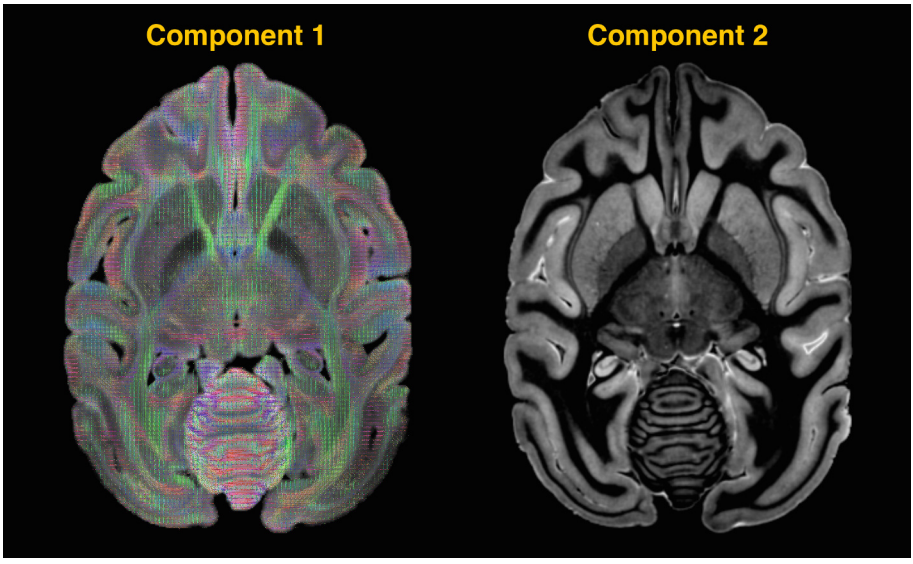

Figure 6.11: Factorization into 2 components in dataset 4. The ODF of anisotropic component 1 is shown on the left, and displays white matter fibre structure. The ODF of isotropic component 2, shown on the right, is primarily associated with grey matter.

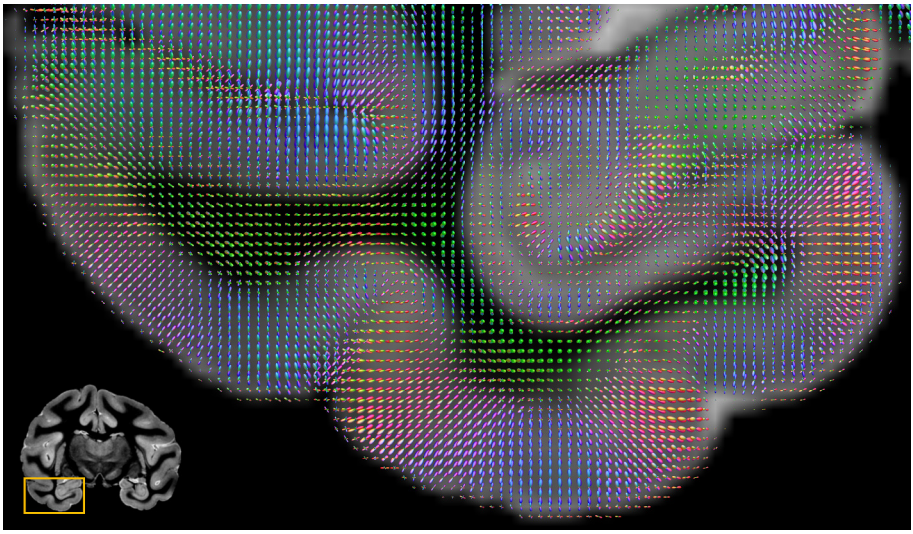

Figure 6.12: Coronal slice of the temporal lobe in dataset 4. The background contrast is the volume fraction of component 2. Overlaid on top is the ODF of component 1. ODF 1 shows longitudinal association fibres traversing white matter and radiating into the grey matter cortex, and recovers anisotropic tissue structure in the hippocampus.

CSF model. In some cases, such as our result of dataset 3, it may therefore be beneficial to include additional components. A third example are in vivo or ex vivo animal data or data of other organs, where the tissue structure differs from human brain. As shown in dataset 4, CNSF may discover structure in such data which is challenging to obtain with existing techniques that assume prior information.

6.5.2 Model selection

The main parameters to select in our approach are the number of components and the SH order $\ell_{\max}$ of each component. In this chapter, we selected one anisotropic ($\ell_{\max} = 8$) and two isotropic ($\ell_{\max} = 0$) components for healthy human brain data, in line with Jeurissen *et al.* [118]. However, in other datasets it may be beneficial to use different settings. The question then arises how one should determine the optimal number of components to use. This problem is generally known as *model selection* or *rank selection*.

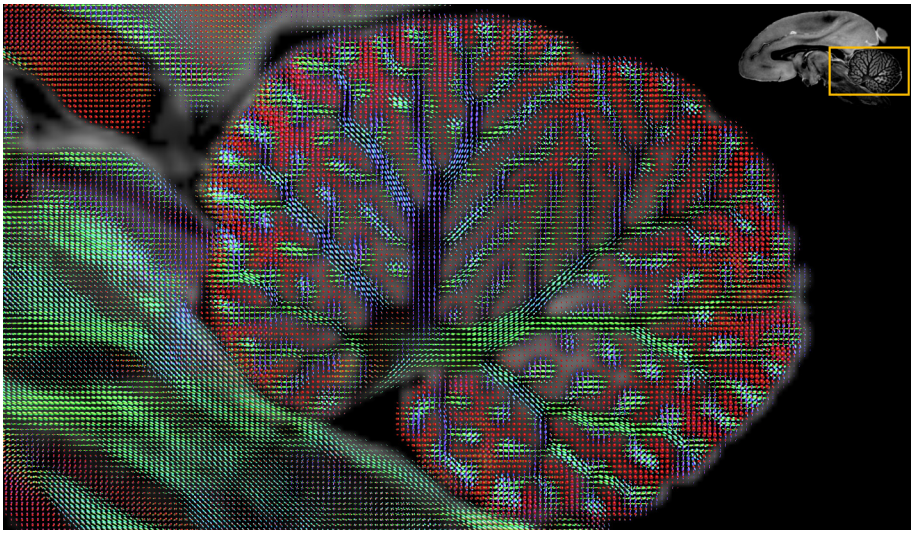

Figure 6.13: Sagittal slice of the cerebellum in dataset 4. The background contrast is the volume fraction of component 2. Overlaid on top is the ODF of component 1, which shows the branching structure of the arbor vitae in cerebellar white matter.

Model selection provides a trade-off between goodness of fit and model complexity. One approach is to use Akaike Information Criterion (AIC) [275] or the Bayesian Information Criterion (BIC) [276] to select such trade-off. Another option is cross-validation [277]. In our previous conference paper [27], we applied BIC to suggest the required number of components (Fig. 6.14). However, different model selection criteria are not always in agreement with each other, and which one to use remains an open question. Therefore, in this work the number of components is selected empirically, based on the nature of the data.

6.5.3 Future perspectives

The presented DWI factorization method lends itself to a number of applications not yet explored in the current work. A first example is factorization of multi-modal data that includes DWI. T_1-weighted, fluid-attenuated inversion recovery (FLAIR), MR spectroscopy metabolite contrasts, or any other scalar image can be included as additional isotropic "shells" in the input tensor $\bar{S}$, provided they are co-registered with the DWI data. Such multi-modal approach may be

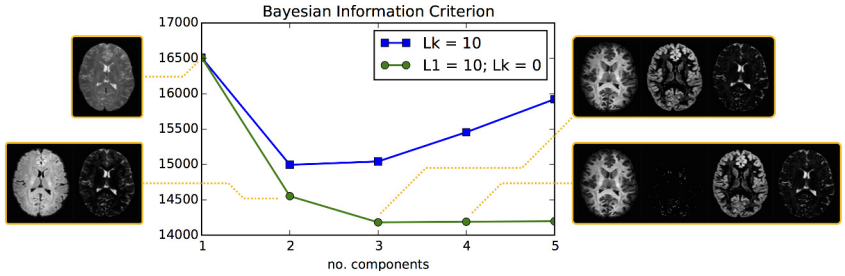

Figure 6.14: Bayesian Information Criterion (BIC) as a function of the model complexity [27]. The blue curve plots the BIC for 1 to 5 anisotropic components of order $\ell_{\max} = 10$, the bottom plot shows the BIC for 1 anisotropic component of order $\ell_{\max} = 10$ and 0 to 4 isotropic components ($\ell_{\max} = 0$).

particularly beneficial for tissue differentiation in pathology, as demonstrated in brain tumours and high-grade gliomas in particular [278–280]. In contrast to those earlier studies, CNSF leverages the full directional nature of the signal and assumes linearity at the level of the acquisition, rather than in derived parameters such as FA. A multi-modal approach may also "augment" single-shell DWI data to facilitate multi-tissue decomposition. Secondly, CNSF can be extended to population studies by including voxels across many subjects in the data tensor $\bar{S}$. As such, the resulting tissue response functions provide an optimal representation of the entire dataset, while the ODFs are quantitatively comparable across subjects. Finally, the presented DWI factorization method may have interesting applications in other organs, such as cardiac tissue or prostate tissue, in which current supervised techniques are not directly applicable.

6.6 Conclusion

This work introduced a generalization of multi-tissue spherical deconvolution as a blind source separation problem, formulated as convex nonnegative factorization in the SH basis. Like CSD, our approach assumes non-negativity of the tissue ODFs and spatial invariance of their RFs, but jointly optimizes the RFs instead of assuming them as known.

Appendix: Multi-modal CNSF with applications in single-shell data

The number of tissue classes is inherently limited by the number of shells (b-values) in the data. A 3-tissue model for healthy human brain thus requires multi-shell data. Yet, in many cases only "single-shell" ($b = 0$ and $b = X$) data is available. Here we augment unsupervised tissue decomposition to multi-modal data. Specifically, we include a T_1-weighted image (T1) in the framework of convexity-constrained non-negative spherical factorization (CNSF) and illustrate its applicability for decomposing single-shell DWI into WM, GM and CSF.

Method

Multi-modal data is incorporated in the decomposition as additional isotropic channels, akin to the $b = 0$ image, under the same assumption of linear partial voluming. As such, the estimated tissue RFs will include the expected T1-intensity. The tissue ODFs remain unchanged, and characterize both density (integral across the sphere) and directional structure. In all experiments, shell weights are set to their respective number of DWI volumes. The T1 is arbitrarily assigned a weight corresponding to 100 DWI volumes.

Results

First, we compare unsupervised tissue decomposition of multi-shell DWI with and without including T1. The RFs, shown in the top and middle rows of Fig. 6.15, are similar and correspond well with the ground-truth RFs, estimated with a MT-CSD. Figure 6.16 shows the ODFs of the estimated tissue components. In both cases, the anisotropic component is associated with WM, two isotropic components are associated with GM and CSF. When including T1, the WM fraction is more sharply delineated, while GM becomes slightly fuzzier. In the ventricles, the CSF component is sensitive to Gibbs-ringing artefacts in the T1.

Secondly, we evaluate 3-tissue decomposition in single-shell DWI, augmented with T1. The RFs are plotted in Fig. 6.15, bottom row. Figure 6.17 shows the reconstructed ODFs in different shells, compared to single-shell CSD [91]. WM, GM, and CSF are effectively separated, even at low b-values. Close-ups of the WM ODF, reconstructed from $b = 2800\,{}^{\mathrm{s}}/_{\mathrm{mm}}$, are shown in Fig. 6.18, and indicate improved handling of partial voluming with respect to single-shell CSD, akin to multi-tissue CSD and CNSF.

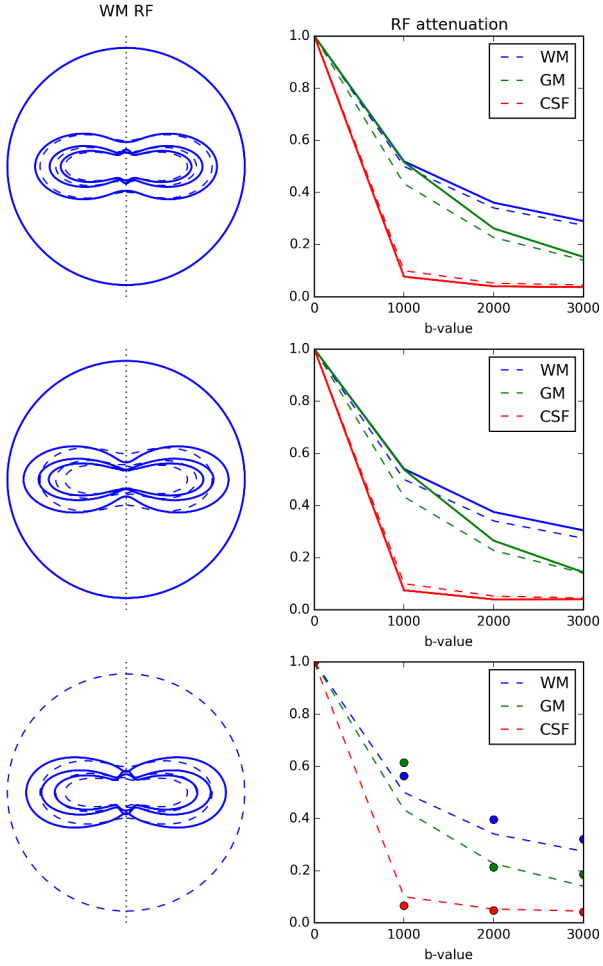

Figure 6.15: Response functions estimated with CNSF in dataset 1, compared to ground truth (dashed lines). Top: multi-shell DWI. Middle: multi-shell DWI + T1 anatomical image. Bottom: single-shell DWI + T1, for each shell separately.

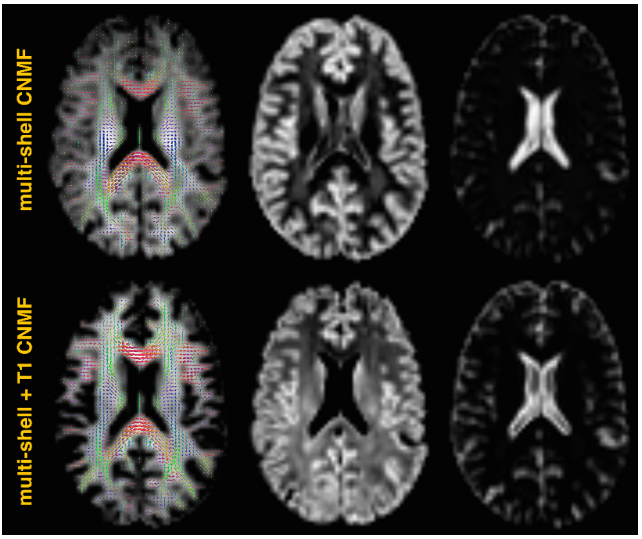

Figure 6.16: Comparison between CNSF of multi-shell DWI with and without T1 anatomical data in dataset 2.

Discussion

Our results show that augmenting single-shell DWI with T1 provides the necessary contrast to discriminate three tissue components, associated with WM, GM, and CSF. While related work has used a T1-segmentation to adapt the CSD response function locally [281], our approach instead finds a set of tissue RFs that explain the data (DWI and T1), without requiring prior segmentation. The comparison with single-shell CSD in Fig. 6.17 shows that even at low b-values, where CSF signal yields large fibre ODFs in the ventricles, our method is able to reconstruct fibre ODFs with no observable CSF contamination. Similarly, Fig. 6.18 illustrates that the multi-tissue decomposition accounts for partial voluming, and ultimately benefits ODF reconstruction and subsequent tractography [23, 118].

Acknowledgements Dataset 1 was provided the Human Connectome Project, WU-Minn Consortium (Principal Investigators: David Van Essen and Kamil Ugurbil; 1U54MH091657) funded by the 16 NIH Institutes and Centers that support the NIH Blueprint for Neuroscience Research; and by the McDonnell Center for Systems Neuroscience at Washington University. Dataset 4 was provided by the Duke Center for In Vivo Microscopy, Durham, NC, USA (an NIH/NIBIB Biomedical Technology Resource Center P41 EB015897).

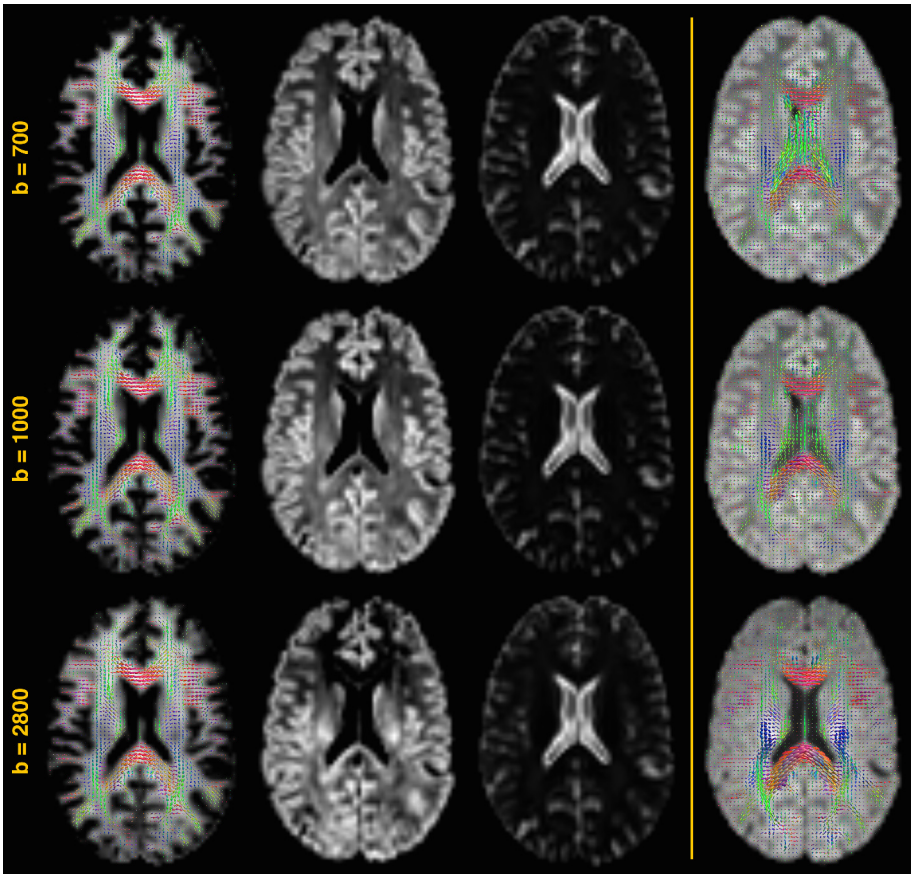

Figure 6.17: Left: Tissue ODFs estimated from T1 and single-shell DWI in dataset 2, estimated with CNSF. Right: Fibre ODF of single-shell CSD.

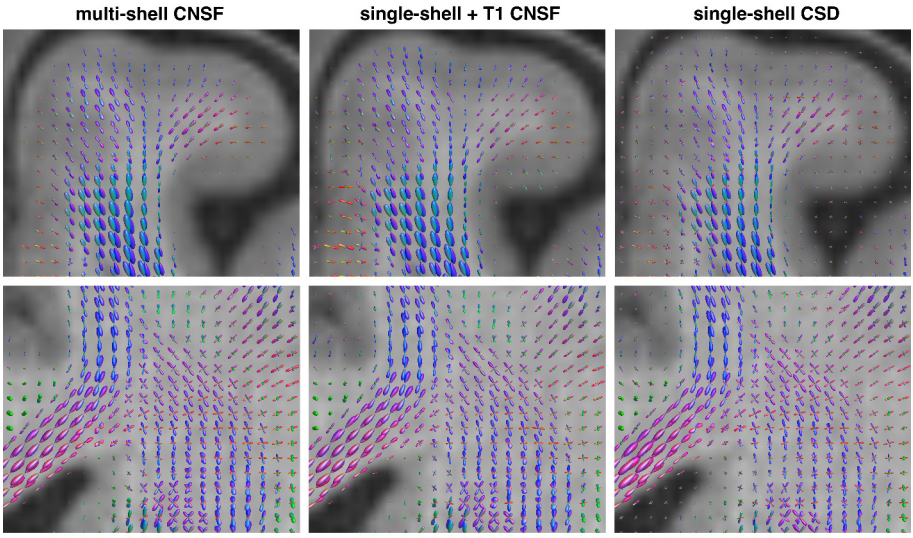

Figure 6.18: Comparison of the proposed method to multi-shell CNSF and single-shell CSD in dataset 1. Coronal slice of the left frontal superior gyrus (top) and the semioval centre (bottom), overlaid on the T1-image.

Chapter 7

Conclusions and future work

7.1 Summary discussion

Imaging neural micro- and macro-structure in vivo is of high relevance to research and clinical practice alike. Diffusion-weighted MRI offers a unique means towards this goal, but requires dedicated image analysis pipelines adapted to the spherical nature of the signal in each voxel. In addition, analysis methods are complicated by large partial voluming, low SNR, acquisition artefacts, and the complexity of the brain itself.

In this thesis, we improved state-of-the-art image analysis methods for DWI, both at local (voxel) and global (image) scale. A constant throughout our work has been to avoid relying on parametric or biophysical models, opting for a data-driven approach instead. To clarify, we do not object to models as such—in fact, any set of assumptions can be considered a model, including those used in this thesis—but wish to limit the model to its bare essentials, with minimal prior assumptions related to the image and the imaging process (the data). For instance, one may assume antipodal symmetry of DWI data, linear partial voluming in both spatial and angular domains, and little to no intercompartmental exchange on the time scale of the acquisition. Further assuming that the diffusion characteristics of neural fibres are identical across the brain leads to the spherical convolution model [88] upon which most of our work is founded. Data-driven approaches give rise to *sensitive* measures of white matter volume and its diffusion properties in normal and pathologic brain [113]. Biophysical models, on the other hand, intend to provide *specific* measures of white matter microstructure, assuming a model of diffusion in individual

cellular compartments. While there is a certain appeal to such microstructural measures, their estimates heavily depend on the model design and its implicit assumptions, which are hard to validate or even known to be untrue. Therefore, we prefer a more conservative perspective in which biophysical properties are as much as possible estimated from and thus adapted to the data at hand.

7.1.1 Global tractography

In Chapter 3, we applied this data-driven perspective to global tractography, incorporating a multi-shell fibre response function, estimated from the data, in the generative segment model and additionally adopting a multi-tissue model [118] of linear partial voluming with isotropic GM and CSF. As such, we integrated local spherical deconvolution and global optimization into one comprehensive framework, suitable for a diverse range of datasets. Our implementation was made publicly available as part of MRtrix3[1].

This integrated optimization framework serves a dual purpose. On the one hand the local tissue geometry is informed by spatial regularization stemming from the surrounding global fibre structure, improving robustness in data of limited resolution and SNR. This increased robustness ultimately benefits the track reconstruction as well. Indeed, validation results in simulated data demonstrated increased specificity of the tractometer connectivity metrics, outperforming state-of-the-art streamline and global approaches, particularly in data of low SNR.

On the other hand, the global track density is informed by the local apparent fibre density in the data, paving the way towards *quantitative* tractography of white matter structure and connectivity. Ensuring such quantitative correspondence between track density and the DWI data is a first requirement for reliable structural connectomics. A second requirement is that all tracks effectively connect grey matter regions, i.e., that no end points in white matter occur. Such anatomical constraints are currently not yet enforced in our global tractography framework, and a topic of future work.

7.1.2 Population priors and atlases

In Chapter 4, we investigated whether tractography could benefit from a model of the expected anatomy in the form of an atlas, as learned from a representative subject population. Such atlas-based analysis is popular and successful in segmentation and label fusion, hence by analogy we hypothesized

[1] http://www.mrtrix.org

that atlas priors may be helpful in tractography too. We demonstrated that global tractography is well suited for incorporating atlas priors, and explored both a local prior of the expected track orientation distribution in each voxel and a global prior of the labelled fibre bundle to which tracks belong.

Our experiments showed greatest benefit with a global labelling prior, which facilitates joint bundle segmentation in addition to excluding false positive fibres. While the local TOD prior may also reduce spurious fibres and robustify the reconstruction, its current sum-of-squared error metric may bias the predicted fibre density in pathology. The global label prior does not suffer from this limitation, and actually contributes a new source of information that cannot be extracted otherwise. Of course, both local and global priors will still be sensitive to morphological pathology such as tumour mass effect, but we argue that this issue needs to be addressed at the registration level. The foremost limitation of atlas-guided tractography then becomes the atlas itself, which needs to capture the full richness of the expected track configuration and its variability.

In Chapter 5, we therefore looked at atlas construction and addressed some of the challenges it presents. First, we introduced a novel approach to groupwise diffeomorphic track set registration leveraging a TOD representation. Such direct registration of subject tractograms outperforms registering the underlying images in dense white matter regions, and could be particularly beneficial in subjects with lesions or tumours that may complicate conventional image registration. While the method was demonstrated with full-brain probabilistic streamline tracking, it is equally applicable to global tractography and to tractography of segmented white matter bundles.

Second, we developed a hybrid bundle segmentation method for streamline tractography, using supervised machine learning classifiers in spectral embedding space. While training data was extracted from a Freesurfer-parcellation with so-called white matter *queries* [164], our results show that the proposed hybrid approach succeeds to label incomplete or interrupted tracks based on their similarity in the embedding space. Such semi-automated fibre-bundle segmentation method could be employed for defining labelled white matter atlases to be used as tractography prior. Ultimately, one may envisage an iterative framework akin to Ziyan *et al.* [173], in which global tractography and labelling recursively inform and improve each other.

7.1.3 Nonnegative DWI factorization

In Chapter 6, we returned to an essential, yet often overlooked, prerequisite of data-driven DWI analysis: estimating the signal response of a single fibre population or of any tissue sample in general. Such response functions are vital

to both local and global fibre reconstruction, and typically obtained by means of prior tissue segmentation of a T1 image. However, T1 and DWI data are often not in spatial alignment with one another due to MRI distortions of the latter, impeding typical pipelines for response function estimation. Rooted in this rather practical motivation, we developed a novel method for multi-tissue RF estimation solely based on DWI. The proposed methodology can nonetheless be regarded as a more general blind source separation technique for spherical data such as DWI, based on convexity-constrained nonnegative factorization.

We have shown that this factorization approach can successfully retrieve tissue components associated with WM, GM, and CSF in normal brain data, in vivo and ex vivo. In the presence of pathology, our method detected and segmented edema as an additional component. These examples illustrate tremendous potential of unsupervised DWI decomposition for analyzing data of unknown tissue structure. For example, we expect this technique to be applicable in cardiac DWI, possibly revealing myocardial fibre structure, or in perinatal imaging, possibly revealing early white matter development and myelination. Moreover, our method can be readily extended to multi-modal data, enabling fusion with T1, Flair, MRS, etc. We have demonstrated one successful application in which single-shell DWI was augmented with T1 data to recover a 3-tissue model. Other possibilities may include pathology segmentation and characterization in brain tumours.

7.2 Future perspectives

In addition to the possible extensions and improvements that were described in each chapter, we conclude this thesis with an outlook of larger trends, challenges and opportunities for diffusion-weighted imaging and neuroimaging in general.

Recent years have been marked by a shift towards high angular resolution and multi-shell acquisition in research studies, facilitating the use of advanced signal and microstructure models beyond the diffusion tensor. The next step is to bring these higher order models to the clinic too, sparking growing interest in compressed sensing and super-resolution techniques in MRI [282, 283]. In addition, large-scale data gathering initiatives such as the Human Connectome Project provide new opportunities for neuroscience and connectomics. However, these datasets also entail new challenges for multi-modal and multi-centre data fusion across large cohorts of subjects and patients. Furthermore, we expect continued advances in DWI acquisition and preprocessing, including q-space trajectory imaging [284], EPI distortion correction [272], denoising [225] and Gibbs-ringing removal [285].

Nonetheless, in vivo validation—or lack thereof—of local microstructure and global connectivity remains a fundamental challenge in DWI analysis. Although a new lipid-clearing microscopy technique known as CLARITY [195, 196] now facilitates ex vivo imaging of large networks of neurons with unprecedented ease and accuracy [197], the full brain microscopic connectome remains far off. Meanwhile, the DWI community has been embroiled in a strongly opinionated debate about biophysical models of microstructure. In the absence of a gold standard, this running battle on which model is right may continue for some time. However, as illustrated in this thesis and related studies, clinically relevant information can still be extracted without strong model assumptions.

Therefore, we expect further improvements to data-driven DWI analysis and increased use thereof in research and clinical practice. In addition, we expect a growing interest in machine learning methods that could learn structure in the data automatically and predict biomarkers directly. Future work can explore supervised techniques for feature prediction [286–289] and expand these to the spherical nature of DWI data. Unsupervised techniques such as the blind factorization introduced in Chapter 6 may be adapted for microstructure imaging, possibly incorporating sparsity priors or spatial regularization. The latter could be imposed via a global tractography framework, unifying the main contributions of this thesis into one comprehensive framework and hence enabling truly multi-scale reconstruction of white matter fibres.

Bibliography

[1] O. H. Petersen, *Lecture Notes: Human Physiology*, 5th. Oxford: Blackwell Publishing Ltd, 2006, p. 664.

[2] Blausen Staff, "Blausen gallery 2014", *Wikiversity Journal of Medicine*, 2014. DOI: 10.15347/wjm/2014.010.

[3] S. Brown, "Responsibility in crime from the medical standpoint", *Popular Science Monthly*, vol. 46, no. 2, pp. 154–164, Dec. 1894.

[4] L. J. O'Donnell, "Cerebral white matter analysis using diffusion imaging", PhD thesis, Massachusetts Institute of Technology, 2006.

[5] O. Sporns, G. Tononi, and R. Kötter, "The human connectome: A structural description of the human brain", *PLoS Computational Biology*, vol. 1, no. 4, e42, 2005. DOI: 10.1371/journal.pcbi.0010042.

[6] C. L. Dumoulin and P. A. Turski, "Phase contrast MRA", in *Encyclopedia of Magnetic Resonance*, R. K. Harris, Ed., Chichester, UK: John Wiley & Sons, Ltd, Mar. 2007. DOI: 10.1002/9780470034590.emrstm0388.

[7] R. B. Buxton, L. R. Frank, E. C. Wong, B. Siewert, S. Warach, and R. R. Edelman, "A general kinetic model for quantitative perfusion imaging with arterial spin labeling", *Magn. Reson. Med.*, vol. 40, no. 3, pp. 383–396, Sep. 1998. DOI: 10.1002/mrm.1910400308.

[8] S. Ogawa, T. M. Lee, A. R. Kay, and D. W. Tank, "Brain magnetic resonance imaging with contrast dependent on blood oxygenation", *Proc. Natl. Acad. Sci. USA*, vol. 87, no. 24, pp. 9868–72, Dec. 1990.

[9] K. J. Friston, P. Fletcher, O. Josephs, A. Holmes, M. D. Rugg, and R. Turner, "Event-related fMRI: Characterizing differential responses", *NeuroImage*, vol. 7, no. 1, pp. 30–40, Jan. 1998. DOI: 10.1006/nimg.1997.0306.

[10] M. W. Woolrich, B. D. Ripley, M. Brady, and S. M. Smith, "Temporal autocorrelation in univariate linear modeling of fMRI data", *NeuroImage*, vol. 14, no. 6, pp. 1370–86, Dec. 2001. DOI: 10.1006/nimg.2001.0931.

[11] N. K. Logothetis, J. Pauls, M. Augath, T. Trinath, and A. Oeltermann, "Neurophysiological investigation of the basis of the fMRI signal", *Nature*, vol. 412, no. 6843, pp. 150–7, Jul. 2001. DOI: 10.1038/35084005.

[12] D. Le Bihan, E. Breton, D. Lallemand, P. Grenier, E. Cabanis, and M. Laval-Jeantet, "MR imaging of intravoxel incoherent motions: Application to diffusion and perfusion in neurologic disorders.", *Radiology*, vol. 161, no. 2, pp. 401–407, Nov. 1986. DOI: 10.1148/radiology.161.2.3763909.

[13] A. Mackay, K. Whittall, J. Adler, D. Li, D. Paty, and D. Graeb, "In vivo visualization of myelin water in brain by magnetic resonance", *Magn. Reson. Med.*, vol. 31, no. 6, pp. 673–677, Jun. 1994. DOI: 10.1002/mrm.1910310614.

[14] M. E. Moseley, Y. Cohen, J. Mintorovitch, L. Chileuitt, H. Shimizu, J. Kucharczyk, M. F. Wendland, and P. R. Weinstein, "Early detection of regional cerebral ischemia in cats: Comparison of diffusion- and T2-weighted MRI and spectroscopy", *Magn. Reson. Med.*, vol. 14, no. 2, pp. 330–346, May 1990. DOI: 10.1002/mrm.1910140218.

[15] C. Beaulieu, "The basis of anisotropic water diffusion in the nervous system – a technical review", *NMR in Biomedicine*, vol. 15, no. 7-8, pp. 435–455, 2002. DOI: 10.1002/nbm.782.

[16] D. J. Werring, C. A. Clark, G. J. Barker, A. J. Thompson, and D. H. Miller, "Diffusion tensor imaging of lesions and normal-appearing white matter in multiple sclerosis", *Neurology*, vol. 52, no. 8, pp. 1626–1626, May 1999. DOI: 10.1212/WNL.52.8.1626.

[17] R. Bammer, M. Augustin, S. Strasser-Fuchs, T. Seifert, P. Kapeller, R. Stollberger, F. Ebner, H. P. Hartung, and F. Fazekas, "Magnetic resonance diffusion tensor imaging for characterizing diffuse and focal white matter abnormalities in multiple sclerosis", *Magn. Reson. Med.*, vol. 44, no. 4, pp. 583–91, Oct. 2000.

[18] M. Filippi, M. Cercignani, M. Inglese, M. Horsfield, and G. Comi, "Diffusion tensor magnetic resonance imaging in multiple sclerosis", *Neurology*, vol. 56, no. 3, pp. 304–311, Feb. 2001. DOI: 10.1212/WNL.56.3.304.

[19] S.-K. Song, S.-W. Sun, M. J. Ramsbottom, C. Chang, J. Russell, and A. H. Cross, "Dysmyelination revealed through MRI as increased radial (but unchanged axial) diffusion of water", *NeuroImage*, vol. 17, no. 3, pp. 1429–1436, Nov. 2002. DOI: 10.1006/nimg.2002.1267.

[20] S. Mori and P. C. M. van Zijl, "Fiber tracking: Principles and strategies – a technical review", *NMR in Biomedicine*, vol. 15, no. 7-8, pp. 468–480, 2002. DOI: 10.1002/nbm.781.

[21] J.-D. Tournier, S. Mori, and A. Leemans, "Diffusion tensor imaging and beyond", *Magn. Reson. Med.*, vol. 65, no. 6, pp. 1532–1556, Apr. 2011. DOI: 10.1002/mrm.22924.

[22] G. B. Frisoni, N. C. Fox, C. R. Jack, P. Scheltens, and P. M. Thompson, "The clinical use of structural MRI in Alzheimer disease", *Nature Reviews Neurology*, vol. 6, no. 2, pp. 67–77, Feb. 2010. DOI: 10.1038/nrneurol.2009.215.

[23] D. Christiaens, M. Reisert, T. Dhollander, S. Sunaert, P. Suetens, and F. Maes, "Global tractography of multi-shell diffusion-weighted imaging data using a multi-tissue model", *NeuroImage*, vol. 123, pp. 89–101, Dec. 2015. DOI: 10.1016/j.neuroimage.2015.08.008.

[24] D. Christiaens, M. Reisert, T. Dhollander, F. Maes, S. Sunaert, and P. Suetens, "Atlas-guided global tractography: Imposing a prior on the local track orientation", in *Computational Diffusion MRI – MICCAI Workshop*, L. O'Donnell, G. Nedjati-Gilani, Y. Rathi, M. Reisert, and T. Schneider, Eds., ser. Mathematics and Visualization, Cambridge, MA, USA: Springer International Publishing, Sep. 2014, pp. 115–123. DOI: 10.1007/978-3-319-11182-7_11.

[25] D. Christiaens, F. Maes, S. Sunaert, and P. Suetens, "Imposing label priors in global tractography can resolve crossing fibre ambiguities", in *International Society for Magnetic Resonance in Medicine (ISMRM) 23th Annual Meeting & Exhibtion*, vol. 23, Toronto, Ontario, Canada, May 2015, p. 2258.

[26] D. Christiaens, T. Dhollander, F. Maes, S. Sunaert, and P. Suetens, "Groupwise deformable registration of fiber track sets using track orientation distributions", in *Computational Diffusion MRI and Brain Connectivity – MICCAI Workshop*, T. Schultz, G. Nedjati-Gilani, A. Venkataraman, L. O'Donnell, and E. Panagiotaki, Eds., ser. Mathematics and Visualization, Nagoya, Japan: Springer International Publishing, Sep. 2013, pp. 151–161. DOI: 10.1007/978-3-319-02475-2_14.

[27] D. Christiaens, F. Maes, S. Sunaert, and P. Suetens, "Convex non-negative spherical factorization of multi-shell diffusion-weighted images", in *Medical Image Computing and Computer-Assisted Intervention – MICCAI 2015*, N. Navab, J. Hornegger, W. M. Wells, and A. F. Frangi, Eds., ser. Lecture Notes in Computer Science, vol. 9349, Munich, Germany: Springer International Publishing, Oct. 2015, pp. 166–173. DOI: 10.1007/978-3-319-24553-9_21.

[28] R. Brown, "XXVII. a brief account of microscopical observations made in the months of june, july and august 1827, on the particles contained in the pollen of plants; and on the general existence of active molecules in organic and inorganic bodies", *Philosophical Magazine Series 2*, vol. 4, no. 21, pp. 161–173, Sep. 1828. DOI: 10.1080/14786442808674769.

[29] A. Einstein, "Über die von der molekularkinetischen Theorie der Wärme geforderte Bewegung von in ruhenden Flüssigkeiten suspendierten Teilchen", *Ann. Phys.*, vol. 322, no. 8, pp. 549–560, 1905. DOI: 10.1002/andp.19053220806.

[30] M. von Smoluchowski, "Zur kinetischen Theorie der Brownschen Molekularbewegung und der Suspensionen", *Ann. Phys.*, vol. 326, no. 14, pp. 756–780, 1906. DOI: 10.1002/andp.19063261405.

[31] A. Fick, "Ueber Diffusion", *Ann. Phys. Chem.*, vol. 170, no. 1, pp. 59–86, 1855. DOI: 10.1002/andp.18551700105.

[32] D. S. Novikov, "Bloch-Torrey equation & diffusion imaging (DWI, DTI, q-space imaging)", in *ISMRM Weekend Educational Course on MR Physics for Physicists*, Toronto, Canada, May 2015.

[33] P. J. Basser, J. Mattiello, and D. Le Bihan, "MR diffusion tensor spectroscopy and imaging", *Biophysical Journal*, vol. 66, no. 1, pp. 259–267, Jan. 1994. DOI: 10.1016/s0006-3495(94)80775-1.

[34] J. Crank, *The Mathematics of Diffusion*, ser. Oxford science publications. Clarendon Press, 1979.

[35] F. Bloch, "Nuclear induction", *Phys. Rev.*, vol. 70, no. 7-8, pp. 460–474, Oct. 1946. DOI: 10.1103/physrev.70.460.

[36] E. M. Purcell, H. C. Torrey, and R. V. Pound, "Resonance absorption by nuclear magnetic moments in a solid", *Phys. Rev.*, vol. 69, no. 1-2, pp. 37–38, Jan. 1946. DOI: 10.1103/physrev.69.37.

[37] D. W. McRobbie, E. A. Moore, M. J. Graves, and M. R. Prince, *MRI From Picture to Proton*. Cambridge: Cambridge University Press, 2006. DOI: 10.1017/CBO9780511545405.

[38] P. C. Lauterbur, "Image formation by induced local interactions: Examples employing nuclear magnetic resonance", *Nature*, vol. 242, no. 5394, pp. 190–191, Mar. 1973. DOI: 10.1038/242190a0.

[39] P. Mansfield, "Multi-planar image formation using NMR spin echoes", *J. Phys. C: Solid State Phys.*, vol. 10, no. 3, pp. L55–L58, Feb. 1977. DOI: 10.1088/0022-3719/10/3/004.

[40] E. O. Stejskal and J. E. Tanner, "Spin diffusion measurements: Spin echoes in the presence of a time-dependent field gradient", *The Journal of Chemical Physics*, vol. 42, no. 1, p. 288, 1965. DOI: 10.1063/1.1695690.

[41] R. Bammer, "Basic principles of diffusion-weighted imaging", *European Journal of Radiology*, vol. 45, no. 3, pp. 169–184, Mar. 2003. DOI: 10.1016/s0720-048x(02)00303-0.

[42] R. Luypaert, S. Boujraf, S. Sourbron, and M. Osteaux, "Diffusion and perfusion MRI: Basic physics", *European Journal of Radiology*, vol. 38, no. 1, pp. 19–27, Apr. 2001. DOI: 10.1016/s0720-048x(01)00286-8.

[43] P. T. Callaghan, C. D. Eccles, and Y. Xia, "NMR microscopy of dynamic displacements: k-space and q-space imaging", *J. Phys. E: Sci. Instrum.*, vol. 21, no. 8, pp. 820–822, Aug. 1988. DOI: 10.1088/0022-3735/21/8/017.

[44] P. T. Callaghan, A. Coy, D. MacGowan, K. J. Packer, and F. O. Zelaya, "Diffraction-like effects in NMR diffusion studies of fluids in porous solids", *Nature*, vol. 351, no. 6326, pp. 467–469, Jun. 1991. DOI: 10.1038/351467a0.

[45] V. J. Wedeen, P. Hagmann, W.-Y. I. Tseng, T. G. Reese, and R. M. Weisskoff, "Mapping complex tissue architecture with diffusion spectrum magnetic resonance imaging", *Magn. Reson. Med.*, vol. 54, no. 6, pp. 1377–1386, 2005. DOI: 10.1002/mrm.20642.

[46] J. Mattiello, P. J. Basser, and D. Le Bihan, "The b-matrix in diffusion tensor echo-planar imaging", *Magn. Reson. Med.*, vol. 37, no. 2, pp. 292–300, Feb. 1997. DOI: 10.1002/mrm.1910370226.

[47] N. G. Papadakis, C. D. Murrills, L. D. Hall, C. L. Huang, and T. Adrian Carpenter, "Minimal gradient encoding for robust estimation of diffusion anisotropy", *Magn. Reson. Imaging*, vol. 18, no. 6, pp. 671–679, 2000.

[48] D. K. Jones, "The effect of gradient sampling schemes on measures derived from diffusion tensor MRI: A Monte Carlo study", *Magn. Reson. Med.*, vol. 51, no. 4, pp. 807–815, 2004.

[49] S. Pajevic and C. Pierpaoli, "Color schemes to represent the orientation of anisotropic tissues from diffusion tensor data: Application to white matter fiber tract mapping in the human brain", *Magn. Reson. Med.*, vol. 42, no. 3, pp. 526–540, Sep. 1999.

[50] J. H. Jensen, J. A. Helpern, A. Ramani, H. Lu, and K. Kaczynski, "Diffusional kurtosis imaging: The quantification of non-Gaussian water diffusion by means of magnetic resonance imaging", *Magn. Reson. Med.*, vol. 53, no. 6, pp. 1432–1440, Jun. 2005. DOI: 10.1002/mrm.20508.

[51] H. Lu, J. H. Jensen, A. Ramani, and J. A. Helpern, "Three-dimensional characterization of non-Gaussian water diffusion in humans using diffusion kurtosis imaging", *NMR in Biomedicine*, vol. 19, no. 2, pp. 236–247, Apr. 2006. DOI: 10.1002/nbm.1020.

[52] L. Minati, D. Aquino, S. Rampoldi, S. Papa, M. Grisoli, M. G. Bruzzone, and E. Maccagnano, "Biexponential and diffusional kurtosis imaging, and generalised diffusion-tensor imaging (GDTI) with rank-4 tensors: A study in a group of healthy subjects", *Magnetic Resonance Materials in Physics, Biology and Medicine*, vol. 20, no. 5-6, pp. 241–253, Dec. 2007. DOI: 10.1007/s10334-007-0091-1.

[53] V. G. Kiselev, "The cumulant expansion: An overarching mathematical framework for understanding diffusion NMR", in *Diffusion MRI*, Oxford University Press, Nov. 2010, pp. 152–168. DOI: 10.1093/med/9780195369779.003.0010.

[54] D. Poot, A. den Dekker, E. Achten, M. Verhoye, and J. Sijbers, "Optimal experimental design for diffusion kurtosis imaging", *IEEE Trans. Med. Imag.*, vol. 29, no. 3, pp. 819–829, Mar. 2010. DOI: 10.1109/TMI.2009.2037915.

[55] T. E. J. Behrens, H. Johansen-Berg, S. Jbabdi, M. F. S. Rushworth, and M. W. Woolrich, "Probabilistic diffusion tractography with multiple fibre orientations: What can we gain?", *NeuroImage*, vol. 34, no. 1, pp. 144–155, 2007.

[56] B. Jeurissen, A. Leemans, J.-D. Tournier, D. K. Jones, and J. Sijbers, "Investigating the prevalence of complex fiber configurations in white matter tissue with diffusion magnetic resonance imaging", *Human Brain Mapping*, vol. 34, no. 11, pp. 2747–2766, May 2012. DOI: 10.1002/hbm.22099.

[57] D. S. Tuch, T. G. Reese, M. R. Wiegell, N. Makris, J. W. Belliveau, and V. J. Wedeen, "High angular resolution diffusion imaging reveals intravoxel white matter fiber heterogeneity", *Magn. Reson. Med.*, vol. 48, no. 4, pp. 577–582, Sep. 2002. DOI: 10.1002/mrm.10268.

[58] M. Descoteaux, "High angular resolution diffusion MRI: From local estimation to segmentation and tractography", PhD thesis, University of Nice-Sophia Antipolis, 2008.

[59] L. R. Frank, "Characterization of anisotropy in high angular resolution diffusion-weighted MRI", *Magn. Reson. Med.*, vol. 47, no. 6, pp. 1083–1099, Jun. 2002. DOI: 10.1002/mrm.10156.

[60] M. Descoteaux, E. Angelino, S. Fitzgibbons, and R. Deriche, "Apparent diffusion coefficients from high angular resolution diffusion imaging: Estimation and applications", *Magn. Reson. Med.*, vol. 56, no. 2, pp. 395–410, 2006. DOI: 10.1002/mrm.20948.

[61] ——, "Regularized, fast, and robust analytical q-ball imaging", *Magn. Reson. Med.*, vol. 58, no. 3, pp. 497–510, 2007. DOI: 10.1002/mrm.21277.

[62] D. S. Tuch, "Q-ball imaging", *Magn. Reson. Med.*, vol. 52, no. 6, pp. 1358–1372, 2004. DOI: 10.1002/mrm.20279.

[63] A. Tristán-Vega, C.-F. Westin, and S. Aja-Fernández, "Estimation of fiber orientation probability density functions in high angular resolution diffusion imaging", *NeuroImage*, vol. 47, no. 2, pp. 638–50, Aug. 2009. DOI: 10.1016/j.neuroimage.2009.04.049.

[64] I. Aganj, C. Lenglet, G. Sapiro, E. Yacoub, K. Ugurbil, and N. Harel, "Reconstruction of the orientation distribution function in single- and multiple-shell q-ball imaging within constant solid angle", *Magn. Reson. Med.*, vol. 64, no. 2, pp. 554–566, Aug. 2010. DOI: 10.1002/mrm.22365.

[65] A. Tristán-Vega, C.-F. Westin, and S. Aja-Fernández, "A new methodology for the estimation of fiber populations in the white matter of the brain with the Funk-Radon transform", *NeuroImage*, vol. 49, no. 2, pp. 1301–15, Jan. 2010. DOI: 10.1016/j.neuroimage.2009.09.070.

[66] C. Thomsen, O. Henriksen, and P. Ring, "In vivo measurement of water self diffusion in the human brain by magnetic resonance imaging", *Acta Radiologica*, vol. 28, no. 3, pp. 353–361, Jan. 1987. DOI: 10.3109/02841858709177362.

[67] M. E. Moseley, Y. Cohen, J. Kucharczyk, J. Mintorovitch, H. S. Asgari, M. F. Wendland, J. Tsuruda, and D. Norman, "Diffusion-weighted MR imaging of anisotropic water diffusion in cat central nervous system", *Radiology*, vol. 176, no. 2, pp. 439–445, Aug. 1990. DOI: 10.1148/radiology.176.2.2367658.

[68] J. V. Hajnal, M. Doran, A. S. Hall, A. G. Collins, A. Oatridge, J. M. Pennock, G. M. Bydder, *et al.*, "MR imaging of anisotropically restricted diffusion of water in the nervous system: Technical, anatomic, and pathologic considerations", *Journal of computer assisted tomography*, vol. 15, no. 1, pp. 1–18, 1991.

[69] P. Douek, R. Turner, J. Pekar, N. Patronas, and D. Le Bihan, "MR color mapping of myelin fiber orientation", *Journal of computer assisted tomography*, vol. 15, no. 6, pp. 923–929, 1991.

[70] P. J. Basser and E. Özarslan, "Introduction to diffusion MR", in *Diffusion MRI: From quantitative measurement to in vivo neuroanatomy*, H. Johansen-Berg and T. E. Behrens, Eds., Elsevier BV, 2009, pp. 2–10. DOI: 10.1016/b978-0-12-374709-9.00001-8.

[71] G. J. Stanisz, G. A. Wright, R. M. Henkelman, and A. Szafer, "An analytical model of restricted diffusion in bovine optic nerve", *Magn. Reson. Med.*, vol. 37, no. 1, pp. 103–111, Jan. 1997. DOI: 10.1002/mrm.1910370115.

[72] E. Panagiotaki, T. Schneider, B. Siow, M. G. Hall, M. F. Lythgoe, and D. C. Alexander, "Compartment models of the diffusion MR signal in brain white matter: A taxonomy and comparison", *NeuroImage*, vol. 59, no. 3, pp. 2241–2254, Feb. 2012. DOI: 10.1016/j.neuroimage.2011.09.081.

[73] U. Ferizi, T. Schneider, E. Panagiotaki, G. Nedjati-Gilani, H. Zhang, C. A. M. Wheeler-Kingshott, and D. C. Alexander, "A ranking of diffusion MRI compartment models with in vivo human brain data", *Magn. Reson. Med.*, vol. 72, no. 6, pp. 1785–92, Dec. 2014. DOI: 10.1002/mrm.25080.

[74] T. Behrens, M. Woolrich, M. Jenkinson, H. Johansen-Berg, R. Nunes, S. Clare, P. Matthews, J. Brady, and S. Smith, "Characterization and propagation of uncertainty in diffusion-weighted MR imaging", *Magn. Reson. Med.*, vol. 50, no. 5, pp. 1077–1088, Oct. 2003. DOI: 10.1002/mrm.10609.

[75] Y. Assaf, R. Z. Freidlin, G. K. Rohde, and P. J. Basser, "New modeling and experimental framework to characterize hindered and restricted water diffusion in brain white matter", *Magn. Reson. Med.*, vol. 52, no. 5, pp. 965–978, 2004.

[76] Y. Assaf and P. J. Basser, "Composite hindered and restricted model of diffusion (CHARMED) MR imaging of the human brain", *NeuroImage*, vol. 27, no. 1, pp. 48–58, Aug. 2005. DOI: 10.1016/j.neuroimage.2005.03.042.

[77] Y. Assaf, T. Blumenfeld-Katzir, Y. Yovel, and P. J. Basser, "AxCaliber: A method for measuring axon diameter distribution from diffusion MRI", *Magn. Reson. Med.*, vol. 59, no. 6, pp. 1347–54, 2008. DOI: 10.1002/mrm.21577.

[78] D. C. Alexander, P. L. Hubbard, M. G. Hall, E. A. Moore, M. Ptito, G. J. M. Parker, and T. B. Dyrby, "Orientationally invariant indices of axon diameter and density from diffusion MRI", *NeuroImage*, vol. 52, no. 4, pp. 1374–89, Oct. 2010. DOI: 10.1016/j.neuroimage.2010.05.043.

[79] T. B. Dyrby, L. V. Søgaard, M. G. Hall, M. Ptito, and D. C. Alexander, "Contrast and stability of the axon diameter index from microstructure imaging with diffusion MRI", *Magn. Reson. Med.*, vol. 70, no. 3, pp. 711–21, Sep. 2013. DOI: 10.1002/mrm.24501.

[80] M. Nilsson, J. Lätt, F. Ståhlberg, D. Westen, and H. Hagslätt, "The importance of axonal undulation in diffusion MR measurements: A Monte Carlo simulation study", *NMR in Biomedicine*, vol. 25, no. 5, pp. 795–805, May 2012. DOI: 10.1002/nbm.1795.

[81] T. P. Hosey, G. B. Williams, and R. E. Ansorge, "Inference of multiple fiber orientations in high angular resolution diffusion imaging", *Magn. Reson. Med.*, vol. 54, no. 6, pp. 1480–1489, 2005.

[82] B. Scherrer, A. Schwartzman, M. Taquet, S. P. Prabhu, M. Sahin, A. Akhondi-Asl, and S. K. Warfield, "Characterizing the distribution of anisotropic micro-structural environments with diffusion-weighted imaging (DIAMOND)", in *Medical Image Computing and Computer-Assisted Intervention – MICCAI 2013*, ser. Lecture Notes in Computer Science Pt 3, K. Mori, I. Sakuma, Y. Sato, C. Barrilot, and N. Navab, Eds., vol. 8151, Nagoya, Japan, 2013, pp. 518–526. DOI: 10.1007/978-3-642-40760-4_65.

[83] E. Kaden, T. R. Knösche, and A. Anwander, "Parametric spherical deconvolution: Inferring anatomical connectivity using diffusion MR imaging", *NeuroImage*, vol. 37, no. 2, pp. 474–488, Aug. 2007. DOI: 10.1016/j.neuroimage.2007.05.012.

[84] H. Zhang, P. L. Hubbard, G. J. M. Parker, and D. C. Alexander, "Axon diameter mapping in the presence of orientation dispersion with diffusion MRI", *NeuroImage*, vol. 56, no. 3, pp. 1301–15, Jun. 2011. DOI: 10.1016/j.neuroimage.2011.01.084.

[85] H. Zhang, T. Schneider, C. a. Wheeler-Kingshott, and D. C. Alexander, "NODDI: practical in vivo neurite orientation dispersion and density imaging of the human brain", *NeuroImage*, vol. 61, no. 4, pp. 1000–16, Jul. 2012. DOI: 10.1016/j.neuroimage.2012.03.072.

[86] S. N. Sotiropoulos, T. E. Behrens, and S. Jbabdi, "Ball and rackets: Inferring fiber fanning from diffusion-weighted MRI", *NeuroImage*, vol. 60, no. 2, pp. 1412–1425, Apr. 2012. DOI: 10.1016/j.neuroimage.2012.01.056.

[87] M. Tariq, T. Schneider, D. C. Alexander, C. A. M. Wheeler-Kingshott, and H. Zhang, "In vivo estimation of dispersion anisotropy of neurites using diffusion MRI", in *Medical Image Computing and Computer-Assisted Intervention – MICCAI 2014*, ser. Lecture Notes in Computer Science Pt 3, P. Golland, N. Hata, C. Barrillot, J. Hornegger, and R. Howe, Eds., vol. 8675, Boston, MA, USA: Springer, 2014, pp. 241–248. DOI: 10.1007/978-3-319-10443-0_31.

[88] J.-D. Tournier, F. Calamante, D. G. Gadian, and A. Connelly, "Direct estimation of the fiber orientation density function from diffusion-weighted MRI data using spherical deconvolution", *NeuroImage*, vol. 23, no. 3, pp. 1176–1185, Nov. 2004. DOI: 10.1016/j.neuroimage.2004.07.037.

[89] A. W. Anderson, "Measurement of fiber orientation distributions using high angular resolution diffusion imaging", *Magn. Reson. Med.*, vol. 54, no. 5, pp. 1194–206, 2005.

[90] M. Descoteaux, R. Deriche, T. Knosche, and A. Anwander, "Deterministic and probabilistic tractography based on complex fibre orientation distributions", *IEEE Trans. Med. Imag.*, vol. 28, no. 2, pp. 269–286, Feb. 2009. DOI: 10.1109/tmi.2008.2004424.

[91] J.-D. Tournier, F. Calamante, and A. Connelly, "Robust determination of the fibre orientation distribution in diffusion MRI: Non-negativity constrained super-resolved spherical deconvolution", *NeuroImage*, vol. 35, no. 4, pp. 1459–1472, May 2007. DOI: 10.1016/j.neuroimage.2007.02.016.

[92] J.-D. Tournier, F. Calamante, and A. Connelly, "Determination of the appropriate b-value and number of gradient directions for high-angular-resolution diffusion-weighted imaging", *NMR in Biomedicine*, vol. 26, no. 12, pp. 1775–86, Dec. 2013. DOI: 10.1002/nbm.3017.

[93] C. M. W. Tax, B. Jeurissen, S. B. Vos, M. A. Viergever, and A. Leemans, "Recursive calibration of the fiber response function for spherical deconvolution of diffusion MRI data", *NeuroImage*, vol. 86, pp. 67–80, Feb. 2014. DOI: 10.1016/j.neuroimage.2013.07.067.

[94] A. Goh, C. Lenglet, P. M. Thompson, and R. Vidal, "Estimating orientation distribution functions with probability density constraints and spatial regularity", in *Medical Image Computing and Computer-Assisted Intervention – MICCAI 2009*, ser. Lecture Notes in Computer Science, G.-Z. Yang, D. Hawkes, D. Rueckert, A. Noble, and C. Taylor, Eds., vol. 5761, London, UK: Springer Berlin Heidelberg, 2009, pp. 877–885. DOI: 10.1007/978-3-642-04268-3_108.

[95] M. Reisert and V. Kiselev, "Fiber continuity: An anisotropic prior for ODF estimation", *IEEE Trans. Med. Imag.*, vol. 30, no. 6, pp. 1274–1283, Jun. 2011. DOI: 10.1109/tmi.2011.2112769.

[96] J.-D. Tournier, F. Calamante, and A. Conelly, "A robust spherical deconvolution method for the analysis of low SNR or low angular resolution diffusion data", in *International Society of Magnetic Resonance in Medicine (ISMRM) 21st Annual Meeting*, vol. 21, Salt-Lake City, USA, 2013, p. 772.

[97] Q. Zhou, O. V. Michailovich, and Y. Rathi, "Spatially regularized reconstruction of fibre orientation distributions in the presence of isotropic diffusion", *Computing Research Repository*, vol. abs/1401.6196, 2014.

[98] E. J. Canales-Rodríguez, A. Daducci, S. N. Sotiropoulos, E. Caruyer, S. Aja-Fernández, J. Radua, J. M. Yurramendi Mendizabal, Y. Iturria-Medina, L. Melie-García, Y. Alemán-Gómez, J.-P. Thiran, S. Sarró, E. Pomarol-Clotet, and R. Salvador, "Spherical deconvolution of multichannel diffusion MRI data with non-Gaussian noise models and spatial regularization", Oct. 2014. arXiv: 1410.6353.

[99] ——, "Spherical deconvolution of multichannel diffusion MRI data with non-Gaussian noise models and spatial regularization", *PLoS ONE*, vol. 10, no. 10, A. Leemans, Ed., e0138910, Oct. 2015. DOI: 10.1371/journal.pone.0138910.

[100] M. Reisert, E. Kellner, and V. G. Kiselev, "About the geometry of asymmetric fiber orientation distributions", *IEEE Trans. Med. Imag.*, vol. 31, no. 6, pp. 1240–1249, Jun. 2012. DOI: 10.1109/TMI.2012.2187916.

[101] A. Tristán-Vega and C.-F. Westin, "Probabilistic ODF estimation from reduced HARDI data with sparse regularization", in *Medical Image Computing and Computer-Assisted Intervention – MICCAI 2011*, ser. Lecture Notes in Computer Science Pt 2, vol. 6892, Toronto, Canada: Springer, 2011, pp. 182–190. DOI: 10.1007/978-3-642-23629-7_23.

[102] A. Daducci, D. Van De Ville, J.-P. Thiran, and Y. Wiaux, "Sparse regularization for fiber ODF reconstruction: From the suboptimality of L2 and L1 priors to L0", p. 26, Aug. 2012. arXiv: 1208.2247.

[103] ——, "Sparse regularization for fiber ODF reconstruction: From the suboptimality of L2 and L1 priors to L0", *Med. Image Anal.*, vol. 18, no. 6, pp. 820–833, Aug. 2014. DOI: 10.1016/j.media.2014.01.011.

[104] T. Schultz and S. Groeschel, "Auto-calibrating spherical deconvolution based on ODF sparsity", in *Medical Image Computing and Computer-Assisted Intervention – MICCAI 2013*, ser. Lecture Notes in Computer Science, K. Mori, I. Sakuma, Y. Sato, C. Barrilot, and N. Navab, Eds., vol. 8149, Nagoya, Japan: Springer International Publishing, 2013, pp. 663–670. DOI: 10.1007/978-3-642-40811-3_83.

[105] F.-C. Yeh and W.-Y. I. Tseng, "Sparse solution of fiber orientation distribution function by diffusion decomposition", *PLoS ONE*, vol. 8, no. 10, P. A. Valdes-Sosa, Ed., e75747, Oct. 2013. DOI: 10.1371/journal.pone.0075747.

[106] O. Michailovich, Y. Rathi, and S. Dolui, "Spatially regularized compressed sensing for high angular resolution diffusion imaging", *IEEE Trans. Med. Imag.*, vol. 30, no. 5, pp. 1100–15, May 2011. DOI: 10.1109/TMI.2011.2142189.

[107] B. A. Landman, J. A. Bogovic, H. Wan, F. E. Z. ElShahaby, P.-L. Bazin, and J. L. Prince, "Resolution of crossing fibers with constrained compressed sensing using diffusion tensor MRI", *NeuroImage*, vol. 59, no. 3, pp. 2175–2186, Feb. 2012. DOI: 10.1016/j.neuroimage.2011.10.011.

[108] M. Mani, M. Jacob, A. Guidon, C. Liu, A. Song, V. Magnotta, and J. Zhong, "Acceleration of high angular and spatial resolution diffusion imaging using compressed sensing", in *9th IEEE International Symposium on Biomedical Imaging (ISBI)*, IEEE, May 2012, pp. 326–329. DOI: 10.1109/ISBI.2012.6235550.

[109] G. D. Parker, A. D. Marshall, P. L. Rosin, N. Drage, S. Richmond, and D. K. Jones, "A pitfall in the reconstruction of fibre ODFs using spherical deconvolution of diffusion MRI data", *NeuroImage*, vol. 65, pp. 433–448, Oct. 2013. DOI: 10.1016/j.neuroimage.2012.10.022.

[110] T. Roine, B. Jeurissen, D. Perrone, J. Aelterman, A. Leemans, W. Philips, and J. Sijbers, "Isotropic non-white matter partial volume effects in constrained spherical deconvolution", *Front. Neuroinform.*, vol. 8, Mar. 2014. DOI: 10.3389/fninf.2014.00028.

[111] F. Dell'Acqua, G. Rizzo, P. Scifo, R. A. Clarke, G. Scotti, and F. Fazio, "A model-based deconvolution approach to solve fiber crossing in diffusion-weighted MR imaging", *IEEE Trans. Biomed. Eng.*, vol. 54, no. 3, pp. 462–472, Mar. 2007. DOI: 10.1109/TBME.2006.888830.

[112] F. Dell'Acqua, P. Scifo, G. Rizzo, M. Catani, A. Simmons, G. Scotti, and F. Fazio, "A modified damped Richardson-Lucy algorithm to reduce isotropic background effects in spherical deconvolution", *NeuroImage*, vol. 49, no. 2, pp. 1446–58, Jan. 2010. DOI: 10.1016/j.neuroimage.2009.09.033.

[113] D. Raffelt, J.-D. Tournier, S. Rose, G. R. Ridgway, R. Henderson, S. Crozier, O. Salvado, and A. Connelly, "Apparent fibre density: A novel measure for the analysis of diffusion-weighted magnetic resonance images", *NeuroImage*, vol. 59, no. 4, pp. 3976–3994, Feb. 2012. DOI: 10.1016/j.neuroimage.2011.10.045.

[114] M. G. Hall and D. C. Alexander, "Finite pulse widths improve fibre orientation estimates in diffusion tensor MRI", in *International Society of Magnetic Resonance in Medicine (ISMRM) 14th Annual Meeting*, vol. 14, Seattle, WA, USA, 2006, p. 1076.

[115] C.-H. Yeh, J.-D. Tournier, K.-H. Cho, C.-P. Lin, F. Calamante, and A. Connelly, "The effect of finite diffusion gradient pulse duration on fibre orientation estimation in diffusion MRI", *NeuroImage*, vol. 51, no. 2, pp. 743–751, Jun. 2010. DOI: 10.1016/j.neuroimage.2010.02.041.

[116] D. A. Raffelt, R. E. Smith, G. R. Ridgway, J.-D. Tournier, D. N. Vaughan, S. Rose, R. Henderson, and A. Connelly, "Connectivity-based fixel enhancement: Whole-brain statistical analysis of diffusion MRI measures in the presence of crossing fibres", *NeuroImage*, vol. 117, pp. 40–55, Aug. 2015. DOI: 10.1016/j.neuroimage.2015.05.039.

[117] F. Dell'Acqua, A. Simmons, S. C. Williams, and M. Catani, "Can spherical deconvolution provide more information than fiber orientations? Hindrance modulated orientational anisotropy, a true-tract specific index to characterize white matter diffusion", *Human Brain Mapping*, vol. 34, no. 10, pp. 2464–2483, Oct. 2013. DOI: 10.1002/hbm.22080.

[118] B. Jeurissen, J.-D. Tournier, T. Dhollander, A. Connelly, and J. Sijbers, "Multi-tissue constrained spherical deconvolution for improved analysis of multi-shell diffusion MRI data", *NeuroImage*, vol. 103, pp. 411–426, Dec. 2014. DOI: 10.1016/j.neuroimage.2014.07.061.

[119] T. E. Conturo, N. F. Lori, T. S. Cull, E. Akbudak, A. Z. Snyder, J. S. Shimony, R. C. McKinstry, H. Burton, and M. E. Raichle, "Tracking neuronal fiber pathways in the living human brain", *Proc. Natl. Acad. Sci. USA*, vol. 96, no. 18, pp. 10 422–10 427, 1999.

[120] S. Mori, B. J. Crain, V. P. Chacko, and P. C. Van Zijl, "Three-dimensional tracking of axonal projections in the brain by magnetic resonance imaging", *Annals of Neurology*, vol. 45, no. 2, pp. 265–269, 1999.

[121] D. K. Jones, A. Simmons, S. C. Williams, and M. A. Horsfield, "Non-invasive assessment of axonal fiber connectivity in the human brain via diffusion tensor MRI", *Magn. Reson. Med.*, vol. 42, no. 1, pp. 37–41, Jul. 1999.

[122] P. J. Basser, S. Pajevic, C. Pierpaoli, J. Duda, and A. Aldroubi, "In vivo fiber tractography using DT-MRI data", *Magn. Reson. Med.*, vol. 44, no. 4, pp. 625–632, 2000.

[123] C. Poupon, C. Clark, V. Frouin, J. Régis, I. Bloch, D. L. Bihan, and J.-F. Mangin, "Regularization of diffusion-based direction maps for the tracking of brain white matter fascicles", *NeuroImage*, vol. 12, no. 2, pp. 184–195, Aug. 2000. DOI: 10.1006/nimg.2000.0607.

[124] J.-D. Tournier, F. Calamante, and A. Connelly, "MRtrix: Diffusion tractography in crossing fiber regions", *International Journal of Imaging Systems and Technology*, vol. 22, no. 1, pp. 53–66, Feb. 2012. DOI: 10.1002/ima.22005.

[125] M. A. Koch, D. G. Norris, and M. Hund-Georgiadis, "An investigation of functional and anatomical connectivity using magnetic resonance imaging", *NeuroImage*, vol. 16, no. 1, pp. 241–50, May 2002. DOI: 10.1006/nimg.2001.1052.

[126] G. J. M. Parker, H. A. Haroon, and C. A. M. Wheeler-Kingshott, "A framework for a streamline-based probabilistic index of connectivity (PICo) using a structural interpretation of MRI diffusion measurements", *Journal of Magn. Reson. Imaging*, vol. 18, no. 2, pp. 242–254, 2003.

[127] J.-D. Tournier, F. Calamante, D. G. Gadian, and A. Connelly, "Diffusion-weighted magnetic resonance imaging fibre tracking using a front evolution algorithm", *NeuroImage*, vol. 20, no. 1, pp. 276–88, Sep. 2003.

[128] D. K. Jones and C. Pierpaoli, "Confidence mapping in diffusion tensor magnetic resonance imaging tractography using a bootstrap approach", *Magn. Reson. Med.*, vol. 53, no. 5, pp. 1143–1149, May 2005. DOI: 10.1002/mrm.20466.

[129] M. Lazar and A. L. Alexander, "Bootstrap white matter tractography (BOOT-TRAC)", *NeuroImage*, vol. 24, no. 2, pp. 524–32, Jan. 2005. DOI: 10.1016/j.neuroimage.2004.08.050.

[130] O. Friman, G. Farnebäck, and C.-F. Westin, "A Bayesian approach for stochastic white matter tractography", *IEEE Trans. Med. Imag.*, vol. 25, no. 8, pp. 965–978, 2006.

[131] D. K. Jones, "Tractography gone wild: Probabilistic fibre tracking using the wild bootstrap with diffusion tensor MRI", *IEEE Trans. Med. Imag.*, vol. 27, no. 9, pp. 1268–1274, 2008.

[132] D. M. Morris, K. V. Embleton, and G. J. Parker, "Probabilistic fibre tracking: Differentiation of connections from chance events", *NeuroImage*, vol. 42, no. 4, pp. 1329–1339, Oct. 2008. DOI: 10.1016/j.neuroimage.2008.06.012.

[133] J.-D. Tournier, F. Calamante, and A. Connelly, "Improved probabilistic streamlines tractography by 2nd order integration over fibre orientation distributions", in *Proceedings of the International Society for Magnetic Resonance in Medicine*, 2010, p. 1670.

[134] B. Jeurissen, A. Leemans, D. K. Jones, J.-D. Tournier, and J. Sijbers, "Probabilistic fiber tracking using the residual bootstrap with constrained spherical deconvolution", *Human Brain Mapping*, vol. 32, no. 3, pp. 461–479, 2011. DOI: 10.1002/hbm.21032.

[135] G. J. M. Parker, C. A. M. Wheeler-Kingshott, and G. J. Barker, "Estimating distributed anatomical connectivity using fast marching methods and diffusion tensor imaging", *IEEE Trans. Med. Imag.*, vol. 21, no. 5, pp. 505–12, May 2002. DOI: 10.1109/TMI.2002.1009386.

[136] J. S. Campbell, K. Siddiqi, V. V. Rymar, A. F. Sadikot, and G. B. Pike, "Flow-based fiber tracking with diffusion tensor and q-ball data: Validation and comparison to principal diffusion direction techniques", *NeuroImage*, vol. 27, no. 4, pp. 725–736, Oct. 2005. DOI: 10.1016/j.neuroimage.2005.05.014.

[137] S. Jbabdi, P. Bellec, R. Toro, J. Daunizeau, M. Pélégrini-Issac, and H. Benali, "Accurate anisotropic fast marching for diffusion-based geodesic tractography", *International Journal of Biomedical Imaging*, vol. 2008, no. 1, p. 320 195, 2008.

[138] M. Schober, N. Kasenburg, A. Feragen, P. Hennig, and S. Hauberg, "Probabilistic shortest path tractography in DTI using Gaussian process ODE solvers", in *Medical Image Computing and Computer-Assisted Intervention – MICCAI 2014*, ser. Lecture Notes in Computer Science Pt 3, P. Golland, N. Hata, C. Barrillot, J. Hornegger, and R. Howe, Eds., vol. 8675, Boston, MA, USA, 2014, pp. 265–272. DOI: 10.1007/978-3-319-10443-0_34.

[139] A. Fuster, T. Dela Haije, A. Tristán-Vega, B. Plantinga, C.-F. Westin, and L. Florack, "Adjugate diffusion tensors for geodesic tractography in white matter", *Journal of Mathematical Imaging and Vision*, vol. 54, no. 1, pp. 1–14, Jan. 2016. DOI: 10.1007/s10851-015-0586-8.

[140] J.-F. Mangin, C. Poupon, Y. Cointepas, D. Rivière, D. Papadopoulos-Orfanos, C. A. Clark, J. Régis, and D. L. Bihan, "A framework based on spin glass models for the inference of anatomical connectivity from diffusion-weighted MR data - a technical review", *NMR in Biomedicine*, vol. 15, no. 7-8, pp. 481–492, 2002. DOI: 10.1002/nbm.780.

[141] B. W. Kreher, I. Mader, and V. G. Kiselev, "Gibbs tracking: A novel approach for the reconstruction of neuronal pathways", *Magn. Reson. Med.*, vol. 60, no. 4, pp. 953–963, Oct. 2008. DOI: 10.1002/mrm.21749.

[142] P. Fillard, C. Poupon, and J.-F. Mangin, "A novel global tractography algorithm based on an adaptive spin glass model", in *Medical Image Computing and Computer-Assisted Intervention – MICCAI 2009*, ser. Lecture Notes in Computer Science, G.-Z. Yang, D. Hawkes, D. Rueckert, A. Noble, and C. Taylor, Eds., vol. 5761, London, UK: Springer Berlin Heidelberg, 2009, pp. 927–934. DOI: 10.1007/978-3-642-04268-3_114.

[143] M. Reisert, I. Mader, C. Anastasopoulos, M. Weigel, S. Schnell, and V. Kiselev, "Global fiber reconstruction becomes practical", *NeuroImage*, vol. 54, no. 2, pp. 955–962, Jan. 2011. DOI: 10.1016/j.neuroimage.2010.09.016.

[144] A. Lemkaddem, D. Skiöldebrand, A. Dal Palù, J.-P. Thiran, and A. Daducci, "Global tractography with embedded anatomical priors for quantitative connectivity analysis", *Frontiers in Neurology*, vol. 5, Nov. 2014. DOI: 10.3389/fneur.2014.00232.

[145] M. Reisert, V. Kiselev, B. Dihtal, E. Kellner, and D. Novikov, "MesoFT: unifying diffusion modelling and fiber tracking", in *Medical Image Computing and Computer-Assisted Intervention – MICCAI 2014*, ser. Lecture Notes in Computer Science, P. Golland, N. Hata, C. Barillot, J. Hornegger, and R. Howe, Eds., vol. 8675, Boston, MA, USA: Springer International Publishing, 2014, pp. 201–208. DOI: 10.1007/978-3-319-10443-0_26.

[146] J.-F. Mangin, P. Fillard, Y. Cointepas, D. L. Bihan, V. Frouin, and C. Poupon, "Toward global tractography", *NeuroImage*, vol. 80, pp. 290–296, Oct. 2013. DOI: 10.1016/j.neuroimage.2013.04.009.

[147] P. Hagmann, M. Kurant, X. Gigandet, P. Thiran, V. J. Wedeen, R. Meuli, and J.-P. Thiran, "Mapping human whole-brain structural networks with diffusion MRI", *PLoS ONE*, vol. 2, no. 7, O. Sporns, Ed., e597, Jul. 2007. DOI: 10.1371/journal.pone.0000597.

[148] P. Hagmann, L. Cammoun, X. Gigandet, R. Meuli, C. J. Honey, V. J. Wedeen, and O. Sporns, "Mapping the structural core of human cerebral cortex", *PLoS Biology*, vol. 6, no. 7, K. J. Friston, Ed., e159, Jul. 2008. DOI: 10.1371/journal.pbio.0060159.

[149] P. Hagmann, L. Cammoun, X. Gigandet, S. Gerhard, P. E. Grant, V. J. Wedeen, R. Meuli, J.-P. Thiran, C. J. Honey, and O. Sporns, "MR connectomics: Principles and challenges", *Journal of Neuroscience Methods*, vol. 194, no. 1, pp. 34–45, 2010.

[150] E. Bullmore and O. Sporns, "Complex brain networks: Graph theoretical analysis of structural and functional systems", *Nature Reviews Neuroscience*, vol. 10, no. 3, pp. 186–198, Mar. 2009. DOI: 10.1038/nrn2575.

[151] M. Rubinov and O. Sporns, "Complex network measures of brain connectivity: Uses and interpretations", *NeuroImage*, vol. 52, no. 3, K. J. Friston, Ed., pp. 1059–1069, Sep. 2010. DOI: 10.1016/j.neuroimage.2009.10.003.

[152] O. Sporns, "The human connectome: A complex network", *Annals of the New York Academy of Sciences*, vol. 1224, no. 1, pp. 109–25, Apr. 2011. DOI: 10.1111/j.1749-6632.2010.05888.x.

[153] ——, "From simple graphs to the connectome: Networks in neuroimaging", *NeuroImage*, vol. 62, no. 2, pp. 881–6, Aug. 2012. DOI: 10.1016/j.neuroimage.2011.08.085.

[154] D. K. Jones, T. R. Knösche, and R. Turner, "White matter integrity, fiber count, and other fallacies: The do's and don'ts of diffusion MRI", *NeuroImage*, vol. 73, pp. 239–254, Jun. 2013. DOI: 10.1016/j.neuroimage.2012.06.081.

[155] A. J. Sherbondy, R. F. Dougherty, R. Ananthanarayanan, D. S. Modha, and B. A. Wandell, "Think global, act local; projectome estimation with BlueMatter", in *Medical Image Computing and Computer-Assisted Intervention – MICCAI 2009*, ser. Lecture Notes in Computer Science, G.-Z. Yang, D. Hawkes, D. Rueckert, A. Noble, and C. Taylor, Eds., vol. 5761, London, UK, 2009, pp. 861–868. DOI: 10.1007/978-3-642-04268-3_106.

[156] A. J. Sherbondy, M. C. Rowe, and D. C. Alexander, "Microtrack: An algorithm for concurrent projectome and microstructure estimation", in *Medical Image Computing and Computer-Assisted Intervention – MICCAI 2010*, ser. Lecture Notes in Computer Science, T. Jiang, N. Navab, J. P. W. Pluim, and M. A. Viergever, Eds., vol. 6361, Springer Berlin Heidelberg, 2010, pp. 183–190. DOI: 10.1007/978-3-642-15705-9_23.

[157] R. E. Smith, J.-D. Tournier, F. Calamante, and A. Connelly, "SIFT: spherical-deconvolution informed filtering of tractograms", *NeuroImage*, vol. 67, pp. 298–312, Feb. 2013. DOI: 10.1016/j.neuroimage.2012.11.049.

[158] ——, "SIFT2: enabling dense quantitative assessment of brain white matter connectivity using streamlines tractography", *NeuroImage*, vol. 119, pp. 338–351, Oct. 2015. DOI: 10.1016/j.neuroimage.2015.06.092.

[159] A. Daducci, A. Dal Palù, L. Alia, and J.-P. Thiran, "COMMIT: convex optimization modeling for micro-structure informed tractography", *IEEE Trans. Med. Imag.*, pp. 246–257, 2014. DOI: 10.1109/tmi.2014.2352414.

[160] F. Pestilli, J. D. Yeatman, A. Rokem, K. N. Kay, and B. A. Wandell, "Evaluation and statistical inference for human connectomes", *Nature Methods*, vol. 11, no. 10, pp. 1058–1063, Sep. 2014. DOI: 10.1038/nmeth.3098.

[161] R. E. Smith, J.-D. Tournier, F. Calamante, and A. Connelly, "The effects of SIFT on the reproducibility and biological accuracy of the structural connectome", *NeuroImage*, vol. 104, pp. 253–265, Jan. 2015. DOI: 10.1016/j.neuroimage.2014.10.004.

[162] ——, "Anatomically-constrained tractography: Improved diffusion MRI streamlines tractography through effective use of anatomical information", *NeuroImage*, vol. 62, no. 3, pp. 1924–1938, Sep. 2012. DOI: 10.1016/j.neuroimage.2012.06.005.

[163] L. J. O'Donnell, A. J. Golby, and C.-F. Westin, "Fiber clustering versus the parcellation-based connectome", *NeuroImage*, vol. 80, pp. 283–289, 2013.

[164] D. Wassermann, N. Makris, Y. Rathi, M. Shenton, R. Kikinis, M. Kubicki, and C.-F. Westin, "On describing human white matter anatomy: The white matter query language", in *Medical Image Computing and Computer-Assisted Intervention – MICCAI 2013*, ser. Lecture Notes in Computer Science, K. Mori, I. Sakuma, Y. Sato, C. Barillot, and N. Navab, Eds., vol. 8149, Nagoya, Japan: Springer Berlin Heidelberg, 2013, pp. 647–654. DOI: 10.1007/978-3-642-40811-3_81.

[165] F. Dell'Acqua, L. Lacerda, R. Barrett, L. D'Anna, S. Tsermentseli, L. Goldstein, and M. Catani, "MegaTrack: a fast and effective strategy for group comparison and supervised analysis of large-scale tractography datasets", in *International Society for Magnetic Resonance in Medicine (ISMRM) 23th Annual Meeting & Exhibtion*, vol. 23, Toronto, Ontario, Canada, May 2015, p. 2843.

[166] M. Catani and M. Thiebaut de Schotten, "A diffusion tensor imaging tractography atlas for virtual in vivo dissections", *Cortex*, vol. 44, no. 8, pp. 1105–1132, Sep. 2008. DOI: 10.1016/j.cortex.2008.05.004.

[167] L. J. O'Donnell and C.-F. Westin, "Automatic tractography segmentation using a high-dimensional white matter atlas", *IEEE Trans. Med. Imag.*, vol. 26, no. 11, pp. 1562–75, 2007.

[168] M. Maddah, W. E. L. Grimson, S. K. Warfield, and W. M. Wells, "A unified framework for clustering and quantitative analysis of white matter fiber tracts", *Med. Image Anal.*, vol. 12, no. 2, pp. 191–202, 2008.

[169] D. Wassermann, L. Bloy, E. Kanterakis, R. Verma, and R. Deriche, "Unsupervised white matter fiber clustering and tract probability map generation: Applications of a Gaussian process framework for white matter fibers", *NeuroImage*, vol. 51, no. 1, pp. 228–41, 2010.

[170] P. Guevara, C. Poupon, D. Rivière, Y. Cointepas, M. Descoteaux, B. Thirion, and J.-F. Mangin, "Robust clustering of massive tractography datasets", *NeuroImage*, vol. 54, no. 3, pp. 1975–93, Mar. 2011. DOI: 10.1016/j.neuroimage.2010.10.028.

[171] E. Visser, E. H. J. Nijhuis, J. K. Buitelaar, and M. P. Zwiers, "Partition-based mass clustering of tractography streamlines", *NeuroImage*, vol. 54, no. 1, pp. 303–12, Jan. 2011. DOI: 10.1016/j.neuroimage.2010.07.038.

[172] Y. Xia, Turken, U., S. L. Whitfield-Gabrieli, and J. D. Gabrieli, "Knowledge-based classification of neuronal fibers in entire brain", in *Medical Image Computing and Computer-Assisted Intervention – MICCAI 2005*, ser. Lecture Notes in Computer Science, J. S. Duncan and G. Gerig, Eds., vol. 3749, Palm Springs, CA, USA: Springer Berlin Heidelberg, 2005, pp. 205–212. DOI: 10.1007/11566465_26.

[173] U. Ziyan, M. R. Sabuncu, W. E. L. Grimson, and C.-F. Westin, "Consistency clustering: A robust algorithm for group-wise registration, segmentation and automatic atlas construction in diffusion MRI", *International journal of computer vision*, vol. 85, no. 3, pp. 279–290, Jan. 2009. DOI: 10.1007/s11263-009-0217-1.

[174] H. Li, Z. Xue, L. Guo, T. Liu, J. Hunter, and S. T. C. Wong, "A hybrid approach to automatic clustering of white matter fibers", *NeuroImage*, vol. 49, no. 2, pp. 1249–58, Jan. 2010. DOI: 10.1016/j.neuroimage.2009.08.017.

[175] P. Guevara, D. Duclap, C. Poupon, L. Marrakchi-Kacem, P. Fillard, D. Le Bihan, M. Leboyer, J. Houenou, and J.-F. Mangin, "Automatic fiber bundle segmentation in massive tractography datasets using a multi-subject bundle atlas", *NeuroImage*, vol. 61, no. 4, pp. 1083–99, 2012.

[176] Q. Wang, P.-T. Yap, G. Wu, and D. Shen, "Application of neuroanatomical features to tractography clustering", *Human Brain Mapping*, vol. 34, no. 9, pp. 2089–2102, Sep. 2013. DOI: 10.1002/hbm.22051.

[177] D. Vercruysse, D. Christiaens, F. Maes, S. Sunaert, and P. Suetens, "Fiber bundle segmentation using spectral embedding and supervised learning", in *Computational Diffusion MRI – MICCAI Workshop*, L. O'Donnell, G. Nedjati-Gilani, Y. Rathi, M. Reisert, and T. Schneider, Eds., ser. Mathematics and Visualization, Cambridge, MA, USA: Springer International Publishing, Sep. 2014, pp. 103–114. DOI: 10.1007/978-3-319-11182-7_10.

[178] D. C. Alexander, "Multiple-fiber reconstruction algorithms for diffusion MRI", *Annals of the New York Academy of Sciences*, vol. 1064, no. 1, pp. 113–133, Dec. 2005. DOI: 10.1196/annals.1340.018.

[179] E. Caruyer, A. Daducci, M. Descoteaux, J.-C. Houde, J.-P. Thiran, and R. Verma, "Phantomas: A flexible software library to simulate diffusion MR phantoms", in *International Society for Magnetic Resonance in Medicine (ISMRM) 22th Joint Annual Meeting ISMRM-ESMRMB*, vol. 22, Milan, Italy, May 2014, p. 2666.

[180] E. Fieremans, Y. D. Deene, S. Delputte, M. S. Özdemir, Y. D'Asseler, J. Vlassenbroeck, K. Deblaere, E. Achten, and I. Lemahieu, "Simulation and experimental verification of the diffusion in an anisotropic fiber phantom", *Journal of Magnetic Resonance*, vol. 190, no. 2, pp. 189–199, Feb. 2008. DOI: 10.1016/j.jmr.2007.10.014.

[181] M. Hall and D. Alexander, "Convergence and parameter choice for Monte-Carlo simulations of diffusion MRI", *IEEE Trans. Med. Imaging*, vol. 28, no. 9, pp. 1354–1364, Sep. 2009. DOI: 10.1109/tmi.2009.2015756.

[182] B. A. Landman, J. A. D. Farrell, S. A. Smith, D. S. Reich, P. A. Calabresi, and P. C. M. van Zijl, "Complex geometric models of diffusion and relaxation in healthy and damaged white matter", *NMR in Biomedicine*, vol. 32, no. 2, pp. 152–162, 2010. DOI: 10.1002/nbm.1437.

[183] C.-H. Yeh, B. Schmitt, D. L. Bihan, J.-R. Li-Schlittgen, C.-P. Lin, and C. Poupon, "Diffusion microscopist simulator: A general Monte Carlo simulation system for diffusion magnetic resonance imaging", *PLoS ONE*, vol. 8, no. 10, W. Zhan, Ed., e76626, Oct. 2013. DOI: 10.1371/journal.pone.0076626.

[184] T. G. Close, J.-D. Tournier, F. Calamante, L. A. Johnston, I. Mareels, and A. Connelly, "A software tool to generate simulated white matter structures for the assessment of fibre-tracking algorithms", *NeuroImage*, vol. 47, no. 4, pp. 1288–1300, Oct. 2009. DOI: 10.1016/j.neuroimage.2009.03.077.

[185] M.-A. Côté, G. Girard, A. Boré, E. Garyfallidis, J.-C. Houde, and M. Descoteaux, "Tractometer: Towards validation of tractography pipelines", *Med. Image Anal.*, vol. 17, no. 7, pp. 844–857, Oct. 2013. DOI: 10.1016/j.media.2013.03.009.

[186] A. Daducci, E. Caruyer, M. Descoteaux, J.-C. Houde, and J.-P. Thiran, Eds., *IEEE International Symposium on Biomedical Imaging (ISBI): HARDI Reconstruction Challenge*, 2013.

[187] E. Fieremans, Y. D. Deene, S. Delputte, M. S. Özdemir, E. Achten, and I. Lemahieu, "The design of anisotropic diffusion phantoms for the validation of diffusion weighted magnetic resonance imaging", *Physics in Medicine and Biology*, vol. 53, no. 19, pp. 5405–5419, Sep. 2008. DOI: 10.1088/0031-9155/53/19/009.

[188] P. Pullens, A. Roebroeck, and R. Goebel, "Ground truth hardware phantoms for validation of diffusion-weighted MRI applications", *J. Magn. Reson. Imaging*, vol. 32, no. 2, pp. 482–488, Jul. 2010. DOI: 10.1002/jmri.22243.

[189] N. Yanasak and J. Allison, "Use of capillaries in the construction of an MRI phantom for the assessment of diffusion tensor imaging: Demonstration of performance", *Magn. Reson. Imaging*, vol. 24, no. 10, pp. 1349–1361, Dec. 2006. DOI: 10.1016/j.mri.2006.08.001.

[190] P. Fillard, M. Descoteaux, A. Goh, S. Gouttard, B. Jeurissen, J. Malcolm, A. Ramirez-Manzanares, M. Reisert, K. Sakaie, F. Tensaouti, T. Yo, J.-F. Mangin, and C. Poupon, "Quantitative evaluation of 10 tractography algorithms on a realistic diffusion MR phantom", *NeuroImage*, vol. 56, no. 1, pp. 220–234, May 2011. DOI: 10.1016/j.neuroimage.2011.01.032.

[191] E. Fieremans, "Physical hardware phantoms for the validation of diffusion MRI", in *International Society for Magnetic Resonance in Medicine (ISMRM) 24th Annual Meeting & Exhibtion*, vol. 24, Singapore, May 2016.

[192] M. Helmstaedter, K. L. Briggman, S. C. Turaga, V. Jain, H. S. Seung, and W. Denk, "Connectomic reconstruction of the inner plexiform layer in the mouse retina", *Nature*, vol. 500, no. 7461, pp. 168–174, Aug. 2013. DOI: 10.1038/nature12346.

[193] M. Axer, K. Amunts, D. Grässel, C. Palm, J. Dammers, H. Axer, U. Pietrzyk, and K. Zilles, "A novel approach to the human connectome: Ultra-high resolution mapping of fiber tracts in the brain", *NeuroImage*, vol. 54, no. 2, pp. 1091–1101, Jan. 2011. DOI: 10.1016/j.neuroimage.2010.08.075.

[194] H. Wang, J. Zhu, M. Reuter, L. N. Vinke, A. Yendiki, D. A. Boas, B. Fischl, and T. Akkin, "Cross-validation of serial optical coherence scanning and diffusion tensor imaging: A study on neural fiber maps in human medulla oblongata", *NeuroImage*, vol. 100, pp. 395–404, Oct. 2014. DOI: 10.1016/j.neuroimage.2014.06.032.

[195] K. Chung, J. Wallace, S.-Y. Kim, S. Kalyanasundaram, A. S. Andalman, T. J. Davidson, J. J. Mirzabekov, K. A. Zalocusky, J. Mattis, A. K. Denisin, S. Pak, H. Bernstein, C. Ramakrishnan, L. Grosenick, V. Gradinaru, and K. Deisseroth, "Structural and molecular interrogation of intact biological systems", *Nature*, vol. 497, no. 7449, pp. 332–337, Apr. 2013. DOI: 10.1038/nature12107.

[196] E. Underwood, "Tissue imaging method makes everything clear", *Science*, vol. 340, no. 6129, pp. 131–132, Apr. 2013. DOI: 10.1126/science.340.6129.131.

[197] H. Shen, "See-through brains clarify connections", *Nature*, vol. 496, no. 7444, pp. 151–151, Apr. 2013. DOI: 10.1038/496151a.

[198] T. B. Leergaard, N. S. White, A. de Crespigny, I. Bolstad, H. D'Arceuil, J. G. Bjaalie, and A. M. Dale, "Quantitative histological validation of diffusion MRI fiber orientation distributions in the rat brain", *PLoS ONE*, vol. 5, no. 1, P. A. Valdes-Sosa, Ed., e8595, Jan. 2010. DOI: 10.1371/journal.pone.0008595.

[199] K. Schilling, V. Janve, Y. Gao, I. Stepniewska, B. A. Landman, and A. W. Anderson, "Comparison of 3d orientation distribution functions measured with confocal microscopy and diffusion MRI", *NeuroImage*, vol. 129, pp. 185–197, Apr. 2016. DOI: 10.1016/j.neuroimage.2016.01.022.

[200] Y. Wang, Q. Wang, J. P. Haldar, F.-C. Yeh, M. Xie, P. Sun, T.-W. Tu, K. Trinkaus, R. S. Klein, A. H. Cross, and S.-K. Song, "Quantification of increased cellularity during inflammatory demyelination", *Brain*, vol. 134, no. 12, pp. 3590–3601, Dec. 2011. DOI: 10.1093/brain/awr307.

[201] D. Barazany, P. J. Basser, and Y. Assaf, "In vivo measurement of axon diameter distribution in the corpus callosum of rat brain", *Brain*, vol. 132, no. 5, pp. 1210–1220, Apr. 2009. DOI: 10.1093/brain/awp042.

[202] D. C. Van Essen, S. M. Smith, D. M. Barch, T. E. Behrens, E. Yacoub, and K. Ugurbil, "The WU-Minn human connectome project: An overview", *NeuroImage*, vol. 80, pp. 62–79, Oct. 2013. DOI: 10.1016/j.neuroimage.2013.05.041.

[203] C.-P. Lin, W.-Y. I. Tseng, H.-C. Cheng, and J.-H. Chen, "Validation of diffusion tensor magnetic resonance axonal fiber imaging with registered manganese-enhanced optic tracts", *NeuroImage*, vol. 14, no. 5, pp. 1035–1047, Nov. 2001. DOI: 10.1006/nimg.2001.0882.

[204] C.-P. Lin, V. J. Wedeen, J.-H. Chen, C. Yao, and W.-Y. I. Tseng, "Validation of diffusion spectrum magnetic resonance imaging with manganese-enhanced rat optic tracts and ex vivo phantoms", *NeuroImage*, vol. 19, no. 3, pp. 482–495, Jul. 2003. DOI: 10.1016/s1053-8119(03)00154-x.

[205] T. B. Dyrby, L. V. Søgaard, G. J. Parker, D. C. Alexander, N. M. Lind, W. F. Baaré, A. Hay-Schmidt, N. Eriksen, B. Pakkenberg, O. B. Paulson, and J. Jelsing, "Validation of in vitro probabilistic tractography", *NeuroImage*, vol. 37, no. 4, pp. 1267–1277, Oct. 2007. DOI: 10.1016/j.neuroimage.2007.06.022.

[206] J. D. Schmahmann, D. N. Pandya, R. Wang, G. Dai, H. E. D'Arceuil, A. J. de Crespigny, and V. J. Wedeen, "Association fibre pathways of the brain: Parallel observations from diffusion spectrum imaging and autoradiography", *Brain*, vol. 130, no. 3, pp. 630–653, Feb. 2007. DOI: 10.1093/brain/awl359.

[207] Y. Gao, A. S. Choe, I. Stepniewska, X. Li, M. J. Avison, and A. W. Anderson, "Validation of DTI tractography-based measures of primary motor area connectivity in the squirrel monkey brain", *PLoS ONE*, vol. 8, no. 10, C. Beaulieu, Ed., e75065, Oct. 2013. DOI: 10.1371/journal.pone.0075065.

[208] A. Yendiki, "Validation of white-matter pathways reconstructed with diffusion tractography", in *International Society for Magnetic Resonance in Medicine (ISMRM) 24th Annual Meeting & Exhibtion*, vol. 24, Singapore, May 2016.

[209] F. Dell'Acqua and M. Catani, "Structural human brain networks: Hot topics in diffusion tractography", *Current Opinion in Neurology*, vol. 25, pp. 375–383, 4 Aug. 2012. DOI: 10.1097/wco.0b013e328355d544.

[210] S. Jbabdi and H. Johansen-Berg, "Tractography: Where do we go from here?", *Brain Connectivity*, vol. 1, no. 3, pp. 169–183, Sep. 2011. DOI: 10.1089/brain.2011.0033.

[211] Y. Assaf, D. C. Alexander, D. K. Jones, A. Bizzi, T. E. Behrens, C. A. Clark, Y. Cohen, T. B. Dyrby, P. S. Huppi, T. R. Knoesche, D. LeBihan, G. J. Parker, and C. Poupon, "The CONNECT project: Combining macro- and micro-structure", *NeuroImage*, vol. 80, pp. 273–282, Oct. 2013. DOI: 10.1016/j.neuroimage.2013.05.055.

[212] P. J. Green, "Reversible jump Markov chain Monte Carlo computation and Bayesian model determination", *Biometrika*, vol. 82, no. 4, pp. 711–732, 1995. DOI: 10.1093/biomet/82.4.711.

[213] Y. Zhang, M. Brady, and S. Smith, "Segmentation of brain MR images through a hidden markov random field model and the expectation-maximization algorithm", *IEEE Trans. Med. Imag.*, vol. 20, no. 1, pp. 45–57, 2001. DOI: 10.1109/42.906424.

[214] M. F. Glasser, S. N. Sotiropoulos, J. A. Wilson, T. S. Coalson, B. Fischl, J. L. Andersson, J. Xu, S. Jbabdi, M. Webster, J. R. Polimeni, D. C. V. Essen, and M. Jenkinson, "The minimal preprocessing pipelines for the Human Connectome Project", *NeuroImage*, vol. 80, pp. 105–124, Oct. 2013. DOI: 10.1016/j.neuroimage.2013.04.127.

[215] J. L. Andersson, S. Skare, and J. Ashburner, "How to correct susceptibility distortions in spin-echo echo-planar images: Application to diffusion tensor imaging", *NeuroImage*, vol. 20, no. 2, pp. 870–888, Oct. 2003. DOI: 10.1016/s1053-8119(03)00336-7.

[216] S. M. Smith, M. Jenkinson, M. W. Woolrich, C. F. Beckmann, T. E. Behrens, H. Johansen-Berg, P. R. Bannister, M. D. Luca, I. Drobnjak, D. E. Flitney, R. K. Niazy, J. Saunders, J. Vickers, Y. Zhang, N. D. Stefano, J. M. Brady, and P. M. Matthews, "Advances in functional and structural MR image analysis and implementation as FSL", *NeuroImage*, vol. 23, S208–S219, Jan. 2004. DOI: 10.1016/j.neuroimage.2004.07.051.

[217] P. F. Neher, B. Stieltjes, M. Reisert, I. Reicht, H.-P. Meinzer, and K. H. Fritzsche, "MITK global tractography", in *Medical Imaging 2012: Image Processing*, D. R. Haynor and S. Ourselin, Eds., ser. Proc. SPIE, vol. 8314, SPIE, Feb. 2012, p. 83144D. DOI: 10.1117/12.911215.

[218] K. H. Fritzsche, P. F. Neher, I. Reicht, T. van Bruggen, C. Goch, M. Reisert, M. Nolden, S. Zelzer, H.-P. Meinzer, and B. Stieltjes, "MITK diffusion imaging", *Methods of Information in Medicine*, vol. 51, no. 5, pp. 441–448, 2012. DOI: 10.3414/me11-02-0031.

[219] J.-C. Houde, E. Caruyer, A. Daducci, and M. Descoteaux, "How should tractography go forward? A Tractometer evaluation of local reconstruction and tracking", in *International Society for Magnetic Resonance in Medicine (ISMRM) 22th Joint Annual Meeting ISMRM-ESMRMB*, vol. 22, Milan, Italy, May 2014, p. 273.

[220] G. Girard, K. Whittingstall, R. Deriche, and M. Descoteaux, "Towards quantitative connectivity analysis: Reducing tractography biases", *NeuroImage*, vol. 98, pp. 266–278, Sep. 2014. DOI: 10.1016/j.neuroimage.2014.04.074.

[221] T. Dhollander, L. Emsell, W. V. Hecke, F. Maes, S. Sunaert, and P. Suetens, "Track Orientation Density Imaging (TODI) and Track Orientation Distribution (TOD) based tractography", *NeuroImage*, vol. 94, pp. 312–336, Jul. 2014. DOI: 10.1016/j.neuroimage.2013.12.047.

[222] H. Gudbjartsson and S. Patz, "The Rician distribution of noisy MRI data", *Magn. Reson. Med.*, vol. 34, no. 6, pp. 910–914, Dec. 1995. DOI: 10.1002/mrm.1910340618.

[223] S. Aja-Fernández, G. Vegas-Sánchez-Ferrero, and A. Tristán-Vega, "Noise estimation in parallel MRI: GRAPPA and SENSE", *Magn. Reson. Imaging*, vol. 32, no. 3, pp. 281–290, Apr. 2014. DOI: 10.1016/j.mri.2013.12.001.

[224] S. N. Sotiropoulos, S. Jbabdi, J. Xu, J. L. Andersson, S. Moeller, E. J. Auerbach, M. F. Glasser, M. Hernandez, G. Sapiro, M. Jenkinson, D. A. Feinberg, E. Yacoub, C. Lenglet, D. C. V. Essen, K. Ugurbil, and T. E.

Behrens, "Advances in diffusion MRI acquisition and processing in the human connectome project", *NeuroImage*, vol. 80, pp. 125–143, Oct. 2013. DOI: 10.1016/j.neuroimage.2013.05.057.

[225] J. Veraart, E. Fieremans, and D. S. Novikov, "Diffusion MRI noise mapping using random matrix theory", *Magn. Reson. Med.*, n/a–n/a, Nov. 2015. DOI: 10.1002/mrm.26059.

[226] H. Li, T. Liu, G. Young, L. Guo, and S. Wong, "Brain tissue segmentation based on DWI/DTI data", in *3rd IEEE International Symposium on Biomedical Imaging: Macro to Nano*, IEEE, 2006, pp. 57–60. DOI: 10.1109/isbi.2006.1624851.

[227] C.-F. Lu, P.-S. Wang, Y.-C. Chou, H.-C. Li, B.-W. Soong, and Y.-T. Wu, "Segmentation of diffusion-weighted brain images using expectation maximization algorithm initialized by hierarchical clustering", in *30th Annual International Conference of the IEEE Engineering in Medicine and Biology Society*, IEEE, Aug. 2008, pp. 5502–5505. DOI: 10.1109/iembs.2008.4650460.

[228] O. Sporns, "Theoretical neuroanatomy: Relating anatomical and functional connectivity in graphs and cortical connection matrices", *Cerebral Cortex*, vol. 10, no. 2, pp. 127–141, Feb. 2000. DOI: 10.1093/cercor/10.2.127.

[229] D. B. Chklovskii, T. Schikorski, and C. F. Stevens, "Wiring optimization in cortical circuits", *Neuron*, vol. 34, no. 3, pp. 341–347, Apr. 2002. DOI: 10.1016/s0896-6273(02)00679-7.

[230] M. Kaiser and C. C. Hilgetag, "Nonoptimal component placement, but short processing paths, due to long-distance projections in neural systems", *PLoS Computational Biology*, vol. 2, no. 7, e95, 2006. DOI: 10.1371/journal.pcbi.0020095.

[231] A. Raj and Y. Chen, "The wiring economy principle: Connectivity determines anatomy in the human brain", *PLoS ONE*, vol. 6, no. 9, G. G. de Polavieja, Ed., e14832, Sep. 2011. DOI: 10.1371/journal.pone.0014832.

[232] C. Ding, T. Li, and M. Jordan, "Convex and semi-nonnegative matrix factorizations", *IEEE Trans. Pattern Anal. Machine Intell.*, vol. 32, no. 1, pp. 45–55, Jan. 2010. DOI: 10.1109/tpami.2008.277.

[233] G. J. Parker, "Probabilistic fiber tracking", in *Diffusion MRI: Theory, methods, and applications*, D. K. Jones, Ed., Oxford University Press, 2010, pp. 396–408.

[234] M. Cabezas, A. Oliver, X. Lladó, J. Freixenet, and M. Bach Cuadra, "A review of atlas-based segmentation for magnetic resonance brain images", *Computer methods and programs in biomedicine*, vol. 104, no. 3, e158–e177, 2011.

[235] P. A. Cook, H. Zhang, S. P. Awate, and J. C. Gee, "Atlas-guided probabilistic diffusion-tensor fiber tractography", in *5th International Symposium on Biomedical Imaging: From Nano to Macro – ISBI 2008*, IEEE, 2008, pp. 951–954.

[236] P.-T. Yap, J. H. Gilmore, W. Lin, and D. Shen, "PopTract: population-based tractography", *IEEE Trans. Med. Imag.*, vol. 30, no. 10, pp. 1829–1840, 2011.

[237] A. Yendiki, P. Panneck, P. Srinivasan, A. Stevens, L. Zöllei, J. Augustinack, R. Wang, D. Salat, S. Ehrlich, T. Behrens, S. Jbabdi, R. Gollub, and B. Fischl, "Automated probabilistic reconstruction of white-matter pathways in health and disease using an atlas of the underlying anatomy", *Front. Neuroinform.*, vol. 5, 2011.

[238] S. Jbabdi, M. W. Woolrich, J. L. R. Andersson, and T. E. J. Behrens, "A Bayesian framework for global tractography", *NeuroImage*, vol. 37, no. 1, pp. 116–129, 2007.

[239] D. Raffelt, J.-D. Tournier, S. Crozier, A. Connelly, and O. Salvado, "Reorientation of fiber orientation distributions using apodized point spread functions", *Magn. Reson. Med.*, vol. 67, no. 3, pp. 844–855, Dec. 2012. DOI: 10.1002/mrm.23058.

[240] M. Jenkinson, C. F. Beckmann, T. E. J. Behrens, M. W. Woolrich, and S. M. Smith, "FSL", *NeuroImage*, vol. 62, no. 2, pp. 782–90, Aug. 2012. DOI: 10.1016/j.neuroimage.2011.09.015.

[241] J. L. R. Andersson, M. Jenkinson, and S. Smith, "Non-linear registration aka spatial normalisation – FMRIB technial report TR07JA2", Oxford, UK, Tech. Rep. June, 2007, p. 22.

[242] B. Fischl, "FreeSurfer", *NeuroImage*, vol. 62, no. 2, pp. 774–781, 2012.

[243] S. Bauer, R. Wiest, L.-P. Nolte, and M. Reyes, "A survey of mri-based medical image analysis for brain tumor studies", *Physics in Medicine and Biology*, vol. 58, no. 13, R97–R129, 2013. DOI: 10.1088/0031-9155/58/13/R97.

[244] S. Durrleman, P. Fillard, X. Pennec, A. Trouvé, and N. Ayache, "Registration, atlas estimation and variability analysis of white matter fiber bundles modeled as currents", *NeuroImage*, vol. 55, no. 3, pp. 1073–90, 2011.

[245] L. J. O'Donnell, W. M. Wells, A. J. Golby, and C.-F. Westin, "Unbiased groupwise registration of white matter tractography", in *Medical Image Computing and Computer Assisted Intervention – MICCAI 2012*, N. Ayache, H. Delingette, P. Golland, and K. Mori, Eds., ser. Lecture Notes in Computer Science, vol. 7512, Nice, France: Springer, Heidelberg, 2012, pp. 123–30.

[246] U. Ziyan, M. R. Sabuncu, L. J. O'Donnell, and C.-F. Westin, "Nonlinear registration of diffusion MR images based on fiber bundles", in *Medical Image Computing and Computer Assisted Intervention – MICCAI 2007*, N. Ayache, S. Ourselin, and A. Maeder, Eds., ser. Lecture Notes in Computer Science, vol. 4791, Brisbane, Australia: Springer, Heidelberg, 2007, pp. 351–8.

[247] M. W. A. Caan, L. J. Van Vliet, C. B. L. M. Majoie, M. M. Van Der Graaff, C. A. Grimbergen, and F. M. Vos, "Nonrigid point set matching of white matter tracts for diffusion tensor image analysis", *IEEE Transactions on Biomedical Engineering*, vol. 58, no. 9, pp. 2431–40, 2011.

[248] O. Zvitia, A. Mayer, R. Shadmi, S. Miron, and H. K. Greenspan, "Co-registration of white matter tractographies by adaptive-mean-shift and Gaussian mixture modeling", *IEEE Trans. Med. Imag.*, vol. 29, no. 1, pp. 132–45, 2010.

[249] A. Mayer, G. Zimmerman-Moreno, R. Shadmi, A. Batikoff, and H. Greenspan, "A supervised framework for the registration and segmentation of white matter fiber tracts", *IEEE Trans. Med. Imag.*, vol. 30, no. 1, pp. 131–45, 2011.

[250] F. Calamante, J.-D. Tournier, G. D. Jackson, and A. Connelly, "Track-density imaging (TDI): Super-resolution white matter imaging using whole-brain track-density mapping", *NeuroImage*, vol. 53, no. 4, pp. 1233–43, 2010.

[251] D. Raffelt, J.-D. Tournier, J. Fripp, S. Crozier, A. Connelly, and O. Salvado, "Symmetric diffeomorphic registration of fibre orientation distributions", *NeuroImage*, vol. 56, no. 3, pp. 1171–80, 2011.

[252] T. Vercauteren, X. Pennec, A. Perchant, and N. Ayache, "Diffeomorphic demons: Efficient non-parametric image registration", *NeuroImage*, vol. 45, no. 1, S61–S72, 2009.

[253] T. Dhollander, J. Veraart, W. Van Hecke, F. Maes, S. Sunaert, J. Sijbers, and P. Suetens, "Feasibility and advantages of diffusion weighted imaging atlas construction in q-space", in *Medical Image Computing and Computer Assisted Intervention – MICCAI 2011*, G. Fichtinger, A.

Martel, and T. Peters, Eds., ser. Lecture Notes in Computer Science, vol. 6892, Toronto, Canada: Springer Berlin Heidelberg, 2011, pp. 166–73. DOI: 10.1007/978-3-642-23629-7_21.

[254] J. Du, A. Goh, and A. Qiu, "Diffeomorphic metric mapping of high angular resolution diffusion imaging based on Riemannian structure of orientation distribution functions", *IEEE Trans. Med. Imag.*, vol. 31, no. 5, pp. 1021–33, 2012.

[255] V. Siless, J. Glaunès, P. Guevara, J.-F. Mangin, C. Poupon, D. Le Bihan, B. Thirion, and P. Fillard, "Joint T1 and brain fiber log-demons registration using currents to model geometry", in *Medical Image Computing and Computer Assisted Intervention – MICCAI 2012*, N. Ayache, H. Delingette, P. Golland, and K. Mori, Eds., ser. Lecture Notes in Computer Science, vol. 7511, Nice, France: Springer, Heidelberg, 2012, pp. 57–65.

[256] D. Holland, J. M. Kuperman, and A. M. Dale, "Efficient correction of inhomogeneous static magnetic field-induced distortion in Echo Planar Imaging", *NeuroImage*, vol. 50, no. 1, pp. 175–83, 2010.

[257] S. Wakana, H. Jiang, L. M. Nagae-Poetscher, P. C. M. Van Zijl, and S. Mori, "Fiber tract-based atlas of human white matter anatomy", *Radiology*, vol. 230, no. 1, pp. 77–87, 2004.

[258] J. Shi and J. Malik, "Normalized cuts and image segmentation", *Pattern Analysis and Machine Intelligence, IEEE Transactions on*, vol. 22, no. 8, pp. 888–905, 2000.

[259] C. Fowlkes, S. Belongie, F. Chung, and J. Malik, "Spectral grouping using the nystrom method", *IEEE Trans. Pattern Anal. Machine Intell.*, vol. 26, no. 2, pp. 214–225, 2004.

[260] V. Vapnik, *The nature of statistical learning theory*. Springer, 2000.

[261] L. Breiman, "Random forests", *Machine learning*, vol. 45, no. 1, pp. 5–32, 2001.

[262] P. Geurts, D. Ernst, and L. Wehenkel, "Extremely randomized trees", *Machine Learning*, vol. 63, no. 1, pp. 3–42, Mar. 2006. DOI: 10.1007/s10994-006-6226-1.

[263] B. Jeurissen, J.-D. Tournier, and J. Sijbers, "Tissue-type segmentation using non-negative matrix factorization of multi-shell diffusion-weighted MRI images", in *International Society for Magnetic Resonance in Medicine (ISMRM) 23th Annual Meeting & Exhibtion*, vol. 23, Toronto, Ontario, Canada, May 2015, p. 349.

[264] Y. Xie, J. Ho, and B. C. Vemuri, "Nonnegative factorization of diffusion tensor images and its applications", in *Information Processing in Medical Imaging: 22nd International Conference, IPMI 2011, Kloster Irsee, Germany, July 3-8, 2011. Proceedings*, ser. Lecture Notes in Computer Science, G. Székely and H. K. Hahn, Eds., vol. 6801, Springer Berlin Heidelberg, 2011, pp. 550–561. DOI: 10.1007/978-3-642-22092-0_45.

[265] M. Reisert, I. Mader, R. Umarova, S. Maier, L. Tebartz van Elst, and V. G. Kiselev, "Fiber density estimation from single q-shell diffusion imaging by tensor divergence", *NeuroImage*, vol. 77, pp. 166–176, Mar. 2013. DOI: 10.1016/j.neuroimage.2013.03.032.

[266] P. Paatero and U. Tapper, "Positive matrix factorization: A non-negative factor model with optimal utilization of error estimates of data values", *Environmetrics*, vol. 5, no. 2, pp. 111–126, Jun. 1994. DOI: 10.1002/env.3170050203.

[267] D. D. Lee and H. S. Seung, "Learning the parts of objects by non-negative matrix factorization", *Nature*, vol. 401, no. 6755, pp. 788–791, Oct. 1999. DOI: 10.1038/44565.

[268] I. S. Dhillon and D. S. Modha, "Concept decompositions for large sparse text data using clustering", *Machine Learning*, vol. 42, no. 1, pp. 143–175, 2001. DOI: 10.1023/a:1007612920971.

[269] J. MacQueen, "Some methods for classification and analysis of multivariate observations", in *Proceedings of the Fifth Berkeley Symposium on Mathematical Statistics and Probability, Volume 1: Statistics*, Berkeley, Calif.: University of California Press, 1967, pp. 281–297.

[270] M. S. Andersen, J. Dahl, and L. Vandenberghe, *CVXOPT: a Python package for convex optimization, version 1.1.7*, 2014.

[271] E. Caruyer, C. Lenglet, G. Sapiro, and R. Deriche, "Design of multishell sampling schemes with uniform coverage in diffusion MRI", *Magn. Reson. Med.*, vol. 69, no. 6, pp. 1534–1540, Apr. 2013. DOI: 10.1002/mrm.24736.

[272] J. L. Andersson and S. N. Sotiropoulos, "An integrated approach to correction for off-resonance effects and subject movement in diffusion MR imaging", *NeuroImage*, vol. 125, pp. 1063–1078, Jan. 2016. DOI: 10.1016/j.neuroimage.2015.10.019.

[273] N. J. Tustison, B. B. Avants, P. A. Cook, Y. Zheng, A. Egan, P. A. Yushkevich, and J. C. Gee, "N4ITK: improved N3 bias correction", *IEEE Trans. Med. Imag.*, vol. 29, no. 6, pp. 1310–1320, Jun. 2010. DOI: 10.1109/tmi.2010.2046908.

[274] E. Calabrese, A. Badea, C. L. Coe, G. R. Lubach, M. A. Styner, and G. A. Johnson, "Investigating the tradeoffs between spatial resolution and diffusion sampling for brain mapping with diffusion tractography: Time well spent?", *Human Brain Mapping*, vol. 35, no. 11, pp. 5667–5685, Jul. 2014. DOI: 10.1002/hbm.22578.

[275] H. Akaike, "A new look at the statistical model identification", *IEEE Trans. Automatic Control*, vol. 19, no. 6, pp. 716–723, Dec. 1974. DOI: 10.1109/tac.1974.1100705.

[276] G. Schwarz, "Estimating the dimension of a model", *Ann. Statist.*, vol. 6, no. 2, pp. 461–464, Mar. 1978. DOI: 10.1214/aos/1176344136.

[277] A. B. Owen and P. O. Perry, "Bi-cross-validation of the SVD and the nonnegative matrix factorization", *Ann. Appl. Stat.*, vol. 3, no. 2, pp. 564–594, Jun. 2009. DOI: 10.1214/08-aoas227.

[278] P. Sajda, S. Du, T. Brown, R. Stoyanova, D. Shungu, X. Mao, and L. Parra, "Nonnegative matrix factorization for rapid recovery of constituent spectra in magnetic resonance chemical shift imaging of the brain", *IEEE Trans. Med. Imag.*, vol. 23, no. 12, pp. 1453–1465, Dec. 2004. DOI: 10.1109/tmi.2004.834626.

[279] S. Ortega-Martorell, P. J. G. Lisboa, A. Vellido, R. V. Simões, M. Pumarola, M. Julià-Sapé, and C. Arús, "Convex non-negative matrix factorization for brain tumor delimitation from MRSI data", *PLoS ONE*, vol. 7, no. 10, D. Monleon, Ed., e47824, Oct. 2012. DOI: 10.1371/journal.pone.0047824.

[280] N. Sauwen, D. M. Sima, S. V. Cauter, J. Veraart, A. Leemans, F. Maes, U. Himmelreich, and S. V. Huffel, "Hierarchical non-negative matrix factorization to characterize brain tumor heterogeneity using multi-parametric MRI", *NMR in Biomedicine*, vol. 28, no. 12, pp. 1599–1624, Oct. 2015. DOI: 10.1002/nbm.3413.

[281] T. Roine, B. Jeurissen, D. Perrone, J. Aelterman, W. Philips, A. Leemans, and J. Sijbers, "Informed constrained spherical deconvolution (iCSD)", *Med. Image Anal.*, vol. 24, no. 1, pp. 269–281, Aug. 2015. DOI: 10.1016/j.media.2015.01.001.

[282] V. Golkov, J. M. Portegies, A. Golkov, R. Duits, and D. Cremers, "Holistic image reconstruction for diffusion MRI", in *Computational Diffusion MRI – MICCAI Workshop*, ser. Mathematics and Visualization 6, Munich, Germany, 2016, pp. 27–39. DOI: 10.1007/978-3-319-28588-7_3.

[283] G. V. Steenkiste, B. Jeurissen, J. Veraart, A. J. den Dekker, P. M. Parizel, D. H. J. Poot, and J. Sijbers, "Super-resolution reconstruction of diffusion parameters from diffusion-weighted images with different slice orientations", *Magn. Reson. Med.*, vol. 75, no. 1, pp. 181–195, Jan. 2015. DOI: 10.1002/mrm.25597.

[284] C.-F. Westin, H. Knutsson, O. Pasternak, F. Szczepankiewicz, E. Özarslan, D. van Westen, C. Mattisson, M. Bogren, L. J. O'Donnell, M. Kubicki, D. Topgaard, and M. Nilsson, "Q-space trajectory imaging for multidimensional diffusion MRI of the human brain", *NeuroImage*, Feb. 2016. DOI: 10.1016/j.neuroimage.2016.02.039.

[285] E. Kellner, B. Dhital, V. G. Kiselev, and M. Reisert, "Gibbs-ringing artifact removal based on local subvoxel-shifts", *Magn. Reson. Med.*, n/a–n/a, Nov. 2015. DOI: 10.1002/mrm.26054.

[286] D. C. Alexander, D. Zikic, J. Zhang, H. Zhang, and A. Criminisi, "Image quality transfer via random forest regression: Applications in diffusion MRI", in *Medical Image Computing and Computer-Assisted Intervention – MICCAI 2014*, ser. Lecture Notes in Computer Science, P. Golland, N. Hata, C. Barrillot, J. Hornegger, and R. Howe, Eds., vol. 8675, Boston, MA, USA, 2014, pp. 225–232. DOI: 10.1007/978-3-319-10443-0_29.

[287] P. F. Neher, M. Götz, T. Norajitra, C. Weber, and K. H. Maier-Hein, "A machine learning based approach to fiber tractography using classifier voting", in *Medical Image Computing and Computer-Assisted Intervention – MICCAI 2014*, ser. Lecture Notes in Computer Science, N. Navab, J. Hornegger, W. M. Wells, and A. F. Frangi, Eds., vol. 9349, Boston, MA, USA: Springer International Publishing, 2014, pp. 45–52. DOI: 10.1007/978-3-319-24553-9_6.

[288] V. Golkov, A. Dosovitskiy, P. Sämann, J. I. Sperl, T. Sprenger, M. Czisch, M. I. Menzel, P. A. Gómez, A. Haase, T. Brox, and D. Cremers, "Q-space deep learning for twelve-fold shorter and model-free diffusion MRI scans", in *Medical Image Computing and Computer-Assisted Intervention – MICCAI 2015*, ser. Lecture Notes in Computer Science, N. Navab, J. Hornegger, W. M. Wells, and A. F. Frangi, Eds., vol. 9349, Munich, Germany: Springer International Publishing, 2015, pp. 37–44. DOI: 10.1007/978-3-319-24553-9_5.

[289] V. Golkov, T. Sprenger, J. Sperl, and M. Menzel, "Model-free novelty-based diffusion MRI", in *International Symposium on Biomedical Imaging: From Nano to Macro*, Prague, Czech Republic: IEEE, Apr. 2016, pp. 1233–1236.

Curriculum

ir. Daan Christiaens (° Etterbeek, 14 September 1989) completed his high school studies in science-mathematics in 2007 at the Jan-van-Ruusbroeckollege in Brussels. In 2010, he obtained his B.Sc. in Computer Science at KU Leuven (minor in Electrical Engineering, magna cum laude). In 2012, he graduated at KU Leuven as M.Sc. in Biomedical Engineering (magna cum laude). His master thesis on "The effect of spatial transformations of diffusion-weighted images on fibre tracking" was awarded the Materialise thesis prize and motivated him to pursue a Ph.D. in this field.

During his studies, Daan worked as a trainee at Asyril in Fribourg, Switzerland for two months and later chaired the local committee of IAESTE, a global internship exchange network, in Leuven. After graduating in 2012, he started a Ph.D. fellowship of IWT Flanders in the Medical Image Computing lab at KU Leuven under supervision of prof. Frederik Maes and prof. Stefan Sunaert. His work was published in NeuroImage and presented at MICCAI and ISMRM. At the latter conference, he twice received ISMRM magna cum laude awards for his work. In addition, Daan has contributed to the development of the open source software package MRtrix, supervised 3 master thesis students, and taught exercise sessions and practicals in 3 courses at bachelor and master level.

In his spare time, Daan enjoys travelling, rock climbing and mountaineering. He is also a bit of a foodie and likes to read about the world.

List of publications

International journal articles

2015 D. Christiaens, M. Reisert, T. Dhollander, S. Sunaert, P. Suetens, and F. Maes, "Global tractography of multi-shell diffusion-weighted imaging data using a multi-tissue model", *NeuroImage*, vol. 123, pp. 89–101, Dec. 2015 (cover image).

2016 D. Christiaens, S. Sunaert, P. Suetens, and F. Maes, "Convexity-constrained and nonnegativity-constrained spherical factorization in diffusion-weighted imaging" (in revision).

2016 T. Billiet, L. Emsell, M. Vandenbulcke, R. Peeters, D. Christiaens, A. Leemans, W. van Hecke, A. Smeets, F. Amant, S. Sunaert, and S. Deprez, "Recovery from chemotherapy-induced white matter changes?" (in review).

2016 O. Maier, B. Menze, M. Liebrandt, S. Winzeck, L. Häni, M. Heinrich, J. von der Gablentz, A. Basit, P. Bentley, L. Chen, D. Christiaens, F. Dutil, K. Egger, C. Feng, B. Glocker, M. Götzp, T. Haeck, H.-L. Halmen, M. Havaei, K. M. Iftekharuddin, P.-M. Jodoin, K. Kamnitsas, E. Kellner, A. Korvenoja, H. Larochelle, C. Ledig, J.-H. Lee, F. Maes, Q. Mahmood, K. H. Maier-Hein, R. McKinley, C. Pal, L. Pei, J. Rangarajan, S. M. S. Reza, D. Robben, D. Rueckert, E. Salli, P. Suetens, C.-W. Wang, M. Wilms, P. Schramm, T. F. Münte, U. M. Krämer, M. Reyes, and H. Handels, "ISLES 2015 – A public evaluation benchmark for ischemic stroke lesion segmentation from multispectral MRI" (in review).

2016 L. Emsell, C. Adamson, F. Bouckaert, T. Billiet, D. Christiaens, F. De Winter, M. Seal, P. Sienaert, S. Sunaert, and M. Vandenbulcke, "Corpus callosum morphology and microstructure in late-life depression" (in review).

International conference papers: published in full in proceedings

2015 D. Christiaens, F. Maes, S. Sunaert, and P. Suetens, "Convex non-negative spherical factorization of multi-shell diffusion-weighted images", in *Medical Image Computing and Computer-Assisted Intervention – MICCAI 2015*, N. Navab, J. Hornegger, W. M. Wells, and A. F. Frangi, Eds., ser. Lecture Notes in Computer Science, vol. 9349, Munich, Germany: Springer International Publishing, Oct. 2015, pp. 166–173 (traditional poster).

2015 D. Robben, D. Christiaens, J. Rangarajan, J. Gelderblom, P. Joris, F. Maes, and P. Suetens, "A voxel-wise, cascaded classification approach to stroke lesion segmentation", in *Brainlesion: Glioma, Multiple Sclerosis, Stroke and Traumatic Brain Injuries*, A. Crimi, B. Menze, O. Maier, M. Reyes, and H. Handels, Eds., ser. Lecture Notes in Computer Science, vol. 9556, Munich, Germany: Springer International Publishing, Oct. 2015, pp. 254–265 (3rd place in SPES subchallenge).

2014 D. Christiaens, M. Reisert, T. Dhollander, F. Maes, S. Sunaert, and P. Suetens, "Atlas-guided global tractography: Imposing a prior on the local track orientation", in *Computational Diffusion MRI – MICCAI Workshop*, L. O'Donnell, G. Nedjati-Gilani, Y. Rathi, M. Reisert, and T. Schneider, Eds., ser. Mathematics and Visualization, Cambridge, MA, USA: Springer International Publishing, Sep. 2014, pp. 115–123 (oral presentation).

2014 D. Vercruysse, D. Christiaens, F. Maes, S. Sunaert, and P. Suetens, "Fiber bundle segmentation using spectral embedding and supervised learning", in *Computational Diffusion MRI – MICCAI Workshop*, L. O'Donnell, G. Nedjati-Gilani, Y. Rathi, M. Reisert, and T. Schneider, Eds., ser. Mathematics and Visualization, Cambridge, MA, USA: Springer International Publishing, Sep. 2014, pp. 103–114 (oral presentation).

2013 D. Christiaens, T. Dhollander, F. Maes, S. Sunaert, and P. Suetens, "Groupwise deformable registration of fiber track sets using track orientation distributions", in *Computational Diffusion MRI and Brain Connectivity – MICCAI Workshop*, T. Schultz, G. Nedjati-Gilani, A. Venkataraman, L. O'Donnell, and E. Panagiotaki, Eds., ser. Mathematics and Visualization, Nagoya, Japan: Springer International Publishing, Sep. 2013, pp. 151–161 (oral presentation).

2012 D. Christiaens, T. Dhollander, F. Maes, S. Sunaert, and P. Suetens, "The effect of reorientation of the fibre orientation distribution on fibre tracking", in *Computational Diffusion MRI – MICCAI Workshop*, E. Panagiotaki, L. O'Donnell, T. Schultz, and G. Zhang, Eds., Nice, France, Oct. 2012 (oral presentation).

International conference abstracts

2016 D. Christiaens, F. Maes, S. Sunaert, and P. Suetens, "Unsupervised multi-tissue decomposition of single-shell diffusion-weighted imaging by generalization to multi-modal data", in *International Society for Magnetic Resonance in Medicine (ISMRM) 24th Annual Meeting & Exhibtion*, vol. 24, Singapore, May 2016 (electronic poster, magna cum laude award).

2016 L. Emsell, C. Adamson, F. Bouckaert, T. Billiet, D. Christiaens, F. De Winter, M. Seal, P. Sienaert, S. Sunaert, and M. Vandenbulcke, "Corpus callosum morphology and microstructure in late-life depression", in *International Society for Magnetic Resonance in Medicine (ISMRM) 24th Annual Meeting & Exhibtion*, vol. 24, Singapore, May 2016 (traditional poster, psychiatry study group 2nd best poster award).

2016 T. Billiet, L. Emsell, M. Vandenbulcke, R. Peeters, D. Christiaens, A. Leemans, W. Van Hecke, A. Smeets, F. Amant, S. Sunaert, and S. Deprez, "Investigating possible recovery of chemotherapy-induced white matter changes in breast cancer", in *ICCTF congress*, Amsterdam, The Netherlands, Mar. 2016, p. 62.

2015 D. Christiaens, F. Maes, S. Sunaert, and P. Suetens, "Imposing label priors in global tractography can resolve crossing fibre ambiguities", in *International Society for Magnetic Resonance in Medicine (ISMRM) 23th Annual Meeting & Exhibtion*, vol. 23, Toronto, Ontario, Canada, May 2015, p. 2258 (oral presentation, magna cum laude award).

2015 D. Christiaens, F. Maes, S. Sunaert, and P. Suetens, "Can label priors in global tractography resolve crossing fibre ambiguities?", in *ISMRM Benelux Chapter 7th Annual Meeting*, Ghent, Belgium, Jan. 2015 (oral presentation).

2014 D. Robben, D. Christiaens, F. Maes, and P. Suetens, "Regression and classification using random forest-based techniques", in *MICCAI 2014 Machine Learning Challenge (MLC)*, Cambridge, MA, USA, Sep. 2014 (oral presentation).

2014 D. Christiaens, F. Maes, S. Sunaert, and P. Suetens, "Global tractography of multi-shell HARDI data", in *International Society for Magnetic Resonance in Medicine (ISMRM) 22th Joint Annual Meeting ISMRM-ESMRMB*, vol. 22, Milan, Italy, May 2014, p. 270 (oral presentation).

2014 T. Billiet, S. Deprez, B. Maedler, R. Peeters, H. Zhang, A. Leemans, T. Dhollander, D. Christiaens, F. Amant, A. Smeets, B. Van den Bergh, M. Vandenbulcke, E. Legius E, S. Sunaert, and L. Emsell, "Investigating the long-term effects of systemic chemotherapy on brain white matter using multi-shell diffusion MRI and myelin water imaging", in *International Society for Magnetic Resonance in Medicine (ISMRM) 22th Joint Annual Meeting ISMRM-ESMRMB*, vol. 22, Milan, Italy, May 2014, p. 1915 (traditional poster).

2014 D. Christiaens, F. Maes, S. Sunaert, and P. Suetens, "Global tractography of multi-shell diffusion data", in *ISMRM Benelux Chapter 6th Annual Meeting*, Maastricht, The Netherlands, Jan. 2014 (oral presentation).

2014 T. Billiet, S. Deprez, B. Maedler, R. Peeters, H. Zhang, A. Leemans, T. Dhollander, D. Christiaens, F. Amant, A. Smeets, B. Van den Bergh, M. Vandenbulcke, E. Legius E, S. Sunaert, and L. Emsell, "Investigating the long-term effects of systemic chemotherapy on brain white matter using multi-shell diffusion MRI and myelin water imaging", in *ISMRM Benelux Chapter 6th Annual Meeting*, Maastricht, The Netherlands, Jan. 2014 (traditional poster).

2014 T. Billiet, S. Deprez, B. Maedler, R. Peeters, H. Zhang, A. Leemans, T. Dhollander, D. Christiaens, F. Amant, A. Smeets, B. Van den Bergh, M. Vandenbulcke, E. Legius E, S. Sunaert, and L. Emsell, "Investigating the long-term effects of systemic chemotherapy on brain white matter using multi-shell diffusion MRI and myelin water imaging", in *ICCTF Conference*, Seattle, WA, USA, Feb. 2014.

2013 D. Christiaens, F. Maes, S. Sunaert, and P. Suetens, "Global fibre reconstruction of multi-shell HARDI data", in *ISMRM workshop on diffusion as a probe of neural tissue microstructure*, Podstrana, Croatia, Oct. 2013 (traditional poster).

2013 T. Billiet, S. Deprez, D. Christiaens, R. Peeters, S. Sunaert, and L. Emsell, "DKI more sensitive than DTI for detecting microstructural brain changes in patients with breast cancer recovering from chemotherapy", in *ISMRM workshop on diffusion as a probe of neural tissue microstructure*, Podstrana, Croatia, Oct. 2013 (traditional poster).

2013 D. Christiaens, T. Dhollander, F. Maes, S. Sunaert, and P. Suetens, "On the estimation of the fiber response function for constrained spherical deconvolution", in *ISMRM Benelux Chapter 5th Annual Meeting*, Rotterdam, The Netherlands, Jan. 2013 (traditional poster).

Thesis

2012 D. Christiaens, "The effect of spatial transformations of diffusion-weighted images on fibre tracking", Master thesis, KU Leuven, Leuven, Belgium, June 2012 (Materialise master thesis prize for biomedical engineering).

FACULTY OF ENGINEERING SCIENCE
DEPARTMENT OF ELECTRICAL ENGINEERING
CENTER FOR PROCESSING SPEECH AND IMAGES
Herestraat 49 box 7003
B-3000 Leuven